A MULTI-RESOLUTION DISCONTINUOUS GALERKIN METHOD FOR UNSTEADY COMPRESSIBLE FLOWS

A Thesis
Presented to
The Academic Faculty

by

Andrew B. Shelton

In Partial Fulfillment
of the Requirements for the Degree
Doctor of Philosophy in the
School of Aerospace Engineering

Georgia Institute of Technology
August 2008

A MULTI-RESOLUTION DISCONTINUOUS GALERKIN METHOD FOR UNSTEADY COMPRESSIBLE FLOWS

Approved by:

Dr. Marilyn Smith, Advisor
School of Aerospace Engineering
Georgia Institute of Technology

Dr. Hao-Min Zhou, Co-Advisor
School of Mathematics
Georgia Institute of Technology

Dr. Suresh Menon
School of Aerospace Engineering
Georgia Institute of Technology

Dr. Stephen Ruffin
School of Aerospace Engineering
Georgia Institute of Technology

Dr. Luca Dieci
School of Mathematics
Georgia Institute of Technology

Date Approved: 30 June 2008

Dedicated to Anna and Ella

who bring Love and Joy to my world

ACKNOWLEDGEMENTS

I am most humbled by and grateful for my family members, who have provided for me the steadfast encouragement, humor, patience, and inspiration during the taxing times that often typify one's graduate career. The successful completion of this work is certainly due to the "behind the scenes" toil and sacrifice of my loving wife, Anna, and our beautiful daughter Ella.

I am grateful to my major department research advisor, Dr. Marilyn Smith, for above all giving me the freedom to explore my ideas (even the overly-ambitious ones). I am also thankful for the inspiring and enlightening discussions on multi-resolution with my minor department research advisor Dr. Hao-Min Zhou. I appreciate the positive and constructive feedback for improving this research from the thesis committee members Dr. Suresh Menon, Dr. Stephen Ruffin, and Dr. Luca Dieci. My fellow graduate students and lab partners provided much needed reality checks, advice, and diversion: David O'Brien, Jennifer Abras, Eric Lynch, Chirag Talati, and Nick Burgess have my appreciation and best-wishes for continued success.

TABLE OF CONTENTS

LIST OF FIGURES

LIST OF SYMBOLS OR ABBREVIATIONS

d	vector of details coordinates; also spatial dimension.
B	Vandermond matrix, mapping of modal expansion coefficients to nodal values at special quadrature nodes.
$f(u)$	nonlinear function of scalar state, first coordinate direction.
$F(U)$	nonlinear function of system state, first coordinate direction.
$g(u)$	nonlinear function of scalar state, second coordinate direction.
$G(U)$	nonlinear function of system state, first coordinate direction.
G	low-pass filter.
h	sub-region of Ω obtained by n times subdivision.
H	high pass filter.
J	Jacobian of coordinate transformation, $J = \det[\partial(x, y)/\partial(\xi, \eta)]$.
k	number of modes in expansion.
M	mass matrix.
n	levels of detail.
p	polynomial degree.
u	generic state for scalar conservation law.
U	generic state for system of conservation laws.
V	Vandermond matrix, mapping modal expansion coefficients to nodal values at special interpolation nodes.
W	diagonal matrix of Guass-type quadrature weights.
Γ	boundary trace of spatial region.
Ω	spatial region.
$\phi(\tau)$	scaling function, basis function in piecewise polynomial averages space $\mathcal{V}$.
$\psi(\tau)$	wavelet function, basis function in orthogonal complement space $\mathcal{W}$.
τ	generic spatial coordinate(s).
ξ	generic first coordinate direction.
η	generic second coordinate direction.
a^*	function a evaluated along shared boundary trace, requiring numerical flux function.

$\tilde{a}$	globally continuous function.
$\bar{a}$	vector of modal coordinates.
$\vec{a}$	vector of nodal coordinates.
$\mathbf{e}_{(i)}$	unit vector in the i-th direction.
$\mathcal{F}_n$	numerical normal flux function.
$\mathbb{P}$	orthogonal projector onto the averages space.
$\mathbb{Q}$	orthogonal projector onto the details space.
$\mathcal{U}$	numerical state function.
$\mathcal{V}$	piecewise polynomial function space.
$\mathcal{W}$	othogonal complement space to $\mathcal{V}$.
$\langle a, b \rangle$	inner product of functions $a(\tau)$ and $b(\tau)$, $\langle a, b \rangle = \int ab \, \mathrm{d}\tau$.
$\|a\|$	induced norm of function $a(\tau)$, $\|a\| = \langle a, a \rangle^{1/2}$.
$\|\bar{a}\|$	vector norm, $\|\bar{a}\| = (\bar{a}^{\mathrm{T}}\bar{a})^{1/2}$.
DG	discontinuous Galerkin.
DoF	degrees of freedom.
MR	multi-resolution.

SUMMARY

The issue of local scale and smoothness presents a crucial and daunting challenge for numerical simulation methods in fluid dynamics. Yet in the interests of both accuracy and economy, how can one devise a general technique that efficiently resolves flow features of consequence and discriminates against others which are either "negligible" or amenable to "universal" modeling? This is particularly difficult because geometries of engineering interest are complex and multi-dimensional, precluding *a priori* knowledge of the flowfield. To address this challenge, the current work employs wavelet theory for the local scale decomposition of functions, which provides a natural mechanism for the adaptive compression of data. The resulting technique is known as the Multi-Resolution Discontinuous Galerkin (MRDG) method.

This research successfully demonstrates that the multi-resolution framework and the discontinuous Galerkin method are well-suited for a new approach to accuracy and cost as demonstrated by the relative ease of their integration in spatial dimension greater than one. Some specific steps achieved include the implementation of suitable data encoding and compression algorithms, construction of multi-wavelet expansion bases in one and two dimensions, and derivation of the multi-resolution derivative operator that includes an upwind-type correction to the central scheme. Solutions with the MRDG method are observed to adapt to and track both smooth and discontinuous flow features in an entirely solution-driven manner without the need for *a priori* user knowledge of those flow features. Run-time efficiency and local adaptation characteristics are explored via a series of classic test problems.

CHAPTER I

INTRODUCTION

1.1 Motivation

It is generally recognized that the nonlinear conservation laws governing fluid dynamics inherently admit wide-ranging spatial and temporal scales. While parameters of interest may only be observed on the coarsest scales, it is the event interactions that occur over many scales that determine the values of these parameters. If a numerical solution fails to capture these events there is not only the loss of local accuracy but a potentially disastrous loss of fundamental system-level response. The impact of the ubiquitous energy cascade of turbulent flows on mixing of species and temperature is an easy example, but there are other flow features such as shear layers, vortices, and shock waves that – depending on the perspective of the observer – appear as asymptotically small driving factors.

The issue of scale and *local* smoothness presents a crucial and daunting challenge for numerical simulation methods in fluid dynamics. Since the advantage of one method over another for a given application ultimately rests on the consideration of both accuracy and cost, how can one devise a general technique that efficiently resolves flow features of consequence and discriminates against others which are either "negligible" or amenable to "universal" modeling? This is particularly difficult when faced with the prospect that flow geometries of engineering interest are complex and multi-dimensional, precluding *a priori* knowledge of the flowfield.

To address this challenge, the current work has been largely inspired by the idea of employing wavelet theory for the local scale decomposition of functions, thereby providing a natural mechanism for adaptive compression of data. Particularly engaging examples of this strategy (specifically aimed at the physics of turbulence) are demonstrated in methods known as Coherent Vortex Simulation (CVS) [29, 30] and Stochastic Coherent Adaptive Large Eddy Simulation (SCALES) [33]. These methods are based on the principle that

a wavelet decomposition applied to a turbulent field may be used to dynamically identify and evolve only the most energetic eddies such that the ill-effects due pure modeling of the dissipative scales are minimized. This is precisely the resolution capability sought. Unfortunately, it is not clear how these methods could be formulated for general flow domains without resorting to the usual pitfalls of generalized cartesian meshes, immersed boundary conditions, *etc.* To bring these important works into the mainstream, it appears that there is a need to consider scale decomposition in the context of the topological flexibility afforded by high-order unstructured discretizations.

1.2 Background

It is generally appreciated that spatial resolution depends *collectively* on discretization scale h and formal order of accuracy (or quality) p, *viz*, the local error is of the familiar form $E = \mathcal{O}(h^p)$. Much of recent effort, however, has focused high order methods in isolation. While traditional engineering practice has utilized second-order finite difference (FD) methods or finite volume (FV) methods with much success, the accurate prediction of highly time and scale-dependent flows has ultimately exposed their inherent weaknesses. In particular, it is well-known that low diffusion, high-order accurate methods are required to alleviate non-physical and premature vortex dissipation typical of low order methods. It is also well-known that high order spatial accuracy proves to be more efficient for long-time integration of unsteady problems

Consider as an example the passive convection of an inviscid vortex in a doubly-periodic domain [82]. Figure 1 shows flowfield isobars at the initial time, and it is expected that vortex returns to the origin every $D_{\text{core}}/V_{\text{ambient}}\Delta t$ time integration steps *undisturbed* from the initial configuration. The kinetic energy of the Euler system, defined as $k_{\text{sys}} = \frac{1}{2}\int(u^2 + v^2)\,\mathrm{d}x\,\mathrm{d}y$, is an invariant quantity. Thus, any deviation from the initial level of k_{sys} indicates the accumulation of numerical dissipation in the solution and a loss of accuracy. To demonstrate the efficiency of increasing order of accuracy, the time-dependent solution for this problem is computed on meshes of 32, 128, 512, and 2048 elements of degree 9, 5, 3, and 1, respectively, using the methodology described in Chapter 2. The results of this simple

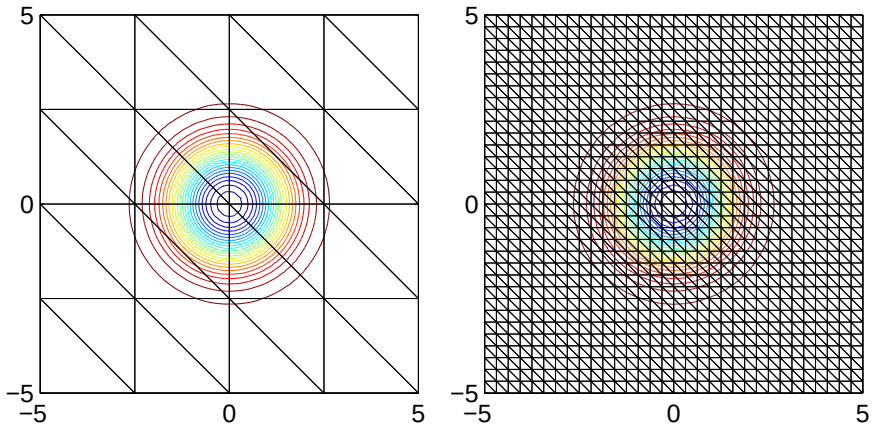

Figure 1: Vortex in a small periodic domain for long-time passive convection. Shown here are 29 contours for the pressure in the range $0.1 \leq p \leq 0.8$ at the initial time. Several element / degree combinations are used for the test: shown here are $N = 32$ elements of degree $p = 9$ (left) and $N = 2048$ elements of degree $p = 1$ (right).

test are shown in Figure 2. Depending on what is considered an acceptable level of kinetic energy decay, short-time integration using a piecewise linear scheme may be an option, particularly if such a code is readily available and only a few cases of different input parameters are of interest. However, if there is either a strenuous error threshold over longer times or many cases to run, the appeal of high order becomes apparent due it's ability to provide lower error at a lower cost. Despite the fact that the linear timestep stability restriction due to the Courant-Freidrichs-Levy number has been shown [23] to vary as $\text{CFL} = (2p+1)^{-1}$, high-order spatial schemes with simple explicit time evolution have a tremendous advantages over their low-order counterparts. The construction of high-order spatial schemes – especially for the unstructured meshes preferred for complex physical domains – has thus become a focal point of research in computational fluid dynamics.

Unfortunately, extending both FD and FV methods to high-order has proved problematic in practice due to issues of convergence, stability, boundary conditions, and parallelization on the extended computational stencils in non-smooth meshes. The high-order accurate conservative method known as the discontinuous Galerkin (DG) method appears to be a most promising approach. Developed in recent years by many researchers, the method has been especially championed by the teams of Cockburn, Shu, *et al.* [22, 23], Bassi, Rebay, *et al.* [11, 10, 12, 9], Karniadakis, Hesthaven, *et al.* [47, 54, 78, 43], and Remacle, Flaherty,

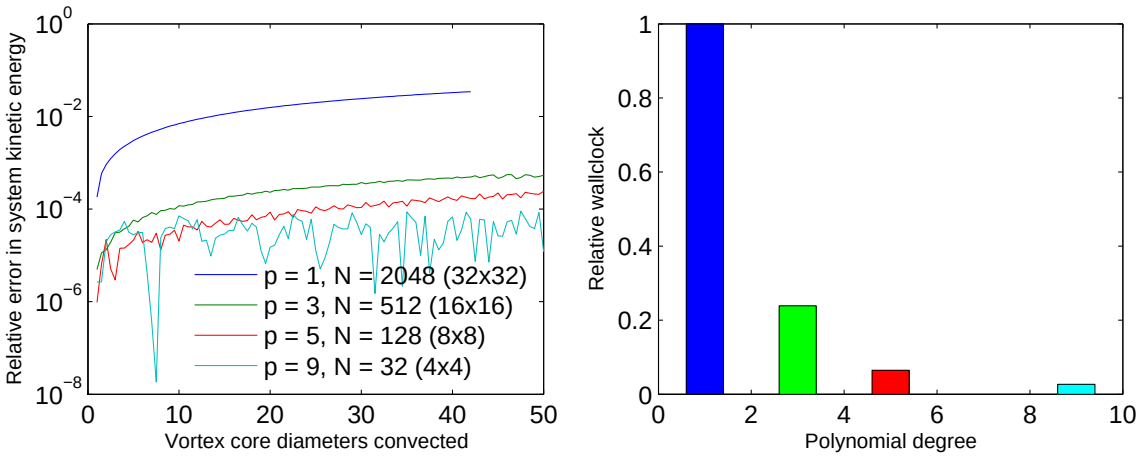

Figure 2: Efficiency of a high-order scheme for long-time integration.

Shephard, *et al.* [66]. The DG method (originally viewed as a hybrid of spectral finite element and finite volume approaches) is indeed the *natural* extension of finite volume to high order. In this setting, the method enjoys exponential convergence properties (providing higher accuracy per degree of freedom compared to lower-order methods) while retaining geometric versatility. The DG method assumes a function expansion for the distribution of the flow variables within each individual element and solves for the modes of the expansion by minimizing the residual in the Galerkin approach. It is important to note that traditional FV formally does the same, though using only single mode corresponding to the constant term, and seeks high order by an *unnatural* extrapolation of the cell averages (see Figure 3). Typical of conservative FV schemes, the resulting DG variables are generally discontinuous across the element boundaries; therefore, inter-element communication of flow information is maintained by the customary application of a Riemann-like flux. Since the element reconstruction is self-contained (no reliance on an extended stencil of neighboring elements,) the discretization is invariantly compact with increasing order of accuracy. Enforcement of consistently accurate and general boundary conditions is natural and trivial, as the solution is known at the selected expansion degree up to and including element boundaries. Non-conforming meshes with "hanging" vertices can be treated without difficulty, and elements of different order of accuracy can be easily accommodated in the same mesh. For approximations in a hierarchical and orthogonal basis, p refinement is a trivial exercise, only

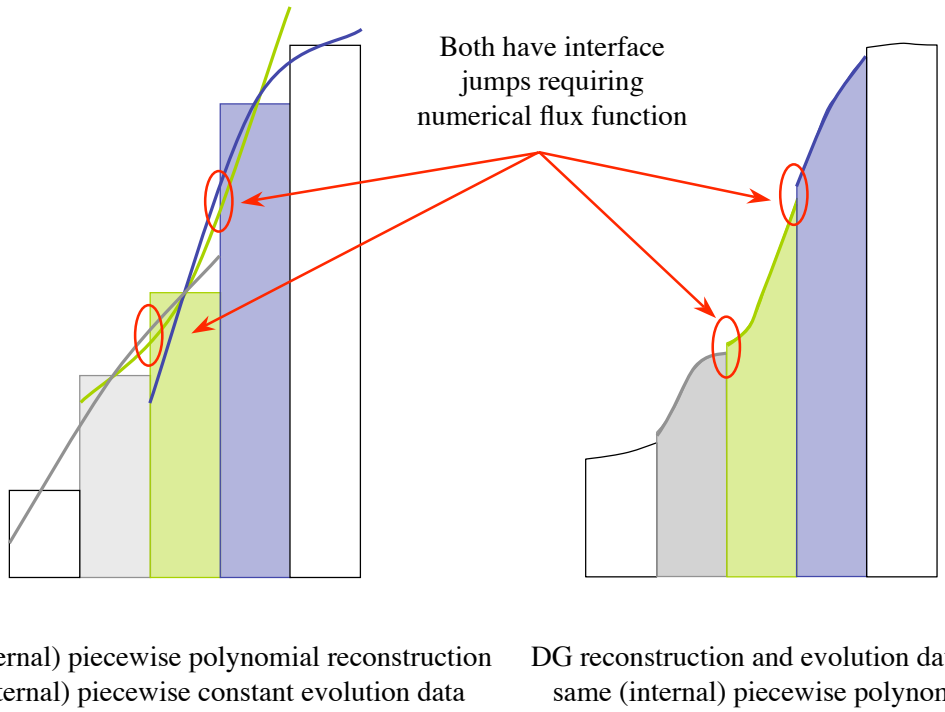

Figure 3: Comparison of finite volume and discontinuous Galerkin interface reconstruction strategies. In the FV method, only the cell-average is evolved in time thus requiring an additional mechanism for extrapolating a higher-order reconstruction to the element interfaces. In the DG method, the entire reconstruction within each element is evolved in time and neighbor communication is limited to computation of the interface flux only. This concentrates degrees of freedom in a more compact physical region and provides an invariant stencil.

requiring the addition of modes to the expansion. However, while p refinement is a strong driver of accuracy (for "smooth" problems,) it is well-localized only in spectral space, not in physical space. Therefore events of scale sufficiently small so as to appear sharp relative to the local scale h, refinement in p inevitably leads to the Gibb's phenomenon. For this reason some form of non-uniform mesh is required that broadly captures either the geometry or the local scale of the problem.

A traditional means of dealing with wide-ranging physical scales is solution adaptation by either mesh movement (r refinement) or – more commonly – mesh refinement (h refinement). In this approach, mesh vertices are moved towards or added within target regions marked by a solution error sensor. This allows the localization of solution degrees of freedom (DoF) and thus efficient allocation of resources. Figure 4 shows a modification

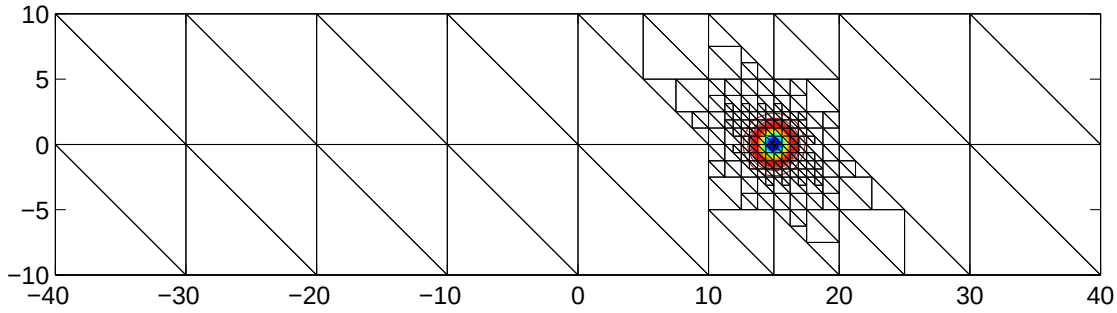

Figure 4: Example of solution adaptation applied to vortex convection in a long distance periodic domain.

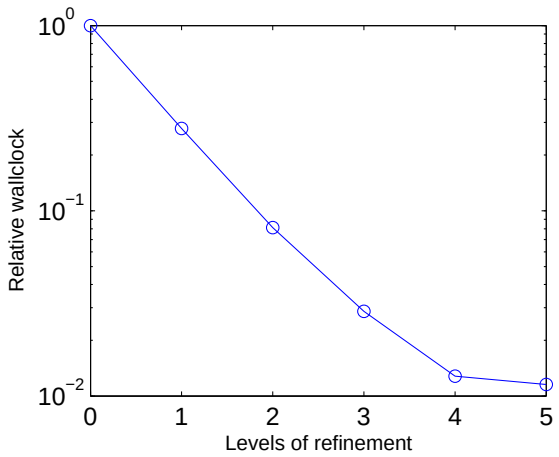

Figure 5: Adaptation cost payoff for vortex convection in a long distance periodic domain using piecewise linear elements.

to the vortex problem above in which the passive convection occurs in a significantly larger domain. The flowfield is characterized by large benign regions away from the vortex core, as indicated by the decreasing mesh density. To demonstrate the efficiency of solution adaptation, the time-dependent solution for this modified problem is computed on an effective mesh of 32768 elements of degree 1 using the methodology described in Chapter 3. The results in Figure 5 show orders-of-magnitude decrease in total solution cost.

Robust solution adaptation is not without difficulty in practice, beginning with the fact that the true solution error required for triggering adaptation is generally unknown *a priori*. Therefore various *ad hoc* estimation techniques have been proposed, with a threshold on solution gradient a common choice. Beyond the obvious difficulties of mesh reconstruction

and computational stencil data management, r and h refinement can be especially problematic for unsteady problems. First, the coarse solution must be of sufficient quality to sense the triggering event. Second, some mesh adaptations have led to non-physical results due to a dominance of numerical error over any increased accuracy afforded by refinement. In recent years, adjoint-based adaptation has been successfully developed as a means of combating these two difficulties, but is unfortunately to date a steady-state approach. Finally, adaptation along domain boundaries requires accurate knowledge of the boundary geometry, in turn necessitating an interface with some form of CAD geometry engine. Therefore, h refinement alone or in concert with p refinement is compromised by the limitations of error sensor design and the quality of the baseline, low-fidelity solution.

A promising and mathematically elegant alternative is the multi-resolution representation of data developed in the classic works by Meyer [60], Mallat [57, 58], Daubechies [24], and Harten [36, 37, 38, 40, 39]. Within the multi-resolution framework, a signal or field event is viewed as a composition of fluctuations on top of a comparatively smooth background, and – by recursive application of this idea – a hierarchy of scales is constructed. Such a perspective is indeed a quite natural form of description. At coarser levels, the fluctuations are the "context" of the event, while at finer levels, the fluctuations provide its most distinguishing features [57]. The decision whether to employ certain distinguishing features rests entirely on their *value added* to the overall description. Multi-resolution is the antithetical approach to the resolution and cost problem: remain within the error of the highest quality approximation available (the "reference scheme") and gain economy by discarding information that falls below a given tolerance. This is the notion of adaptive data compression and the inherent use of computationally sparse operations in a numerical method.

The now inseparably related field of wavelets has witnessed an explosion of interest from mathematicians and engineers alike, owing to the convergence of rich and diverse ideas from many technical disciplines (see [25] for a short and informal account, or [41] for a history of seminal papers). In its most simplistic view, the term wavelets denotes a family of self-similar functions that are obtained from a single "mother wavelet" by the operations

of dilation and translation. Construction of mother wavelets that lead to bases in $L^2(\mathbb{R})$ provides an approximation capability that is well-localized in both scale and frequency. Furthermore, by retaining only the most significant coefficients in a wavelet basis expansion, a sparse representation of a function is obtained. These traits have made wavelets especially attractive for signal and image compression and denoising, with two obvious examples being the FBI fingerprint database and the JPEG 2000 standard. The solution of partial differential equations (PDEs) has benefitted as well, and small sample of approaches can be found in [73, 18, 31, 46, 44, 72]. It became clear early-on that traditional wavelets suffer from the fact that they are translations and dilations of a single function and do not form a basis for functions on a *finite* interval. There are then conceptual difficulties extending wavelets to bounded and general geometries as the domain must be artificially extended or periodized, or the basis functions at the boundaries must be modified. Alternative solutions include abandoning strict orthogonality (bi-orthogonal wavelets) and the translation / dilation relationship (second-generation wavelets).

In a remarkable series of papers [36, 37, 38], Harten developed a more general framework of multi-resolution analysis in which traditional and bi-orthogonal wavelets are special cases. Particulary interesting is the multi-resolution of cell-averages [19, 1], which provides clear connection to and extension of traditional low-order finite volume methods. A characteristic of the application of operators to data in the multi-resolution setting – differentiating it from other adaptive techniques – is the concept of inter-scale effects. For example, Figure 6 shows that in a local mesh refinement scheme, the interface communication considers only the regions present at a given instant. The error sensor must be robust enough to precipitate the necessary refinement in advance before an operator (such as a derivative) requires an accurate interface flux. In contrast, multi-resolution permits information exchange between regions in the same refinement level by demotion and promotion of the details through the application of high- and low-pass filters. Furthermore, multi-resolution operators are constructed in terms of details upon averages in much the same way as the data upon which they work. This means that inter-region communication as shown in Figure 7 is multi-scale event such that output data may immediately contain smaller scales and/or

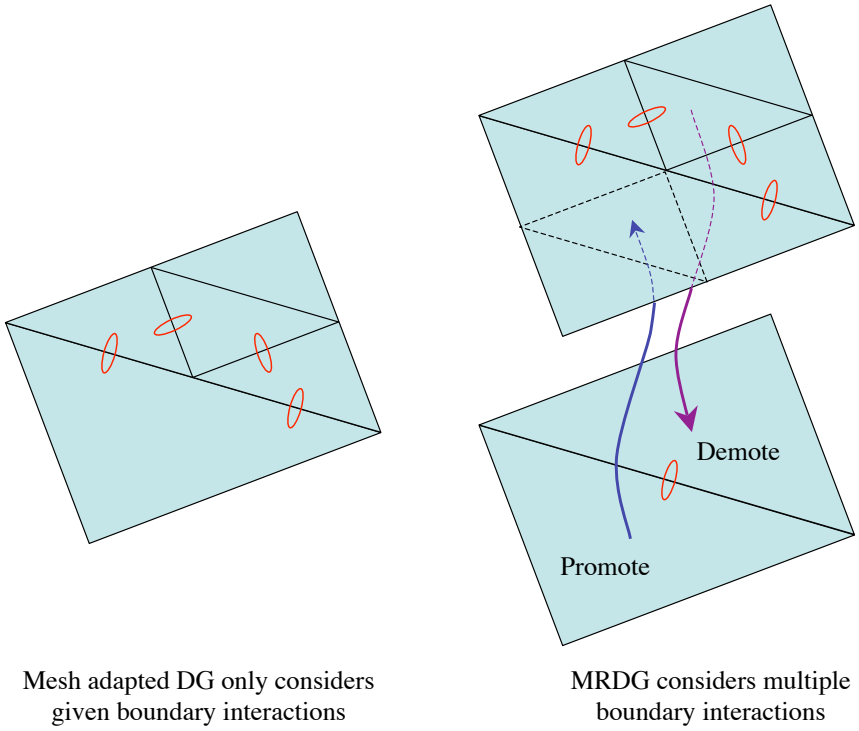

Figure 6: Comparison of element interface communication in a traditional local refinement scheme and in the multi-resolution setting. The multi-resolution permits information exchange between regions in the same refinement level by promotion and demotion of details.

higher expansion modes than the input data.

As an aside, note that these ideas of transferring flow information between scales is reminiscent of, but wholly different from, the application of multigrid in both purpose and approach. In multigrid, nested meshes (and/or hierarchial expansion bases) provide a framework for low-frequency error elimination by the restriction of the state and residual to a coarse mesh (low-order basis) and error prolongation back to the fine mesh (high-order basis) for solution correction. The restriction and prolongation operators are indeed much like the low-pass filter and its transpose, respectfully. However, there are no details to be added to or extracted from information at a given level through a high-pass filter for the purpose of adaptation and compression of the fine scale (reference scheme) data. Recent examples of multigrid exploiting both the h and p components of the DG method may be found in Mavriplis [61, 74, 59] and Darmofal [26].

Returning to data compression and adaptation in the multi-resolution setting, Alpert

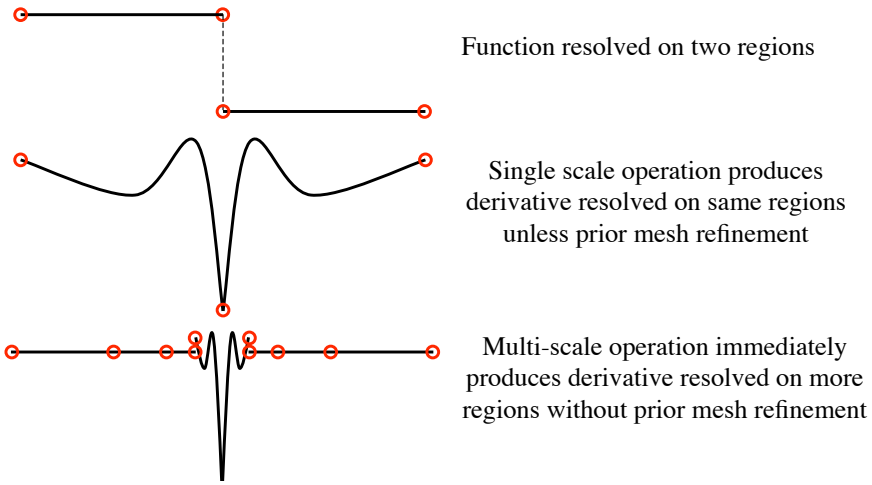

Figure 7: Comparison of the computation of the weak derivative operation in a traditional local refinement and in the multi-resolution setting. Since multi-resolution operators – like the data upon which they work – are comprised of details upon averages, inter-region communication is a multi-scale event and does not require *a priori* mesh refinement.

explored bases for the sparse representation of smooth integral operators on finite domains [3, 4]. The result was a class of multi-wavelets that enable scale-dependent, high-order approximation of functions supported on non-overlapping intervals. The price to pay is lost regularity, as the functions are built upon the orthogonal Legendre polynomial family and recursive bisection of the parent domain is used to achieve translation / dilation. These multi-wavelets were eventually utilized for the adaptive computation of PDEs on the interval [2]. A crucial component of that work is the use of weak derivative operators necessitated by the discontinuous nature of the multi-wavelets. This strategy is of course entirely consistent with the discontinuous Galerkin method, although no explicit reference was ever made. Additionally, Alpert's construction technique for the multi-wavelets may be extended to higher dimensional simplicial domains (such as the triangle) in a straightforward manner [83]. It would seem that a general approach is within reach by combining multi-resolution and discontinuous Galerkin to simultaneously accommodate locality in both formal order of accuracy and physical scale.

1.3 Objective

This research develops an advanced computational technique for accurate, efficient, first-principles-based engineering simulation of compressible flows that by its very design respects the central theme of high-resolution and cost-effectiveness. This is accomplished by integrates the enabling technologies found in (1) the compression and local adaptation properties of the multi-resolution (MR) representation of data and associated operators; and (2) the locally conservative, high order accuracy, invariantly compact stencil, and topologically flexible control volume properties of the discontinuous Galerkin (DG) method.

This research will demonstrate the feasibility of the approach in three phases. First, a high-order DG method is developed and applied to prototypical flows in one and two dimensions on unstructured meshes, demonstrating both the h and p convergence properties of the method as well as the specific application of high-order to a curved boundary domain. Next, the multi-resolution extension of the DG method is developed with as much spatial dimension generality as possible. The method is applied initially to one-dimensional examples elucidating the automatic and local adaptive properties afforded by the MR representation. Finally, the ingredients required to implement the MRDG method in higher spatial dimension with triangular and eventually tetrahedral elements are specified. The final examples will demonstrate the full two-dimensional unstructured development and application of MRDG to flows exhibiting disparate length scales.

CHAPTER II

DISCONTINUOUS GALERKIN METHOD

The following development presents the tools required for solution of the Euler equations by the discontinuous Galerkin method. The discussion begins with the fundamental discretization approach, and subsequently ascends the levels of detail required to implement a tractable numerical solution method utilizing the simplest possible component techniques. The method is demonstrated by application to several canonical problems for the Euler equations in one and two spatial dimensions.

2.1 Variational Form

It suffices to discuss the details of discretization for a scaler equation. Consider the following generic conservation law on some global domain $x, y \in \Omega_g$ having boundary $\Gamma_g = \partial\Omega_g$

$$\frac{\partial \tilde{u}}{\partial t} + \frac{\partial}{\partial x}\tilde{f}(\tilde{u}) + \frac{\partial}{\partial y}\tilde{g}(\tilde{u}) = 0 \tag{1}$$

Multiply by a test function φ and integrate over Ω_g using parts to obtain the weighted residual form

$$\left\langle \varphi, \frac{\partial \tilde{u}}{\partial t} \right\rangle_{\Omega_g} - \left\langle \frac{\partial \varphi}{\partial x}, \tilde{f} \right\rangle_{\Omega_g} - \left\langle \frac{\partial \varphi}{\partial y}, \tilde{g} \right\rangle_{\Omega_g} + \left\langle \varphi, n_x \tilde{f} + n_y \tilde{g} \right\rangle_{\Gamma_g} = 0 \tag{2}$$

Specifying that both the test function φ and the trial function $\tilde{u}$ belong to the same function space, the weighted residual is a Galerkin method.

There are two primary steps required to discretize the problem. First, partition the domain into a collection of non-overlapping, boundary conforming elements Ω_e of characteristic size h_e as

$$\Omega_g = \bigcup_e \Omega_e, \quad \Omega_e \cap \Omega_{e'} = \emptyset \text{ for } e' \neq e \tag{3}$$

Second, approximate on each element the continuous function space as a vector space $\mathcal{V}_p$

with finite dimension $k(p)$

$$\begin{aligned}\mathcal{V}_p = \{f\colon\ & \text{the restriction of } f \text{ to the domain } \Omega_e \\ & \text{is a polynomial of degree less or equal to } p, \\ & \text{and } f \text{ vanishes elsewhere } \}\end{aligned} \tag{4}$$

By projecting the globally continuous test and trial functions onto the *broken* approximation space [14, 13] as

$$\begin{aligned}\varphi \approx \mathbb{P}_k \varphi = \phi \in \mathcal{V}_p \\ \tilde{u} \approx \mathbb{P}_k \tilde{u} = u \in \mathcal{V}_p\end{aligned} \tag{5}$$

the variational form becomes: find $u \in \mathcal{V}_p$ such that $\forall \phi \in \mathcal{V}_p$

$$\left\langle \phi, \frac{\partial u}{\partial t} \right\rangle_{\Omega_e} - \left\langle \frac{\partial \phi}{\partial x}, f \right\rangle_{\Omega_e} - \left\langle \frac{\partial \phi}{\partial y}, g \right\rangle_{\Omega_e} + \langle \phi, (n_x f + n_y g)^* \rangle_{\Gamma_e} = 0 \tag{6}$$

Due to the discontinuous nature of the function space, the normal trace $f_n = n_x f + n_y g$ is no longer uniquely defined and thus is written with the notation $(\cdot)^*$. In this case it is replaced by a numerical flux function $\mathcal{F}_n(u^e, u^b)$ along each portion Γ_b of Γ_e shared by elements e, b and is subject to the consistency requirements

$$\begin{aligned}\mathcal{F}_n(u, u) = f_n(u) \\ \mathcal{F}_n(u^e, u^b) = -\mathcal{F}_n(u^b, u^e)\end{aligned} \tag{7}$$

Note that *all* boundary integrals – including those along Γ_g – are most naturally enforced in this "weak" sense through the numerical fluxes. Integrating by parts once more, this time selecting the normal trace from within the element e, the final formulation for the Discontinuous Galerkin (DG) method is: find $u \in \mathcal{V}_p$ such that $\forall \phi \in \mathcal{V}_p$

$$\left\langle \phi, \frac{\partial u}{\partial t} \right\rangle_{\Omega_e} + \left\langle \phi, \frac{\partial f}{\partial x} + \frac{\partial g}{\partial y} \right\rangle_{\Omega_e} + \langle \phi, (n_x f + n_y g)^* - (n_x f + n_y g) \rangle_{\Gamma_e} = 0 \tag{8}$$

From this point on, Ω_e is denoted simply as Ω and is omitted it all together from the inner product subscript unless required for clarity.

2.2 Approximation by Series Expansion

This section introduces the necessary tools required to transform the DG variational statement derived above into a form suitable for numerical solution. For simplicity, the development works in a single spatial dimension as the results here extend straightforwardly to

higher dimensions.

2.2.1 Series Approximation

By projecting onto the space $\mathcal{V}_p$, a function $\tilde{f}(x)$ is approximated by expansion in a finite $k(p)$ term basis $\phi_0(x), \phi_1(x), \ldots, \phi_{k-1}(x)$ as

$$\tilde{f}(x) \approx \mathbb{P}_k \tilde{f}(x) = f(x) = \sum_{j=0}^{k-1} \bar{f}_j \phi_j(x) \tag{9}$$

For an orthonormal basis, $\langle \phi_i, \phi_j \rangle = \delta_{ij}$, and

$$\bar{f}_i = \langle \phi_i, f \rangle \tag{10}$$

which will become obvious below.

2.2.2 Transformations Between Physical and Modal Spaces

The set of coefficients $\bar{f} = \{\bar{f}_0, \bar{f}_1, \ldots, \bar{f}_{k-1}\}$ represents the modal space coordinates of the approximation. For the (discrete) physical space representation of the function, introduce a set of k approximation nodes $\vec{x} = \{x_0, x_1, \ldots, x_{k-1}\}$, and a set of q quadrature nodes $\vec{r} = \{r_0, r_1, \ldots, r_{q-1}\}$ having associated weights $\vec{w} = \{w_0, w_1, \ldots, w_{q-1}\}$. As discussed later, the approximation nodes are optimally chosen for accurate interpolation and are equal in number to the modes in the expansion. On the other hand, the quadrature nodes are optimally chosen to exactly integrate polynomials of the given degree or less with the fewest possible points, although they generally differ in number from the number of modes, typically $q > k$. Now denote

$$f_i = f(x_i) \quad \longrightarrow \quad \vec{f} = f(\vec{x}) \tag{11}$$

$$f_i^Q = f(r_i) \quad \longrightarrow \quad \vec{f}^Q = f(\vec{r}) \tag{12}$$

The basis functions evaluated at these sets of points generate matrices having nodes along rows and modes along columns written as

$$V_{ij} = \phi_j(x_i) \tag{13}$$

$$B_{ij} = \phi_j(r_i) \tag{14}$$

The $k \times k$ matrix V and the $q \times k$ matrix B are the Vandermonde matrices, and are linear maps from the vector of coefficients of the basis to vectors of sampled values. Depending on the choice of nodes, the transformation from modal to physical space is simply

$$f(x_i) = \sum_j V_{ij} \bar{f}_j \quad \longrightarrow \quad \vec{f} = V \bar{f} \tag{15}$$

$$f(r_i) = \sum_j B_{ij} \bar{f}_j \quad \longrightarrow \quad \vec{f}^{Q} = B \bar{f} \tag{16}$$

The consequence of the choice of nodes is the manner in which the inverse transformation from physical to modal space is performed. For the approximation nodes, the *collocation projection* is simply

$$\bar{f} = V^{-1} \vec{f} \tag{17}$$

However, for the quadrature nodes, the basis matrix B is not square and the situation requires a bit more work.

Consider the inner product of two functions f, g, each having an expansion in terms of ϕ_j:

$$\begin{aligned} \langle g, f \rangle &= \int_\Omega \sum_i \bar{g}_i \phi_i(x) \sum_j \bar{f}_j \phi_j(x) \, \mathrm{d}x \\ &= \sum_i \sum_j \left(\int_\Omega \phi_i(x) \phi_j(x) \, \mathrm{d}x_b \right) \bar{g}_i \bar{f}_j \\ &= \sum_i \sum_j \bar{g}_i M_{ij} \bar{f}_j \end{aligned} \tag{18}$$

The mass matrix is $M_{ij} = \langle \phi_i, \phi_j \rangle$, and for an orthonormal basis becomes δ_{ij} by definition. The above result simplifies to

$$\langle g, f \rangle = \bar{g}^T \bar{f} \tag{19}$$

Thus the inner product of two functions expanded in an orthonormal basis is equal to the inner product of their respective modal coordinate vectors. Consequently, the function norm is equal to its corresponding modal coordinate vector norm

$$\| f(x) \| = |\bar{f}| \tag{20}$$

Let $g = \phi_i$, then $\vec{g} = \phi_i(\vec{x}) = V_{[:,i]} = V \mathbf{e}_{(i)}$, from which it follows that $\bar{g} = \mathbf{e}_{(i)}$, i.e., the unit vector in the i-th direction. Therefore, an inner product of f with one of its basis functions

ϕ_i is

$$\langle \phi_i, f \rangle = \mathbf{e}_{(i)}^T \bar{f} = \bar{f}_i \tag{21}$$

which is of course is the result previously stated.

The inner product of g, f may also be computed by means of numerical quadrature as

$$\begin{aligned} \langle g, f \rangle &= \int_\Omega g(x) f(x) \, \mathrm{d}x \\ &\approx \sum_p g(r_p) w_p f(r_p) \\ &= \sum_p \sum_i \sum_j B_{pi} \bar{g}_i w_p B_{pj} \bar{f}_j \\ &= \sum_p \sum_i \sum_j B_{pi} \bar{g}_i W_{pp} B_{pj} \bar{f}_j \\ &= \bar{g}^T \left(B^T W B \right) \bar{f} \end{aligned} \tag{22}$$

where W is the diagonal matrix $W_{ii} = w_i$, and it is worth noting that $B^T W B \approx M$ to machine precision. Again making the substitution $g = \phi_i$, the previous relation becomes

$$\langle \phi_i, f \rangle \approx \ \mathbf{e}_{(i)}^T \left(B^T W B \right) \bar{f} \tag{23}$$

Recalling that $B\bar{f} = \vec{f^Q}$, it follows that

$$\bar{f} = \left(B^T W B \right)^{-1} B^T W \vec{f^Q} \tag{24}$$

This is the *Galerkin projection* and the desired transformation from physical space to modal space using the quadrature nodes. The significance and utility of this device will become clear later.

2.2.3 Differentiation

To approximate the derivative of the function f requires the derivatives of the basis

$$f_x(x) = \frac{\mathrm{d}}{\mathrm{d}x} f(x) = \sum_{j=0}^{k-1} \bar{f}_j \frac{\mathrm{d}}{\mathrm{d}x} \phi_j(x) \quad \longrightarrow \quad \vec{f_x} = V_x \bar{f} \tag{25}$$

where the derivative Vandermonde matrix is

$$V_{x_{pj}} = \frac{\mathrm{d}}{\mathrm{d}x} \phi_j(x_p) \tag{26}$$

Of course, direct expansion of $\mathrm{d}\tilde{f}/\mathrm{d}\xi$ is also valid

$$\mathbb{P}_k \frac{\mathrm{d}}{\mathrm{d}x}\tilde{f}(x) = f_x(x) = \sum_{j=0}^{k-1} \bar{f}_{x_j}\phi_j(x) \quad \longrightarrow \quad \vec{f_x} = V\bar{f}_x \tag{27}$$

The unknown modal coordinates $\bar{f}_x$ are found by equating the respective $\vec{f_x}$ from the two approaches with the result that

$$\bar{f}_x = D_x\bar{f} \tag{28}$$

where the derivative operator is

$$D_x = V^{-1}V_x \tag{29}$$

This technique is called collocation differentiation.

2.2.4 Boundary Inner Product

Given a suitable basis for the some Γ_b of Ω, the transformations between physical and modal spaces described above hold, *viz*

$$\vec{f}_{(b)} = V_{(b)}\bar{f}_{(b)} \tag{30}$$

$$\bar{f}_{(b)} = V_{(b)}^{-1}\vec{f}_{(b)} \tag{31}$$

The trace function $f_{(b)}$ on Γ_b is simply interpolated from f on Ω as

$$\vec{f}_{(b)} = f(\vec{x}_b) \tag{32}$$

While it is not required, it is most convenient to have boundary approximation nodes shared by the interior approximation nodes. As shown later, the choice of approximation nodes can indeed be constructed with this property, in which case

$$f(\vec{x}_b) = \vec{f}_{[\vec{i}_{(b)}]} = V_{[\vec{i}_{(b)},:]}\bar{f} \tag{33}$$

where $\vec{i}_{(b)}$ is the index set of the particular interior approximation nodes that lie on boundary. Switching from interior modal coordinates to boundary modal coordinates is easily accomplished as

$$\bar{f}_{(b)} = X_{(b)}\bar{f} \tag{34}$$

with the extraction operator defined as

$$X_{(b)} = V_{(b)}^{-1} V_{[\vec{i}_{(b)},:]} \tag{35}$$

Now consider the generic boundary inner product

$$\langle g, f \rangle_\Gamma = \sum_b \langle g, f \rangle_{\Gamma_b} = \sum_b \bar{g}_{(b)}^T M_{(b)} \bar{f}_{(b)} \tag{36}$$

Making the by now familiar substitution $g = \phi_i$ and using the extraction operator above on the modes of g, the inner product becomes

$$\langle \phi_i, f \rangle_{\Gamma_b} = \mathbf{e}_{(i)}^T X_{(b)}^T M_{(b)} \bar{f}_{(b)} \tag{37}$$

Anticipating that the inverse of the element mass matrix is applied to all terms, the boundary operator is defined as

$$S_{(b)} = M^{-1} X_{(b)}^T M_{(b)} \tag{38}$$

Of course in the case of orthonormal bases, $M_{ij} = \delta_{ij}$ and $M_{(b)_{ij}} = \delta_{ij}$ such that the boundary operator reduces to

$$S_{(b)} = X_{(b)}^T \tag{39}$$

2.2.5 Matrix Form of Variational Statement

Taking the semi-discrete approach, the basis is a function of space and the modal coordinates are a function of time, *viz*

$$u(x, y, t) = \sum_{j=0}^{k-1} \bar{u}_j(t) \phi_j(x, y) \tag{40}$$

Now applying the results developed so far, the DG variational statement: find $u \in \mathcal{V}_p$ such that $\forall \phi \in \mathcal{V}_p$

$$\left\langle \phi, \frac{\partial u}{\partial t} \right\rangle_\Omega + \left\langle \phi, \frac{\partial f}{\partial x} + \frac{\partial g}{\partial y} \right\rangle_\Omega + \langle \phi, \mathcal{F}_n - f_n \rangle_\Gamma = 0 \tag{41}$$

has the following matrix operator form:

$$\frac{\mathrm{d}}{\mathrm{d}t} \bar{u} + D_x \bar{f} + D_y \bar{g} + \sum_b S_{(b)} \left(\bar{\mathcal{F}}_{n\,(b)} - \bar{f}_{n\,(b)} \right) = 0 \tag{42}$$

2.3 Specification of Basis, Nodes, and Element Geometry

The Vandermonde matrix V clearly plays a crucial role in the development, and its conditioning depends both on the construction of the basis $\phi_{m(ij)}(x, y)$ and the particular selection of the approximation nodes. While the simplest choice for the basis is the set of monomials $\{x^i y^j : 0 \leq i + j < m\}$, this results in a Vandermonde matrix with exponentially growing condition number and thus extremely problematic evaluation of V^{-1}. This reflects the unfortunate reality that the basis becomes numerically linearly dependent with an increasing number of modes. The familiar solution to this situation is choose a basis that is orthonormalized with respect to some inner product, such as the Legendre polynomials on the interval. As for the selection of nodes, recent attention has been devoted to Fekete points [70, 78], which are closely related to optimal interpolation points and specifically maximize the determinant of V to make it far from singular. The following focuses on the bi-unit domains for the interval $\Omega_{\text{int}} = \{x : -1 \leq x \leq 1\}$ and the right triangle $\Omega_{\text{tri}} = \{x, y : -1 \leq x, y \leq 1;\ x + y \leq 0\}$ for construction of the basis and nodes and utilizes coordinate mapping for the general element.

2.3.1 Hierarchical and Orthonormal Basis Functions

A basis is orthonormal if $\forall \phi \in \mathcal{V}_p$ then $\langle \phi_i, \phi_j \rangle = \delta_{ij}$, and is hierarchical if

$$\mathcal{V}_p = \mathcal{V}_0 \oplus (\mathcal{V}_1 \setminus \mathcal{V}_0) \oplus (\mathcal{V}_2 \setminus \mathcal{V}_1) \oplus \cdots \oplus (\mathcal{V}_p \setminus \mathcal{V}_{p-1}) \tag{43}$$

Both of these properties are well worth the extra effort required in construction of the basis, by simplifying analysis, method derivation and coding, and enhancing numerical performance. Additionally, adaptive refinement in the degree of the polynomial approximating space (p refinement) is a trivial task.

Recall that the set of monomials shown by the Pascals's triangle of degree p

$$\begin{array}{ccccccc} & & & 1 & & & \\ & & & x & y & & \\ & & x^2 & xy & y^2 & & \\ & x^3 & x^2y & xy^2 & y^3 & & \\ & & & \vdots & & & \\ x^p & x^{p-1}y & \cdots & xy^{p-1} & y^p & & \end{array} \tag{44}$$

is a hierarchical basis for the approximating space $\mathcal{V}_p$. The total number of terms $k(p)$ – and hence the dimension of the space – are for the interval and triangle respectfully

$$k_{\text{int}} = p + 1, \quad k_{\text{tri}} = \frac{(p+2)(p+1)}{2} \tag{45}$$

The Gram-Schmidt procedure [71] may be applied to these monomials to obtain an orthogonal basis that maintains the hierarchical property. The crucial concept to the procedure is as follows: when given set of j orthonormal functions $q_0, q_1, \ldots, q_{j-1}$ in some domain Ω and an arbitrary function v in the same domain, a function $v^\perp$ orthogonal to $q_0, q_1, \ldots, q_{j-1}$ is constructed by

$$v^\perp = v - \sum_{i=0}^{j-1} \langle q_i, v \rangle q_i \tag{46}$$

The result is then normalized as usual by $\|v^\perp\| = \langle v^\perp, v^\perp \rangle^{1/2}$.

Remarkably, it turns out that a basis constructed in this way yields results identical to the the eigenfunctions of the singular Sturm-Liouville problem and could therefore be considered as "natural" [81, 80]. Recall that singular Sturm-Liouville problem on the interval gives rise to the general class of Jacobi polynomials $P_j^{\alpha,\beta}(x)$, with the classical Chebyshev polynomials $T_j(x)$ and Legendre polynomials $L_j(x)$ (see Figure 8) among the more familiar and commonly used subclasses:

$$T_j = \frac{2^{2n}(n!)^2}{(2n)!} P_j^{1/2,1/2}(x), \quad L_j = P_j^{0,0}(x) \tag{47}$$

On a triangle the eigenfunctions are known as the Koornwinder-Dubiner polynomials [50, 27]. These are quite conveniently written as a tensor products of Jacobi polynomials in

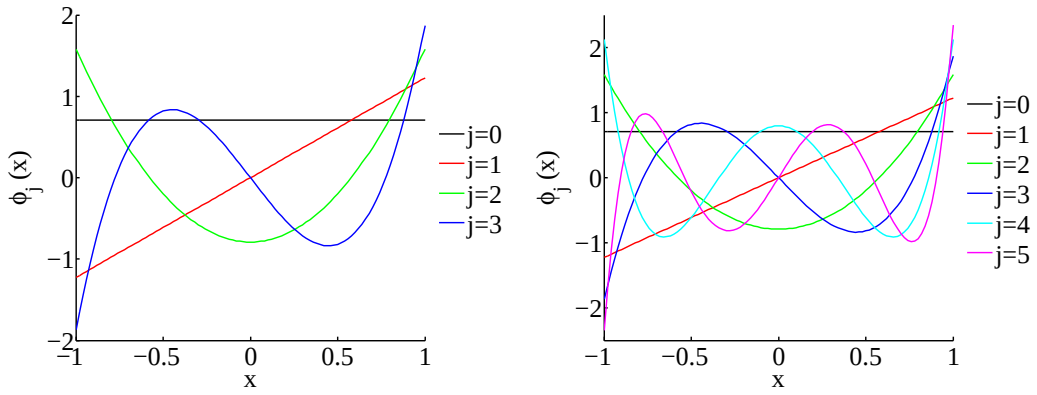

Figure 8: Orthonormal basis functions $\phi_j(x)$ on the interval for degree $p = 3$ (left) and $p = 5$ (right).

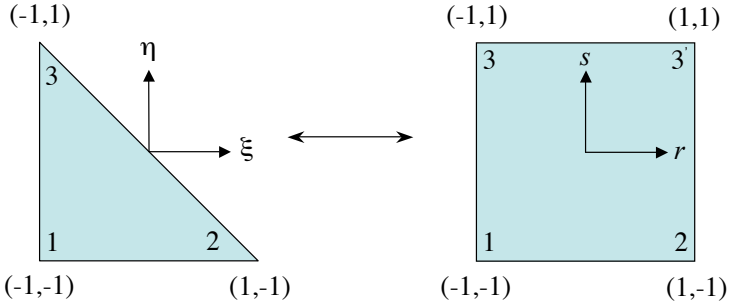

Figure 9: Mapping between canonical and collapsed coordinate element.

collapsed coordinates (or "warped products") [76, 53] as

$$\phi_{m(ij)}(r,s) = \sqrt{\frac{2i+1}{2}}\sqrt{\frac{2j+2i+2}{2}} P_i^{0,0}(r) P_j^{2i+1,0}(s) \left(\frac{1-s}{2}\right)^i \tag{48}$$

where

$$r = 2\frac{1+x}{1-y} - 1, \quad s = y \quad \longleftrightarrow \quad x = \frac{(1+r)(1-s)}{2} - 1, \quad y = s \tag{49}$$

as shown in Figure 9. Derivatives are found by the chain rule as

$$\begin{aligned} \frac{\partial}{\partial x} &= \frac{\partial r}{\partial x}\frac{\partial}{\partial r} + \frac{\partial s}{\partial x}\frac{\partial}{\partial s} = \frac{2}{1-s}\frac{\partial}{\partial r} \\ \frac{\partial}{\partial y} &= \frac{\partial r}{\partial y}\frac{\partial}{\partial r} + \frac{\partial s}{\partial y}\frac{\partial}{\partial s} = \frac{1+r}{1-s}\frac{\partial}{\partial r} + \frac{\partial}{\partial s} \end{aligned} \tag{50}$$

The Jacobi polynomials $P_j^{\alpha,\beta}(x)$ satisfy an orthogonality condition in the weighted inner product

$$\int_{-1}^{+1} \left(\frac{1-x}{2}\right)^\alpha \left(\frac{1+x}{2}\right)^\beta P_i^{\alpha,\beta}(x) P_j^{\alpha,\beta}(x)\, dx = h_i^{\alpha,\beta}\delta_{ij} \tag{51}$$

where the scale $h_i^{\alpha,\beta}$ is

$$h_i^{\alpha,\beta} = \frac{2}{2i+\alpha+\beta+1}\frac{(i+\alpha)!(i+\beta)!}{i!(i+\alpha+\beta)!} \tag{52}$$

Well-known recursion formulae exist for the polynomials and their derivatives:

$$\begin{aligned} P_0^{\alpha,\beta}(x) &= 1 \\ P_1^{\alpha,\beta}(x) &= \frac{1}{2}\left(2(\alpha+1)+(\alpha+\beta+2)(x-1)\right) \\ a_1 P_{m+1}^{\alpha,\beta}(x) &= a_2 P_m^{\alpha,\beta}(x) + a_3 P_{m-1}^{\alpha,\beta}(x) \end{aligned} \tag{53}$$

where

$$\begin{aligned} a_1 &= 2(m+1)(m+\alpha+\beta+1)(2m+\alpha+\beta) \\ a_2 &= (2m+\alpha+\beta+1)(\alpha^2-\beta^2) \\ &\quad + (2m+\alpha+\beta)(2m+\alpha+\beta+1)(2m+\alpha+\beta+2)x \\ a_3 &= -2(m+\alpha)(m+\beta)(m_\alpha+\beta+2) \end{aligned} \tag{54}$$

and

$$b_1 \frac{\mathrm{d}}{\mathrm{d}x} P_m^{\alpha,\beta}(x) = b_2 P_m^{\alpha,\beta}(x) + b_3 P_{m-1}^{\alpha,\beta}(x) \tag{55}$$

where

$$\begin{aligned} b_1 &= (2m+\alpha+\beta+1)(1-x^2) \\ b_2 &= m[\alpha-\beta-(2m+\alpha+\beta)x] \\ b_3 &= 2(m+\alpha)(m+\beta) \end{aligned} \tag{56}$$

Other useful relations are

$$\frac{\mathrm{d}}{\mathrm{d}x} P_m^{\alpha,\beta} = \frac{m+\alpha+\beta+1}{2} P_{m-1}^{\alpha+1,\beta+1} \tag{57}$$

$$(2m+\alpha+\beta)P_m^{\alpha,\beta-1} = (m+\alpha+\beta)P_m^{\alpha,\beta} + (m+\alpha)P_{m-1}^{\alpha,\beta} \tag{58}$$

While the Jacobi and related Koornwinder-Dubiner polynomials are directly used for the basis functions in this work, direct application of the Gram-Schmidt procedure provides great utility as well.

2.3.2 Node Selection

For a given basis, Fekete points are the set of points that maximize the determinant of V. Evidence suggests that Fekete points are close to optimal in the sense that the Lebesgue constant is small [21]. Recall that the Lebesgue constant is used as an an polynomial interpolation quality indicator: it provides an upper bound on the worst possible pointwise error for the interpolant relative to the best possible pointwise approximation available at the same order. It turns out that on the interval, Fekete points are the Lobatto quadrature points. With Lobatto quadrature of order q, polynomials of degree $p = 2q - 3$ may be integrated exactly (up to machine precision). The endpoints are fixed in the total q points and the free $q - 2$ points are defined by the roots of

$$\frac{\mathrm{d}}{\mathrm{d}x} L_{q-1}(x) = 0 \quad \longrightarrow \quad P_{q-2}^{1,1}(x) = 0 \tag{59}$$

This is remarkably convenient to have a single set of points for both optimal interpolation and quadrature. Unfortunately on the triangle, this situation does not hold, as Fekete points in dimensions higher than one are decidedly not Guassian-type quadrature points.

The good news is that on the triangle, numerical evidence shows that Fekete points yield the one-dimensional Lobatto points on the boundaries [20]. This property of course simplifies the extraction of the boundary modal coordinates from the interior as described above. The question then becomes how to determine the Fekete point distribution, and several rich and diverse approaches exist. In one particularly well-known approach, Taylor, Wingate, and Vincent [70] utilize a steepest ascent algorithm to maximize the determinant of the Vandermonde matrix. In another, Hesthaven [42], recognizing that the Lobatto points on the interval coincide with the minimum energy configuration of electrostatic charges, extends the analogy to the triangle by solving a minimization problem for the electrostatic energy while enforcing the Lobatto configuration along the boundary. The present work employs a more recent strategy due to Warburton [77] that views the problem from the perspective of a coordinate warping transformation and results in an explicit construction of Fekete-like points. The results appear to be superior to other choices for degree $p \leq 10$. Figure 10 shows the node distributions on the canonical right triangle and the equilateral

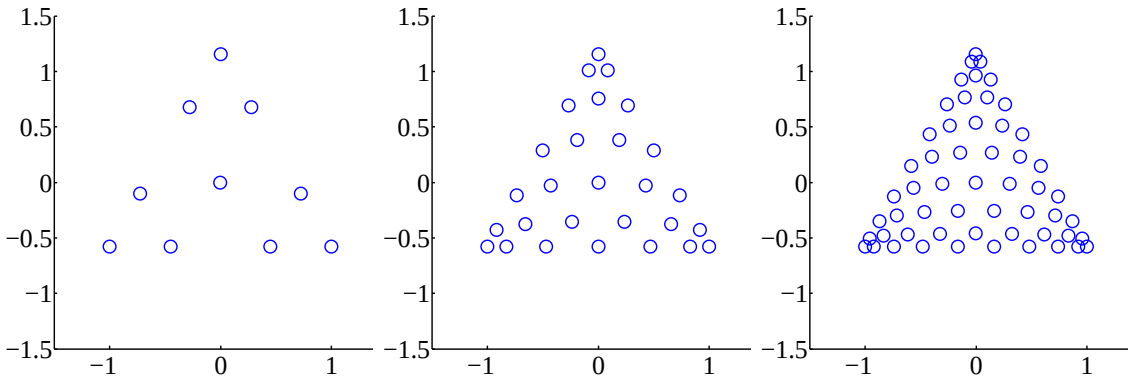

Figure 10: Fekete-like node distributions by the method of Warburton mapped to an equilateral triangle to show symmetry. Polynomial degree $p = 3, 6, 9$.

triangle.

As for the quadrature points on the triangle, the warped product form of the Koornwinder-Dubiner basis suggests a sound strategy: Lobatto points are used in the r-direction while Radu points are used in the s-direction of the collapsed coordinates to avoid the singularity at $s = 1$. With Radu quadrature of order q, polynomials of degree $p = 2q - 2$ may be integrated exactly (up to machine precision). The endpoint $x = -1$ is fixed in the total q points and the free $q - 1$ points are defined by the roots of:

$$\frac{L_{q-1}(x) + L_q(x)}{1 + x} = 0 \quad \longrightarrow \quad P^{0,1}_{q-1}(x) = 0 \tag{60}$$

Figure 11 shows the node distributions on the canonical right triangle and the equilateral triangle. It has been shown [35] that the collapsed Cartesian grid is overall the most efficient, particularly for high order of polynomial expansions, and the asymmetry of the quadrature points does not affect the accuracy of the numerical solution provided that a sufficient number of points is used.

2.3.3 Physical and Canonical Elements

The process of partitioning the global domain into non-overlapping, boundary conforming regions (*i.e.*, meshing or grid generation), naturally produces elements of various sizes, shapes, and orientations. For the required elemental operations such as inner products and differentiation, the individual physical elements are mapped to the canonical bi-unit element

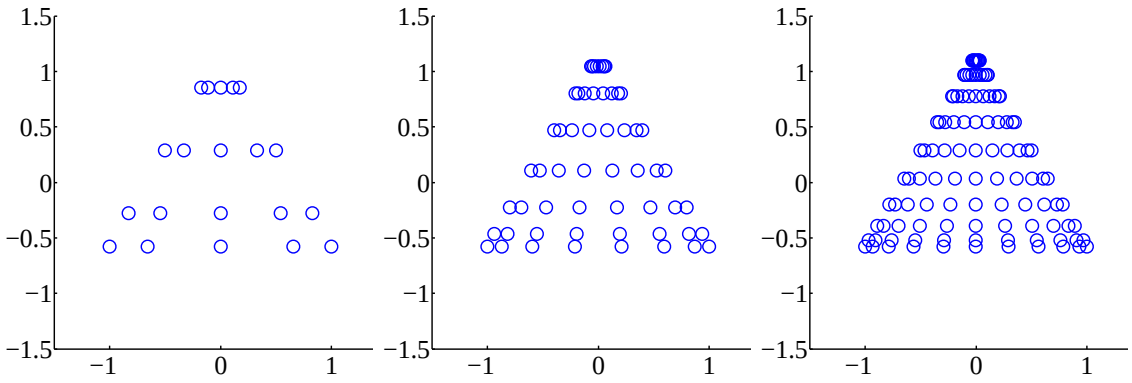

Figure 11: Quadrature node distribution mapped to an equilateral triangle to show symmetery. Polynomial degree $p = 3, 6, 9$.

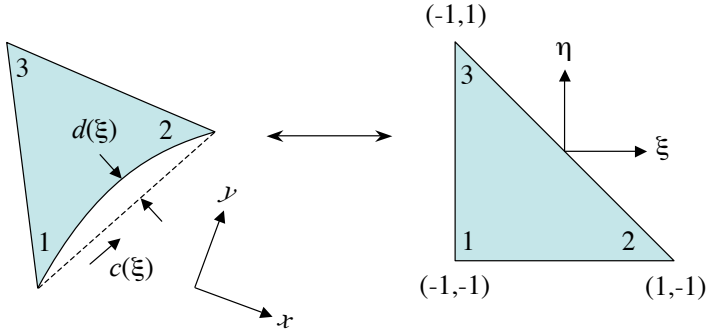

Figure 12: Mapping between physical and canonical element.

having local coordinates ξ, η. It is in the local ξ, η system that the physical geometry, basis functions, and nodes for the element are actually *defined* (see Figure 12).

Consider first a generic elemental inner product

$$\begin{aligned} \langle g, f \rangle &= \int_{\Omega} g(x,y) f(x,y)) \, \mathrm{d}x \, \mathrm{d}y \\ &= \int_{\Omega_c} g\left(x(\xi,\eta), y(\xi,\eta)\right) f\left(x(\xi,\eta), y(\xi,\eta)\right) J(\xi,\eta) \, \mathrm{d}\xi \, \mathrm{d}\eta \end{aligned} \tag{61}$$

where Ω_c is the canonical element and the Jacobian of the transformation from $x, y \in \Omega$ to $\xi, \eta \in \Omega_c$ is defined

$$J = \det \frac{\partial(x,y)}{\partial(\xi,\eta)} = x_\xi y_\eta - x_\eta y_\xi \tag{62}$$

For differentiation, the chain rule gives

$$\frac{\partial}{\partial \xi} = x_\xi \frac{\partial}{\partial x} + y_\xi \frac{\partial}{\partial y}, \quad \frac{\partial}{\partial \eta} = x_\eta \frac{\partial}{\partial x} + y_\eta \frac{\partial}{\partial y} \tag{63}$$

which can be solved by Cramer's rule for $\partial/\partial x, \partial/\partial y$. Alternatively, the chain rule could be applied as

$$\frac{\partial}{\partial x} = \xi_x \frac{\partial}{\partial \xi} + \eta_x \frac{\partial}{\partial \eta}, \quad \frac{\partial}{\partial y} = \xi_y \frac{\partial}{\partial \xi} + \eta_y \frac{\partial}{\partial \eta} \tag{64}$$

Comparing this later relation to the solution of the former relation yields the metrics of the transformation

$$\begin{aligned} \xi_x &= +J^{-1} y_\eta, \quad \eta_x = -J^{-1} y_\xi \\ \xi_y &= -J^{-1} x_\eta, \quad \eta_y = +J^{-1} x_\xi \end{aligned} \tag{65}$$

For straight-sided elements, locations in physical space x, y are found from parametric coordinates ξ, η by linear mapping of the element vertices $x_{(i)}, y_{(i)}$ in the usual way. For interval and triangular elements, respectfully, the mapping is

$$\begin{aligned} x_{\text{int}}(\xi) &= \frac{1-\xi}{2} x_{(1)} + \frac{1+\xi}{2} x_{(2)} \\ x_{\text{tri}}(\xi, \eta) &= -\frac{\xi+\eta}{2} x_{(1)} + \frac{1+\xi}{2} x_{(2)} + \frac{1+\eta}{2} x_{(3)} \end{aligned} \tag{66}$$

with analogous relations for the y coordinate. In two or more spatial dimensions, Bassi and Reaby [11] have shown that it is critical to conform to the curvature of the physical boundaries with an order of accuracy consistent with the discretization scheme. Obviously, this changes mesh generation strategies and techniques, and research on curved meshing is on-going (see [56] for example). For simplicity here, the Gordon-Hall blending [34] is employed for mapping a single curved side into a triangle. Considering side $x_{(1)-(2)}$ with the curve parameterized as $c(\xi)$ this takes the form

$$x(\xi, \eta) = x_\triangleleft(\xi, \eta) + d(\xi) \left(\frac{1-\eta}{2} \right)^n \tag{67}$$

where $x_\triangleleft(\xi, \eta)$ is the straight-sided triangle mapping above and the difference $d(\xi)$ is zero at the vertices $x_{(1)}, x_{(2)}$ and is blended inwards toward the remaining vertex $x_{(3)}$

$$d(\xi) = c(\xi) - \frac{1-\xi}{2} x_{(1)} - \frac{1+\xi}{2} x_{(2)} \tag{68}$$

Is convenient to represent the geometry of an element in the same basis as the solution on that element. Given the set of approximation nodes in parametric space $x(\xi_j, \eta_j), x(\xi_j, \eta_j)$,

the Vandermonde matrix is computed and the modal space representation is given as usual by

$$\begin{aligned} \bar{x} &= V^{-1}\vec{x} \\ \bar{y} &= V^{-1}\vec{y} \end{aligned} \tag{69}$$

From here, the procedure is to take the necessary derivatives in modal space, interpolate the result to a suitable set of quadrature nodes, form the Jacobian and the metrics point-wise, and finally use Galerkin projection back to modal space.

With the Jacobian and metrics in hand, attention is returned to the curved element. Substituting for f, g with their respective expansions shows

$$\begin{aligned} \langle g, f \rangle &= \int_{\Omega_c} g\left(x(\xi,\eta), y(\xi,\eta)\right) f\left(x(\xi,\eta), y(\xi,\eta)\right) J(\xi,\eta)\, \mathrm{d}\xi\, \mathrm{d}\eta \\ &= \sum_i \sum_j \left(\int_{\Omega_c} \phi_i(\xi,\eta)\phi_j(\xi,\eta) J(\xi,\eta)\, \mathrm{d}\xi\, \mathrm{d}\eta \right) \bar{g}_i \bar{f}_j \\ &= \sum_i \sum_j \bar{g}_i M_{J_{ij}} \bar{f}_j \end{aligned} \tag{70}$$

The mass matrix now has a weighted contribution from the Jacobian as

$$M_{J_{ij}} = \langle \phi_i, J\phi_j \rangle \tag{71}$$

If the Jacobian is constant there is no particular difficulty; however, if the Jacobian is non-constant (which is always the case for curved triangular elements) the basis is not orthonormal in the weighted inner product $\langle \phi_i, J\phi_j \rangle \neq \delta_{ij}$. Therefore the inner product is computed with numerical quadrature by combining the Jacobian with the quadrature weights as

$$W_{J_{ii}} = w_i J_i \tag{72}$$

The corresponding mass matrix and Galerkin projections are

$$M_J \approx B^T W_J B \tag{73}$$

$$\bar{f} = \left(B^T W_J B\right)^{-1} B^T W_J \vec{f}^{Q_J} \tag{74}$$

An alternative strategy is to convert the conservation law written in physical coordinates x, y to one written in generalized coordinates ξ, η. Following the manipulation due to

Viviand and Vinokur (see [69] for example), define the following new variables

$$\begin{aligned} u' &= Ju \\ f' &= J(\xi_x f + \xi_y g) \\ g' &= J(\eta_x f + \eta_y g) \end{aligned} \tag{75}$$

and the original conservation law can then be written in an identical form as

$$\frac{\partial u'}{\partial t} + \frac{\partial}{\partial \xi} f'(u') + \frac{\partial}{\partial \eta} g'(u') = 0 \tag{76}$$

Note that it is equally convenient to perform this change of variables after writing the DG variational form. Either way, at some point the true state may be recovered from the transformed state: by the equivalence of the two forms

$$\langle \phi_i, u \rangle_{\Omega_e} = \langle \phi_i, u' \rangle_{\Omega_c} \quad \longrightarrow \quad \mathbf{e}_{(i)}^T M_J \bar{u} = \mathbf{e}_{(i)}^T M \bar{u}' \tag{77}$$

it follows that

$$\bar{u} = M_J^{-1} M \bar{u}' \tag{78}$$

2.4 Dealing with Nonlinearity and Under-Resolution

Typically the flux functions $f(u), g(u)$ are nonlinear, and this presents some special challenges that are a direct result of representing the state u with an expansion of finite order p on an element of a finite size h (collectively, a finite resolution). One challenge is an under-sampling artifact generically known as aliasing, where high modes of an expansion masquerade as lower modes. If left uncontrolled, this non-physical allocation of modes across the spectrum of the expansion may lead to inaccuracy and eventually instability. Another challenge is that for hyperbolic conservation laws, discontinuous jumps in state (shocks) may develop in finite time. Any attempt to approximate features that are sharp beyond the nominal resolution of the approximation ultimately leads to the Gibbs phenomenon, the familiar overshoots ("ringing") of eigenfunction expansions near discontinuities.

2.4.1 De-Aliasing by Galerkin Projection with Over-Integration

For linear terms that require the inner product $\langle \phi, u \rangle$ with two polynomials of the same or lesser degree $\phi, u \in \mathcal{V}_p$, exact integration of the product requires $q_{\mathrm{L}} = p + 2$ Lobatto

quadrature points. However, for nonlinearities $\langle \phi, f \rangle$ where $\phi \in \mathcal{V}_p$ and $f \in \mathcal{V}_{3p}$ such as those found in the convective flux vector of the compressible Euler equations, exact integration of the product requires $q_{\text{NL}} = 2p+2$ points. For well-resolved functions, uniformly utilizing the linear inner product commits a "quadrature crime" with negligible consequence. However, for marginally- or under-resolved functions, the high mode energy of a nonlinear function can alias into the lower modes with disastrous results.

The de-aliasing procedure [49] is to transform the state from modal to physical space on the q_{NL} points, then form the nonlinear flux terms point-wise, and finally project the result back to the p degree modal space using the Galerkin projection. The aliasing situation is exacerbated on curved elements, where the non-constant Jacobian and metrics bring an additional level of nonlinearity with which to contend. In this case, the over-integration requirement is increased to $q_J > q_{\text{NL}}$ as necessary to accommodate the Jacobian. Figure 13 demonstrates the procedure for the nonlinearity $f(u) = u^3$ with $\bar{u}_j = 1/k$ for $j = 1, \ldots, k$ on a triangular element. In this case f *cannot* exactly represent the nonlinearity with the same number of modes as u. However, is clear that lower modes of f are corrupted in the collocation projection while they are relatively unaffected when using over-integration with Galerkin projection. The later case represents the best possible fit of f to the nonlinearity using the same number of modes as u.

As an aside, note that Galerkin projection with over-integration has the effect of sharp cutoff filtering. Explicitly writing the governing equation with the projection operator in place provides useful insight into how the problem is altered:

$$\frac{\partial}{\partial t}\mathbb{P}_k\tilde{u} + \frac{\partial}{\partial x}\mathbb{P}_k f(\mathbb{P}_k\tilde{u}) + \frac{\partial}{\partial y}\mathbb{P}_k g(\mathbb{P}_k\tilde{u}) = 0 \tag{79}$$

In general, it is expected that

$$\mathbb{P}_k\tilde{f}(\tilde{u}) - \mathbb{P}_k f(\mathbb{P}_k\tilde{u}) \neq 0 \tag{80}$$

and subsequently one *may* choose to model these type differences.

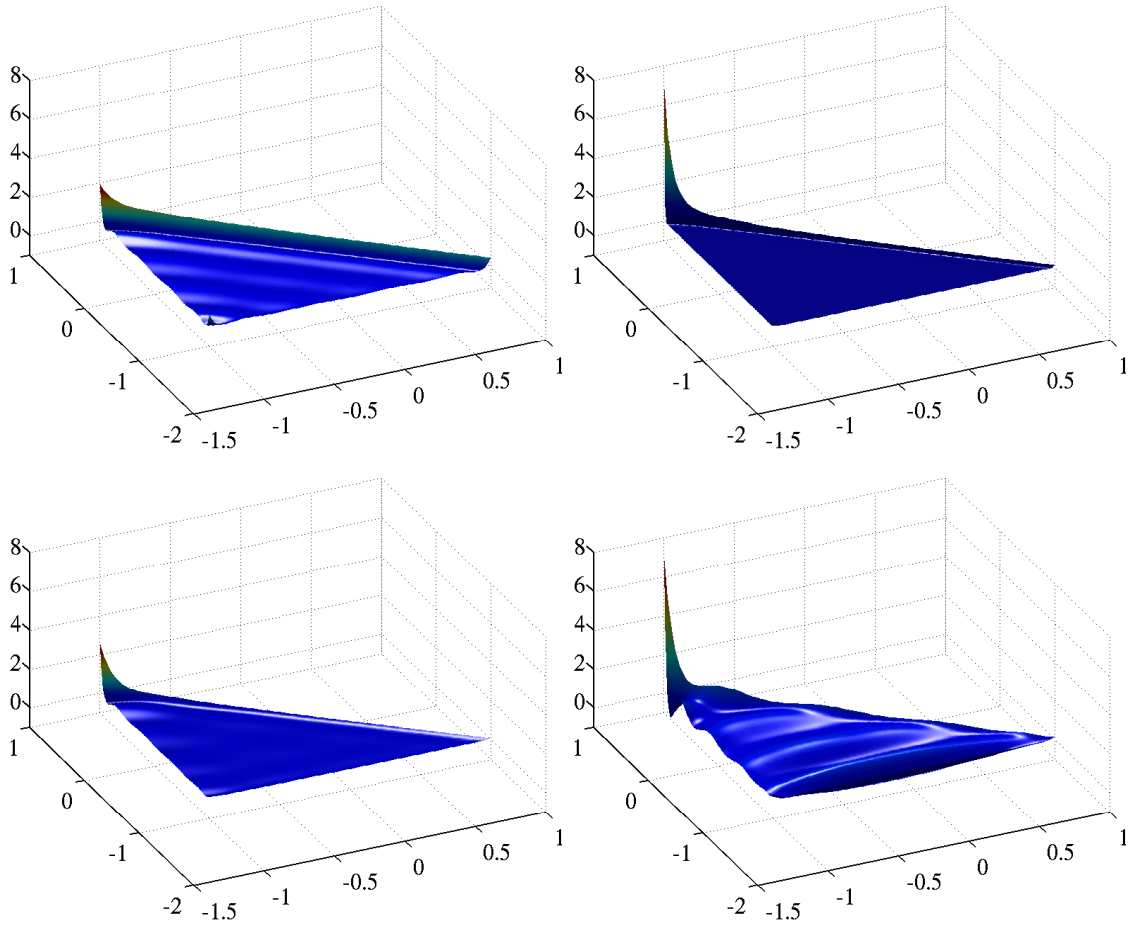

Figure 13: Dealiasing of nonlinearity $f(u) = u^3$ with $\bar{u}_j = 1/k$ for $j = 0, \ldots, k$. Clockwise from top-left: marginally resolved function u, exact value of u^3, $f(u)$ sampled at approximation nodes and collocation projection, $f(u)$ sampled at over-integration quadrature nodes and Galerkin projection.

2.4.2 Shock Capturing with Artificial Viscosity

It is well known that methods for hyperbolic conservation laws of order higher than one will oscillate in the vicinity of shocks. One common approach to this problem is known as slope limiting whereby one means or another the local solution order is essentially reduced. This forces the inter-element jumps to increase and relies on the numerical boundary trace function to provide damping. To offset the loss of accuracy, h refinement may be employed in these regions. Another strategy is to select a solution-dependent computational stencil that results in an essentially non-oscillatory (ENO) reconstruction.

For higher order polynomial approximations, one can *exploit* the sub-element resolution

to obtain shock profiles that are much thinner than the element but just wide enough to be adequately resolved by the underlying approximation expansion. The idea [64] – an old and simple approach tailored for the DG method – is to add a dissipative model term to the original equations the form

$$\begin{aligned} f_{\text{av}}(u) &= \epsilon \frac{\partial u}{\partial x} \\ g_{\text{av}}(u) &= \epsilon \frac{\partial u}{\partial y} \\ \frac{\partial u}{\partial t} + \frac{\partial}{\partial x} f(u) + \frac{\partial}{\partial y} g(u) &= \frac{\partial}{\partial x} f_{\text{av}}(u) + \frac{\partial}{\partial y} g_{\text{av}}(u) \end{aligned} \tag{81}$$

where ϵ controls the amount of viscosity, and $\epsilon = 0$ in smooth regions. By writing the modified equation as a system of first-order equations, the variational form and the resulting matrix operator counterpart is to each equation sequentially in a straightforward way.

For the greatest simplicity, ϵ is taken to be piecewise constant within each element. It is triggered whenever the high frequency components of the expansion do not decay at the expected rate for a smooth solution. This is accomplished by isolating the highest frequency modes $N(p)$ of the k term expansion for u and applying a sensor as

$$\hat{u} = \sum_{j \in N(p)} \bar{u}_j \phi_j, \quad s = \log_{10} \frac{\langle \hat{u}, \hat{u} \rangle}{\langle u, u \rangle} \tag{82}$$

The artificial viscosity ϵ is blended between zero and $\epsilon_{\max}$ based on the p^4 decay of this sensor as

$$\epsilon = \begin{cases} \epsilon_{\max} & \text{if } t > 1 \\ \frac{1}{2}\left(1 + \sin\left(\frac{1}{2}\pi t\right)\right)\epsilon_{\max} & \text{if } -1 \le t \le 1 \\ 0 & \text{else} \end{cases} \tag{83}$$

with

$$t = \frac{s - s_0}{\kappa}, \quad s_0 = \log_{10} \frac{c_{s_0}}{p^4}, \quad \epsilon_{\max} = \frac{c_\epsilon h}{p} \tag{84}$$

For the Euler equations, density is a suitable choice for the sensor variable u, and the following values for the adjustable parameters are found to give reliable performance

$$c_\epsilon = 1/2 \quad c_{s_0} = 1 \quad \kappa = 4 \tag{85}$$

No effort is made to improve upon this strategy, as it performs satisfactorily within the scope of the current effort. However, it is worth noting that the follow-on work [8, 62] utilizing a time-dependent PDE for the artificial viscosity appears to be a significant improvement and assimilates the artificial viscosity within the common DG framework used for all other quantities.

2.5 Implementation of DG for the Euler Equations

With the tools now in place, focus is now shifted to the solution of the Euler equations of fluid dynamics using the discontinuous Galerkin method. There is no requirement to alter or otherwise tailor the DG-specific developments so far to this particular application. Instead, the following specifies the conservation laws and the associated numerical flux functions and boundary conditions. Additionally, the simple explicit Runge-Kutta time integration schemes is detailed.

2.5.1 Governing Equations

The coupled equations of motion that express conservation of mass, momentum, and energy in flux vector (strong conservation) form are given by the system

$$\frac{\partial U}{\partial t} + \frac{\partial}{\partial x} F(U) + \frac{\partial}{\partial y} G(U) = 0 \tag{86}$$

The state and flux vectors are given by

$$U = \left\{ \begin{array}{c} \rho \\ \rho u \\ \rho v \\ \rho e_0 \end{array} \right\} \quad F = \left\{ \begin{array}{c} \rho u \\ \rho u u + p \\ \rho v u \\ (\rho e_0 + p) u \end{array} \right\} \quad G = \left\{ \begin{array}{c} \rho v \\ \rho u v \\ \rho v v + p \\ (\rho e_0 + p) v \end{array} \right\} \tag{87}$$

where ρ is the density, u, v are the components of the velocity vector, p is the pressure, and e_0 is the total energy. The system is closed with the equation of state

$$p = (\gamma - 1) \left(\rho e_0 - \rho \frac{u^2 + v^2}{2} \right) \tag{88}$$

where $\gamma = c_p / c_v$ is the ratio of specific heats and is related to the gas constant by $R = c_p - c_v$. The matrix form of the DG variational statement is simply applied to each equation of this

system, a task most easily accomplished by treating the the state and flux "vectors" as a matrices, having modal coordinates along rows and equations along columns.

2.5.2 Numerical Flux Functions

Due to the discontinuous space and individual elements, the numerical flux function provides the necessary communication of flow information between elements on the "left" and "right" sides of a given interface. Traditionally, with the focal element Ω_e and corresponding outward unit normal traditionally designated as the L-side and the neighbor element Ω_b is designated as the R-side. At a minimum, the numerical flux function must satisfy the consistency relations

$$\begin{aligned} \mathcal{F}_n(U,U) &= F_n(U) \\ \mathcal{F}_n(U^L,U^R) &= -\mathcal{F}_n(U^R,U^L) \end{aligned} \tag{89}$$

For the state and viscous flux traces that appear through the use of artificial viscosity, simple averages are used

$$\mathcal{U} = \frac{U^L + U^R}{2} \tag{90}$$

$$\mathcal{F}_n^{\text{av}} = \frac{F_n^{\text{av}}(U^L) + F_n^{\text{av}}(U^R)}{2} \tag{91}$$

Many other choices exist for the viscous flux function and Arnold *et al.* [6] provides an in-depth discussion.

On the other hand, the inviscid flux normal trace is constructed with techniques traditionally used in upwind finite volume schemes. Many choices exist, such as those due to Godunov, Lax-Friedrichs, Roe, van Leer, Zha-Bilgen, Harten-Lax-van Leer, and many others (see [52] and references therein for details). However in contrast to finite volume methods, the particular choice of flux function becomes less important for at least two reasons. First, the interface integral does not carry the entire burden for the element update. Second, the inter-element solution jumps become increasingly small at an exponential rate with increasing order of the DG approximating space. Therefore, due consideration must be given to the sophistication, difficulty of implementation, and cost of computation. It turns out that the Lax-Friedrichs flux performs quite well compared to other traditional

and more complex functions. The function is given by

$$\mathcal{F}_n = \frac{F_n(U^L) + F_n(U^R)}{2} + \lambda_{\max}\frac{U^L - U^R}{2} \tag{92}$$

where with interface normal velocity u_n and acoustic speed a, the upwinding parameter $\lambda_{\max} = |u_n| + a$ is the maximum eigenvalue of the flux Jacobian $\det[\partial F_n/\partial U]$.

2.5.3 Boundary Conditions

One attractive feature of the DG method is that all boundary integrals, including those conforming to the global physical domain, are enforced weakly through the numerical flux functions. By analogy to the ghost cell technique of some finite volume methods, physical boundary conditions utilize a ghost edge upon which the state and normal flux vectors are constructed. These ghost edges are simply formed on-the-fly from the target element edge data and operators and passed to the numerical flux function. In this way, boundary conditions are entirely consistent with the accuracy of the internal solution.

For the Euler equations, the present work includes periodic, extrapolation, specified, and slip wall boundary conditions, with the first three requiring no special considerations whatsoever. The periodic condition is nothing more than the usual contiguous element interface connectivity artificially specified by the user during setup. The extrapolation condition is to simply copy the state and fluxes (with opposite normal sign) from the target edge to the ghost edge, effectively forcing the boundary trace inner product term to zero. For the specified condition, set the state from the given primitive varibales, compute the corresponding inviscid normal flux vector, and extrapolate the artificial viscous normal flux from the interior of the target element. For the inviscid slip wall condition, mirror the momentum vector about the wall tangent vector and set the viscous normal flux to zero.

2.5.4 Explicit Time Stepping

While the numerical solution of unsteady problems is of great interest, this work is squarely focused on spatial resolution. Furthermore, since the ultimate goal of the current development is groundwork for the simulation of turbulent flows, highly restrictive time step requirements are expected in practice. Such applications negate the advantageous stability

gains of implicit methods while retaining their complication and expense. Therefore, only the simplest explicit time integration methods – the Runge-Kuta multistage schemes – are considered.

Starting with the residual form of the generic conservation law

$$\frac{\mathrm{d}\bar{u}}{\mathrm{d}t} = \mathcal{R}(\bar{u}) \tag{93}$$

with the right-hand side

$$\mathcal{R}(\bar{u}) = -D_x\bar{f} - D_y\bar{g} - \sum_b S_{(b)} \left(\bar{\mathcal{F}}_{n\,(b)} - \bar{f}_{n\,(b)}\right) \tag{94}$$

explicit Runge-Kutta multistage schemes may be written [7] as

$$\begin{aligned} w^i &= u^n + \Delta t \sum_{j=1}^{s} a_{ij} \mathcal{R}(w^{j-1}, t_n + c_j \Delta t) \\ u^{n+1} &= u^n + \Delta t \sum_{j=1}^{s} b_j \mathcal{R}(w^{j-1}, t_n + c_j \Delta t) \end{aligned} \tag{95}$$

with $a_{ij} = 0$ for $j \geq i$ and $c_i = \sum_{j=1}^{s} a_{ij}$. Suppress the explicit dependence of the residual on t, and select among the infinite possibilities methods having intermediate approximations based solely on the previous approximation, i.e., $a_{ij} = 0$ for $i \neq j-1$ such that $a_{ij} \to a_i$. The previous relations simplify to

$$\begin{aligned} w^0 &= u^n \\ w^1 &= u^n + a_1 \Delta t\, \mathcal{R}(w^0) \\ &\vdots \\ w^j &= u^n + a_j \Delta t\, \mathcal{R}(w^{j-1}) \\ &\vdots \\ w^{s-1} &= u^n + a_{s-1} \Delta t\, \mathcal{R}(w^{s-2}) \\ u^{n+1} &= u^n + \Delta t \sum_{j=1}^{s} b_j \mathcal{R}(w^{j-1}) \end{aligned} \tag{96}$$

Familiar schemes in this family are the first-order Forward Euler method

$$\begin{aligned} a_1 &= 0 \\ b_1 &= 1 \end{aligned} \tag{97}$$

the second-order "explicit trapezoidal" method

$$\begin{aligned} a_1 &= 1 \\ b_1 = \frac{1}{2}, \quad b_2 &= \frac{1}{2} \end{aligned} \tag{98}$$

and the classical fourth-order method (reminiscent of Simpson's rule)

$$\begin{aligned} a_1 = \frac{1}{2}, \quad a_2 = \frac{1}{2}, \quad a_3 &= 1 \\ b_1 = \frac{1}{6}, \quad b_2 = \frac{2}{6}, \quad b_3 = \frac{2}{6}, \quad b_4 &= \frac{1}{6} \end{aligned} \tag{99}$$

In terms of storage, two time levels of the solution and the cumulative sum of right-hand side evaluations at the intermediate stages are retained.

As noted by Yee [82], the choice of temporal scheme may be dictated by the user's interest in a variety of often conflicting characteristics. Schemes with high order accurate phase error may have a lower formal order of accuracy when measured in the standard norm. Furthermore, a particular combination of spatial and temporal discretization may impose excessively small timestep constraints for the overall system. Ongoing research considers these factors for optimal compatibility resulting in low phase and amplitude error for unsteady problems. Nevertheless, for all of the example problems considered in this work, the classical fourth-order method above performs well.

As a minimum, the timestep used in an explicit scheme must satisfy a von Neumann stability analysis of the linear wave equation

$$\frac{\partial u}{\partial t} + \frac{\partial}{\partial x}(cu) = 0 \tag{100}$$

The result is the familiar Courant-Freidrichs-Levy criteria

$$|c|\frac{\Delta t}{\Delta x} \leq \text{CFL} \tag{101}$$

For the high order spatial DG scheme, the CFL number has been shown [23] to vary as $\text{CFL}(p) = (2p+1)^{-1}$. All of the computations in this work use this criteria with global wavespeed $\lambda_{\max}$ and an additional safety factor of $1/2$ on the CFL number.

2.5.5 Normalization

It is convenient and good practice to normalize the flow variables. Assuming for simplicity uniform $R = R_\infty$ and $\gamma = \gamma_\infty$ choose

$$\begin{gathered} x^\dagger = \frac{x}{L}, \qquad t^\dagger = \frac{t a_\infty}{L}, \qquad u^\dagger = \frac{u}{a_\infty} \\ \rho^\dagger = \frac{\rho}{\rho_\infty}, \qquad p^\dagger = \frac{p}{\rho_\infty a_\infty^2} = \frac{p}{\gamma p_\infty}, \quad T^\dagger = \frac{T R_\infty}{a_\infty^2} = \frac{T}{\gamma T_\infty} \\ e^\dagger = \frac{e}{a_\infty^2}, \quad c_p^\dagger = \frac{c_p}{R_\infty} = \frac{\gamma}{\gamma - 1}, \quad c_v^\dagger = \frac{c_v}{R_\infty} = \frac{1}{\gamma - 1} \end{gathered} \tag{102}$$

This maintains the form of important thermodynamic relations:

$$p^\dagger = (\gamma - 1)\rho^\dagger e^\dagger, \quad a^\dagger = \sqrt{\frac{\gamma p^\dagger}{\rho^\dagger}}, \quad e^\dagger = c_v^\dagger T^\dagger \tag{103}$$

This work will drop the notation $(\cdot)^\dagger$ and assume that all flow variables are normalized, noting that the process does not introduce additional parameters into the Euler equations. This is in contrast to the situation for the compressible Navier-Stokes equations, where the particular choice affects the final form of the viscous terms that always contain at least a Reynolds number.

2.6 Numerical Examples

The effectiveness of the discontinuous Galerkin method is now demonstrated by application to several simple yet illustrative problems for the Euler equations in one and two spatial dimensions. First, the accuracy of the method for the preservation of smooth solutions is shown by the time evolution of a 1D acoustic pulse in a quiescent background and a 2D isentropic vortex superimposed on a nominal mean flow. Problems of this class provide a simple means for evaluating the performance of a method as the exact solution is simply the passive convection of the initial feature. Second, the shock-capturing capability of the artificial viscosity procedure is shown with the classical 1D Sod shock tube and steady-state 2D supersonic wedge flow. These problems have exact solutions that provide a datum for the quality of the sub-element resolution for moderately thickened shock profiles. Finally, the high accuracy of the method on curved domains is highlighted with the steady-state solution of subsonic flow over a cylinder in a channel. All cases use the fourth-order Runge-Kutta scheme and a timestep restricted by a CFL factor of one-half: $\Delta t \leq \frac{1}{2}\mathrm{CFL}(p)\sqrt{|\Omega_e|_{\min}}/\lambda_{\max}$.

2.6.1 Acoustic Pulse

Given an otherwise quiescent one-dimensional state, an acoustic pulse is introduced by small perturbations in velocity, pressure, and density [79]. The resulting unsteady flow is characterized by the passive convection of the pulse by a uniform acoustic speed such that the size and strength of the pulse are preserved at the initial values for all time. The freestream values are

$$u_\infty = 0, \quad p_\infty = 1/\gamma, \quad \rho_\infty = 1 \tag{104}$$

which gives an acoustic speed $a_\infty = 1$. Perturbations are added to the flow as

$$\Delta u = \frac{\partial \phi}{\partial x}, \quad \Delta p = -\rho_\infty \frac{\partial \phi}{\partial t}, \quad \Delta \rho = -\frac{\rho_\infty}{a_\infty^2} \frac{\partial \phi}{\partial t} \tag{105}$$

where the acoustic potential is defined

$$\phi(x,t) = A \exp\left[-\left(\frac{x - x_c - a_\infty t}{x_w} \right)^2 \right] \tag{106}$$

At the initial time $t = 0$

$$f = \left. \frac{\partial \phi}{\partial x} \right|_{t=0} = - \left. \frac{\partial \phi}{\partial t} \right|_{t=0} = -2A \frac{x - x_c}{x_w^2} \exp\left[-\left(\frac{x - x_c}{x_w} \right)^2 \right] \tag{107}$$

For computational efficiency, this problem is typically defined on suitably large a periodic domain.

The following parameters are chosen: $A = 1.e-5$, $x_w = 0.4$, and $x \in (-1, 1)$. Time-dependent solutions are obtained at a timestep of $\Delta t = 1.e-3$. Figure 28 shows the time evolution of density for a high order degree $p = 9$ solution on $N = 4$ elements. Note that the pulse returns to the starting position in the domain at the correct time dictated by an acoustic wavespeed of one. Figure 15 shows convergence for the norm of density error at the initial condition in terms of expansion degree and number of elements.

2.6.2 Isentropic Vortex

The isentropic vortex is a two-dimensional perturbation of velocity components and temperature in a uniform mean flow [32, 82]. The resulting unsteady flow is characterized by the

passive convection of the vortex by the mean velocity field such that the size and strength of the vortex are preserved at the initial values for all time. The freestream values are

$$u_\infty = M_\infty \cos\alpha, \quad v_\infty = M_\infty \sin\alpha, \quad p_\infty = 1/\gamma, \quad T_\infty = 1/\gamma \tag{108}$$

which gives a density $\rho_\infty = 1$ and an acoustic speed $a_\infty = 1$. Perturbations are added to the flow as

$$\Delta u = -\Delta y f, \quad \Delta v = +\Delta x f, \quad \Delta T = -\frac{\gamma - 1}{2\gamma} f^2 \tag{109}$$

where the vortex potential is defined

$$f = \frac{B}{2\pi} \exp\left[A\left(1 - r^2\right)\right], \quad r^2 = \Delta x^2 + \Delta y^2 \tag{110}$$

The pressure is computed via the isentropic relation

$$p = p_\infty \left(\frac{T}{T_\infty}\right)^{\frac{\gamma}{\gamma-1}} = \frac{1}{\gamma}(\gamma T)^{\frac{\gamma}{\gamma-1}} \tag{111}$$

This problem is typically defined on suitably large a doubly-periodic domain.

The following parameters are selected: $A = 0.3$, $B = 5$, and $x, y \in (-5, 5) \times (-5, 5)$. The freestream Mach number is taken as $M_\infty = 0.5$. Time-dependent solutions are obtained on a $N = 32$ element mesh at timestep of $\Delta t = 1.e - 2$. Figure 16 shows the time evolution of density for a high order degree $p = 7$ solution. The vortex returns to the starting position in the center of the domain at the correct time dictated by the freestream convection speed.

Figure 17 shows exponential convergence for the norm of density error. However, the total degrees of freedom is a more meaningful independent variable for elucidating the efficiency of high order over low-order. Figure 18 provides a comparison of various N, p combinations in terms of DoF by plotting density error norm and wallclock time per core diameter convected. Note that using wallclock per core diameter rather than walllclock per step accounts for changes in timestep due to the CFL restriction on both element size and expansion degree. The timings are normalized by the lowest error case (N=2048 elements of degree p=9). Given that the timestep is selected relative to the CFL condition as a choice of four values per decade (*viz*, 1, 2, 5, 8), it is remarkable that the all of the timing curves nearly collapse to a single line. This indicates that run-time cost is a function of

DoF only, and that accuracy is then driven by expansion degree. As an example of the greater efficiency provided by high order, consider a target density error norm of 1.e-5. The decrease in DoF required to hold the target error while increasing the expansion degree from $p = 1$ to degrees $p = 3, 5, 9$ is approximately $0.211, 0.114, 0.075$, respectively. This in turn results in decreased wallclock times of approximately $0.166, 0.023, 0.015$, respectfully.

2.6.3 Shock Tube

The shock tube is a one-dimensional problem in which two initially separate and stagnant regions of fluid having different states interact instantaneously. The resulting unsteady flow features a shock, a contact discontinuity, and an expansion each moving at steady speeds and separating regions of otherwise uniform flow. The different uniform states are dictated by the time evolution of the system characteristics and the Rankine-Hugoniot relation provides the shock jump conditions. The exact solution for the entire tube as a function of time after can be found by iterative means [5]. For the Sod shock tube problem, the initial conditions are

$$\begin{aligned} \rho = 1, \quad u = 0, \quad p = 1, \quad x \in (-1, 0) \\ \rho = 0.125, \quad u = 0, \quad p = 0.1, \quad x \in [0, 1) \end{aligned} \tag{112}$$

Time-dependent solutions are obtained on a 16 element mesh at timestep of $\Delta t = 2.e{-}4$. Figure 30 shows the time evolution of density for degree $p = 9$ elements. Figure 20 shows density at the final time using degree $p = 3, 9$ elements. The ability to *exploit* the high order sub-cell resolution for relatively thin shock profiles is evident: the slip line and shock are captured within the boundaries of a single element in both cases, with the high order case providing much less smearing of these density jumps.

2.6.4 Supersonic Wedge

An oblique shock forms when two-dimensional supersonic flow is turned into itself, such as by the streamline deflection caused by the impermeable wall of a wedge. Given an upstream Mach number M_1, shock wave angle β, and wedge turning angle θ, the following relation holds [51]

$$\theta = \beta - \tan^{-1}\left[\frac{1}{\sin\beta\cos\beta}\left(\frac{\gamma-1}{\gamma+1}\sin^2\beta + \frac{2}{\gamma-1}\frac{1}{M_1^2}\right)\right] \tag{113}$$

The shock wave angle is found by iteration and used to compute the Mach number in coordinates normal to the shock

$$M_{1n} = M_1 \sin\beta \tag{114}$$

The pressure ratio across the shock is subsequently

$$\frac{p_2}{p_1} = \frac{2\gamma}{\gamma+1} M_{1n}^2 - \frac{\gamma-1}{\gamma+1} \tag{115}$$

The freestream values are

$$u_\infty = M_\infty \cos\alpha, \quad v_\infty = M_\infty \sin\alpha, \quad p_\infty = 1/\gamma, \quad T_\infty = 1/\gamma \tag{116}$$

which gives a density $\rho_\infty = 1$ and an acoustic speed $a_\infty = 1$.

Steady-state solutions are obtained for the condition $M = 3.15$ and $\alpha = 0$ on a 20 element mesh. Figure 21 shows steady-state pressure contours for degree $p = 3, 9$ elements. Again, the ability to exploit the high order sub-cell resolution for relatively thin shock profiles is demonstrated by the complete capture of the shock within the boundaries of a single element. Note that this is a clear advantage over traditional finite volume methods in which a shock is always smeared over several elements due to the dependence of the reconstruction on an external stencil.

2.6.5 Subsonic Cylinder

Two dimensional steady, inviscid, subsonic flow over a cylinder in a channel is both adiabatic and irrotational; therefore changes in entropy should remain zero everywhere. Taking the freestream as the datum state, the change in entropy is [67]

$$\Delta s = \frac{1}{\gamma-1} \ln \frac{p/p_\infty}{(\rho/\rho_\infty)^\gamma} = \frac{1}{\gamma-1} \ln \frac{\gamma p}{\rho^\gamma} \tag{117}$$

The freestream values are

$$u_\infty = M_\infty \cos\alpha, \quad v_\infty = M_\infty \sin\alpha, \quad p_\infty = 1/\gamma, \quad T_\infty = 1/\gamma \tag{118}$$

which gives a density $\rho_\infty = 1$ and an acoustic speed $a_\infty = 1$.

Steady-state solutions are obtained for the representative subsonic condition $M = 0.2$ and $\alpha = 0$ on a $N = 32$ element mesh with *curved* boundaries. Figure 22 shows steady-state x-momentum contours for degree $p = 3, 7$ elements. The asymmetry in the contours

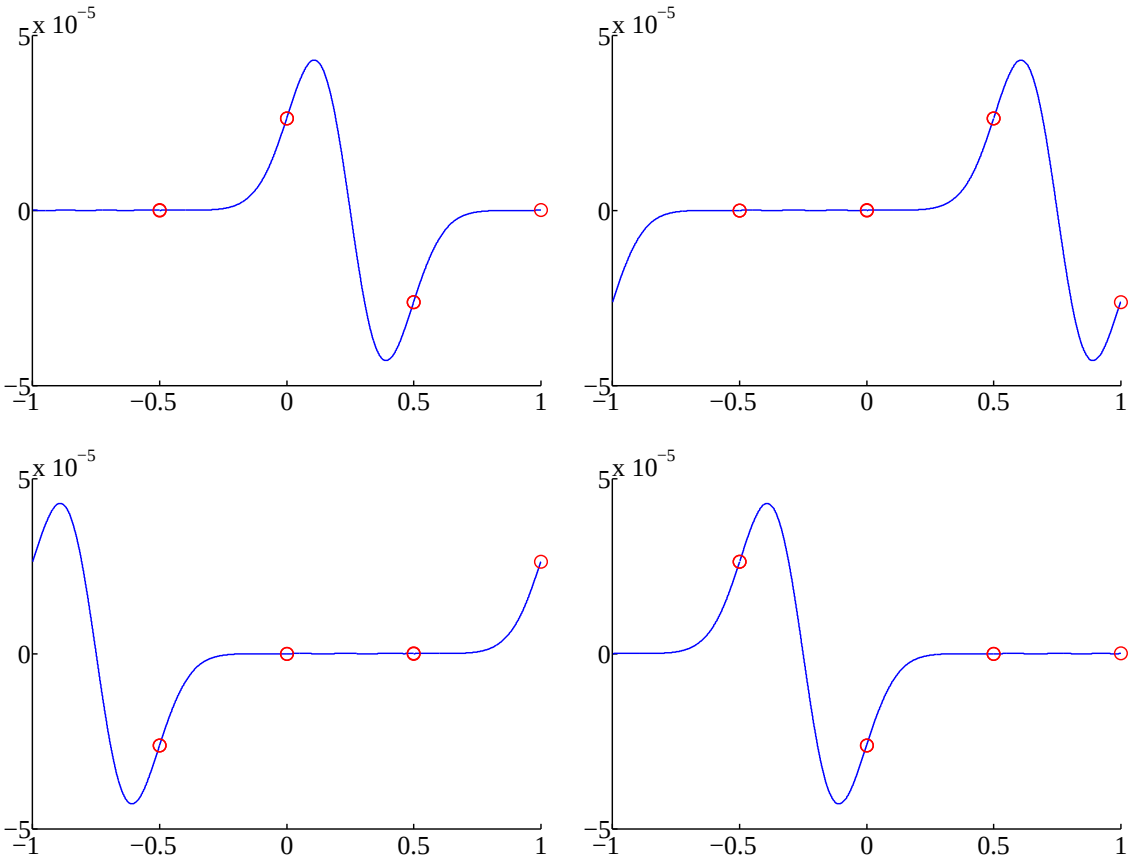

Figure 14: Time evolution of an acoustic pulse (x-momentum) on $N = 4$ elements of degree $p = 9$. Markers indicate element boundaries.

indicates the generation of non-physical entropy in the lower-order solution. Figure 23 shows exponential convergence for the norm of entropy error at steady state.

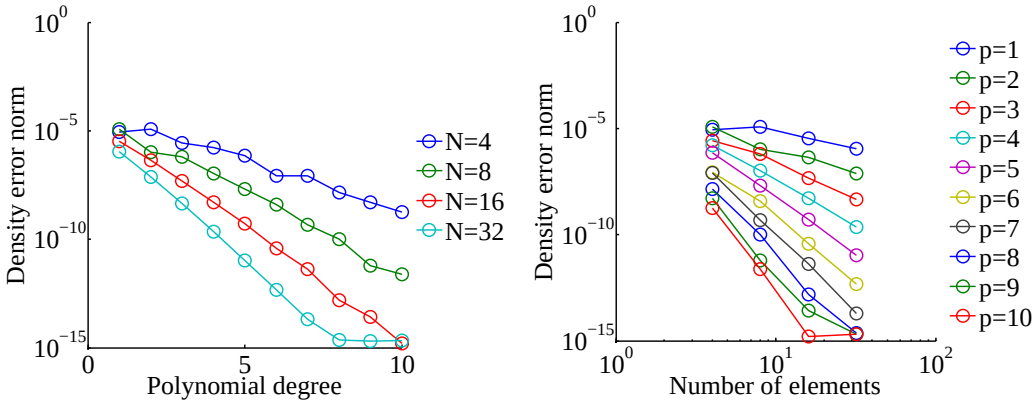

Figure 15: Density error norm convergence for the acoustic pulse initial condition. Convergence is exponential in polynomial expansion degree.

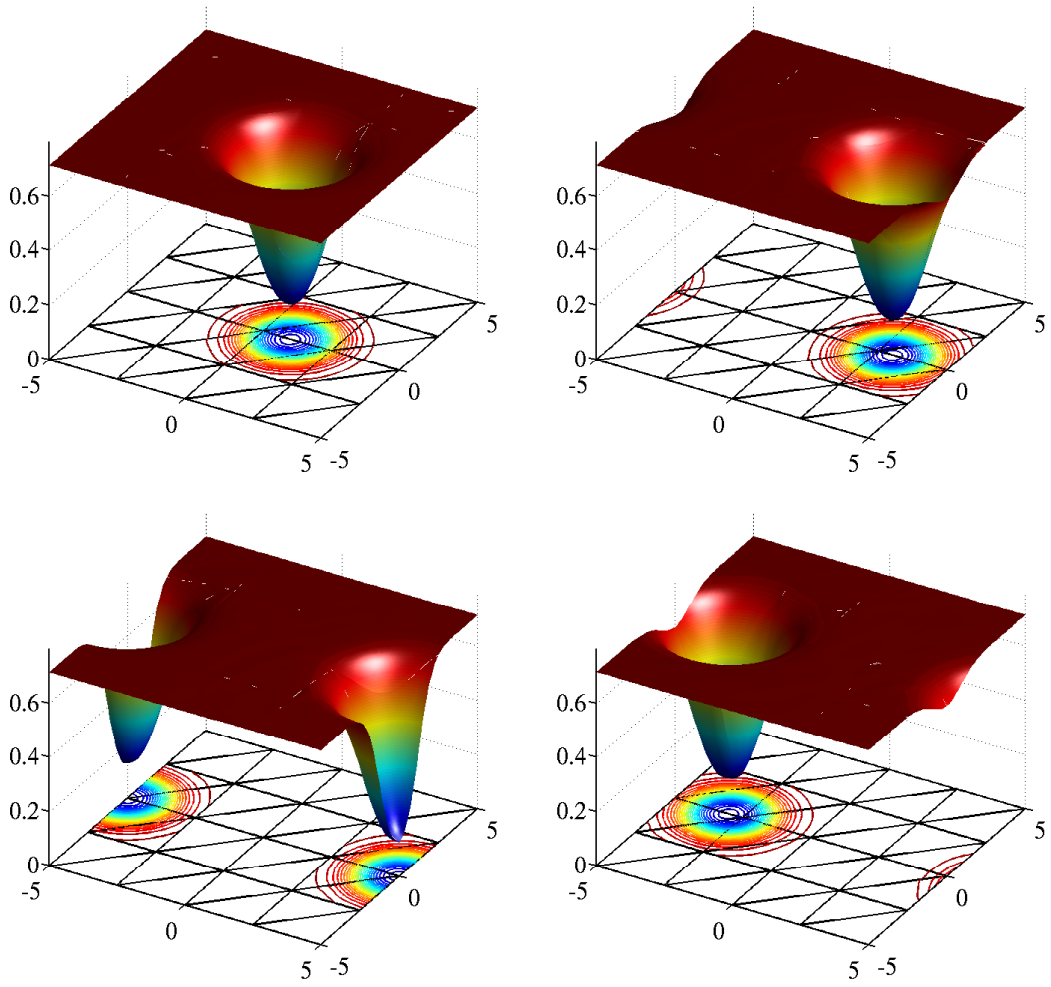

Figure 16: Time evolution of an isentropic vortex (pressure) on $N = 32$ elements of degree $p = 7$.

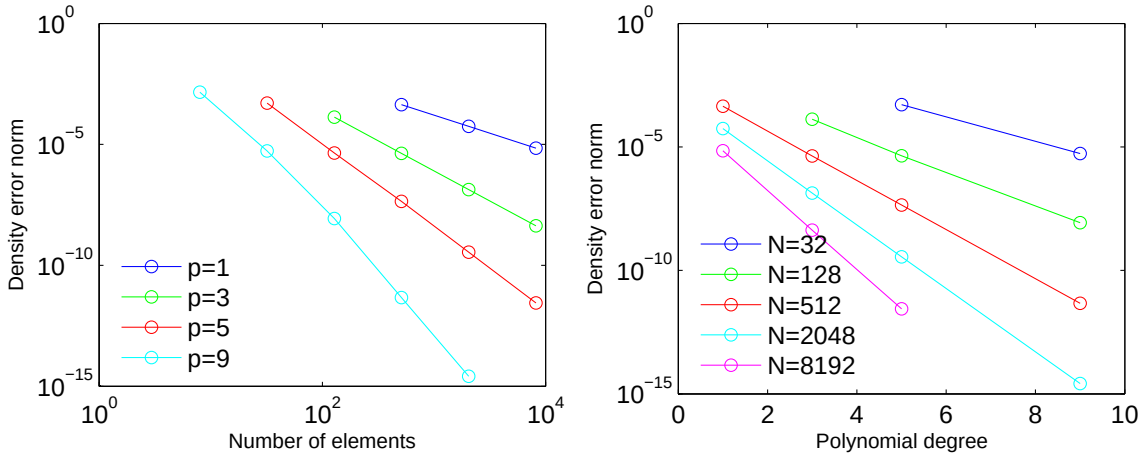

Figure 17: Density error norm convergence for the isentropic vortex initial condition. Convergence is exponential in polynomial expansion degree.

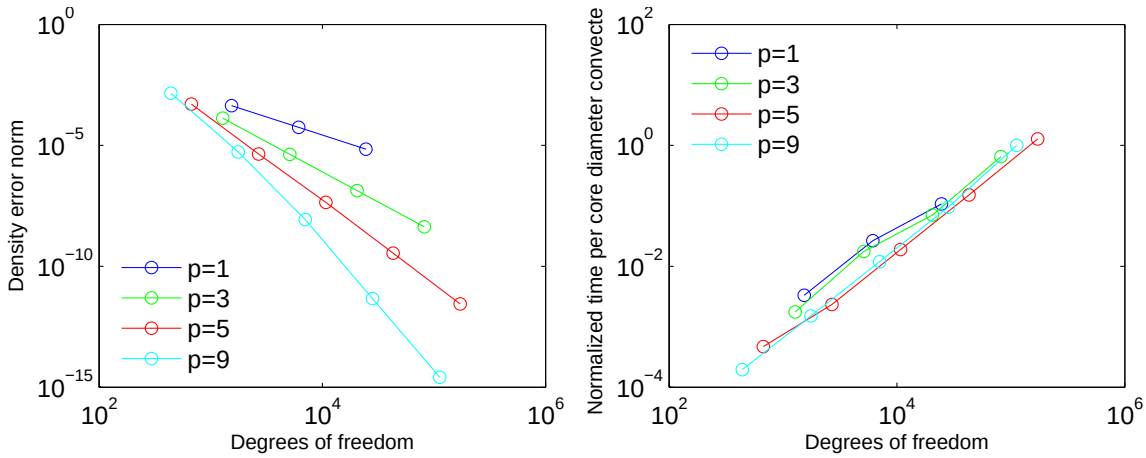

Figure 18: Efficiency of the high order DG scheme in terms of total degrees of freedom for density error norm and wallclock time per core diameter of convection. Timings have been normalized by the lowest error case ($N = 2048$ elements of degree $p = 9$). For a fixed error, increasing degree p permits less DoF and results in a shorter run-time.

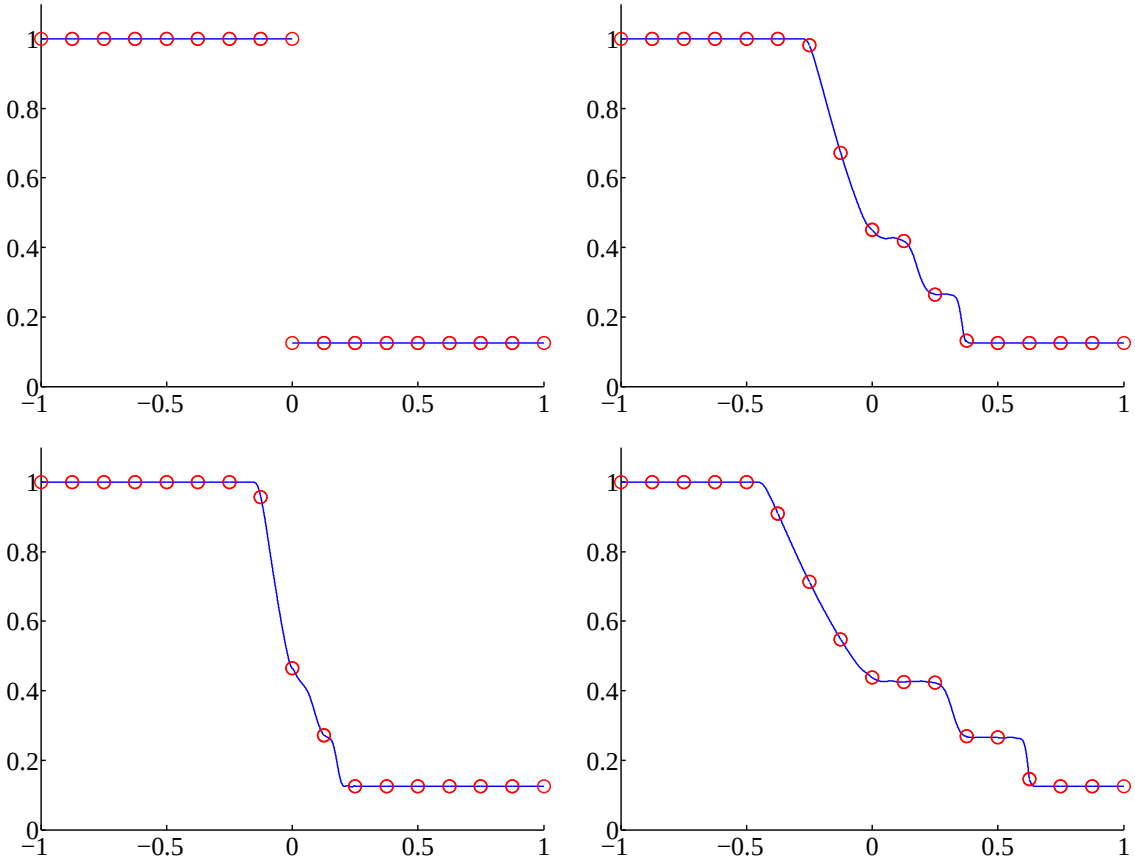

Figure 19: Time evolution of the Sod shock tube (density) on $N = 16$ elements of degree $p = 9$. Markers indicate element boundaries.

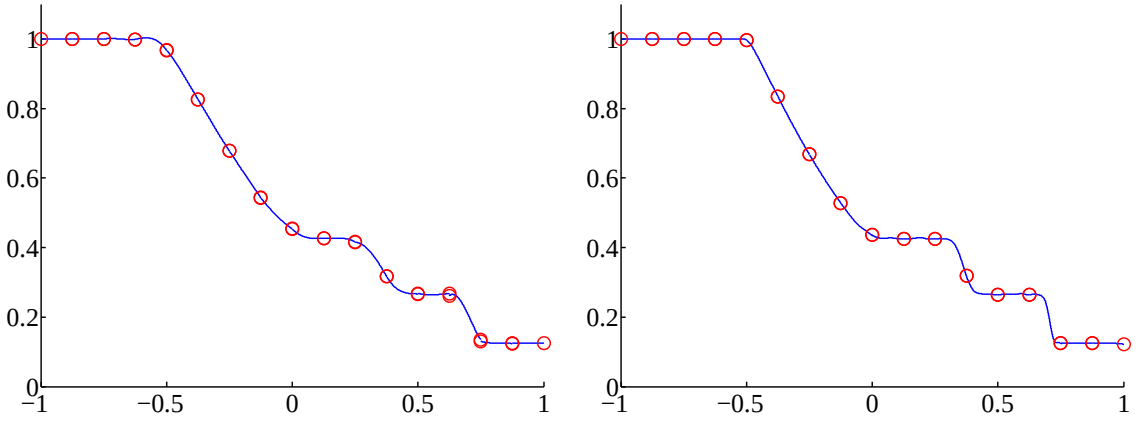

Figure 20: Density for the Sod shock tube at the final time using degree $p = 3$ (left) and $p = 9$ (right). Markers indicate element boundaries. The ability to exploit the high order sub-cell resolution for relatively thin shock profiles is demonstrated by the complete capture of the shock and slip line within the boundaries of a single element.

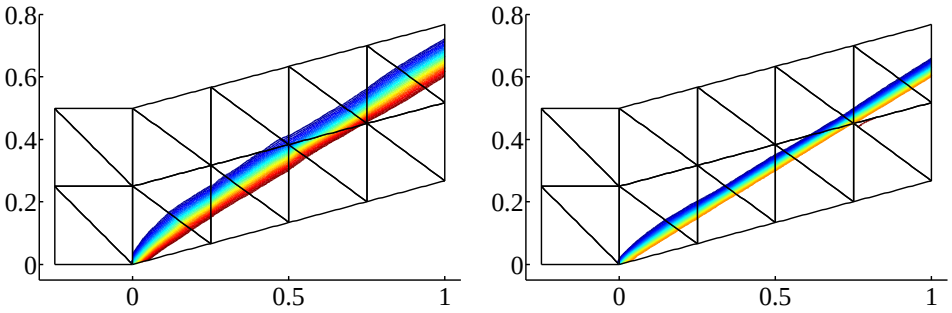

Figure 21: Steady-state pressure contours for the supersonic wedge on $N = 20$ elements of degree $p = 3$ (left) and $p = 9$ (right). The ability to exploit the high order sub-cell resolution for relatively thin shock profiles is even more evident in this 2D example, where the shock is captured in less than one-half of an element width in the degree $p = 3$ case and less than one-quarter of an element width in the degree $p = 9$ case.

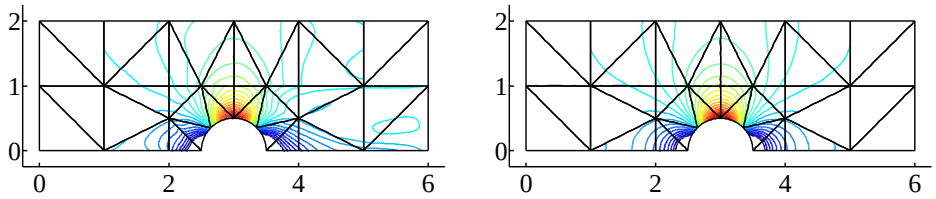

Figure 22: Steady-state x-momentum contours for the subsonic cylinder on $N = 36$ elements of degree $p = 3$ (left) and $p = 7$ (right). The asymmetry in the contours of the lower-order solution indicates the generation of non-physical entropy.

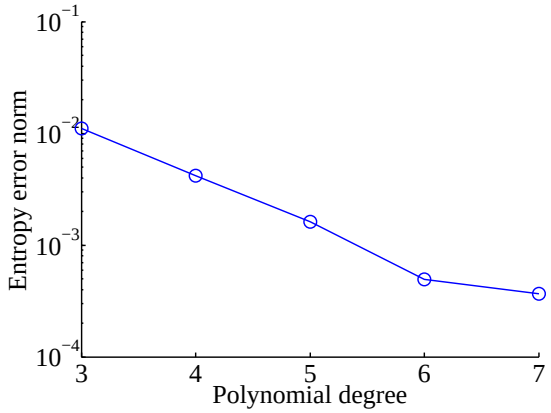

Figure 23: Steady-state entropy error norm convergence for the subsonic cylinder.

CHAPTER III

MULTI-RESOLUTION DISCONTINUOUS GALERKIN METHOD

The following development presents the fundamental tools required for the multi-resolution extension the discontinuous Galerkin method. The discussion begins with the classical framework, subsequently describes algorithms for working with data decomposed over multiple scales, and finally addresses the aspects of the discontinuous Galerkin method that are remarkably well-suited for this framework. Conforming to the guiding principle that it is a method's approach that is most significant, only the simplest possible component techniques are utilized. The method is demonstrated by application to canonical problems for the Euler equations in one spatial dimension, and the path to higher spatial dimensions is outlined.

3.1 Multi-Resolution Framework

Here the relationship between fluctuations and smooth backgrounds is made mathematically precise. Developed by Meyer [60] and Mallat [57], the multi-resolution analysis leads directly to a scale-wise, orthogonal decomposition of a function space. This is achieved by describing functions whose dilates and translates form an orthonormal basis. A modal coordinate transformation is performed on the high resolution reference approximation that retains the same resolution and the same total number degrees of freedom, but characterizes the information contained therein by specific scale contribution. This localization in both spectral and physical space provides the opportunity to adaptively compress the approximation within the error of the reference representation. The following development builds on the broken approximation space inherent to the discontinuous Galerkin method and is a generic spatial dimension extension of Alpert *et al.* [2].

3.1.1 Multi-Resolution Analysis

Begin the multi-resolution analysis by enriching the function space and notation. First, by n times recursive mid-point subdivision, partition the d-dimensional canonical element Ω_c into a collection of 2^{dn} non-overlapping congruent sub-regions Ω_h as

$$\Omega_c = \bigcup_{h=0}^{2^{dn}-1} \Omega_h, \quad \Omega_h \cap \Omega_{h'} = \emptyset \text{ for } h' \neq h \tag{119}$$

Figure 24 shows one and two-dimensional elements. Second, on each sub-region approximate the continuous function space as a vector space $\mathcal{V}_p^n$

$$\begin{aligned} \mathcal{V}_p^n = \{ f \colon & \text{ the restriction of } f \text{ to the sub-domain } \Omega_h \in \Omega_c \\ & \text{for } h = 0, \ldots, 2^{dn} - 1 \\ & \text{is a polynomial of degree less than or equal to } p \\ & \text{and } f \text{ vanishes elsewhere } \} \end{aligned} \tag{120}$$

with

$$\dim \mathcal{V}_p^n = 2^{dn} k(p) \tag{121}$$

The space $\mathcal{V}_p^n$ forms a component of a nested sequence of closed subspaces (i.e., an ascending chain of embedded closed subspaces)

$$\mathcal{V}_p^0 \subset \mathcal{V}_p^1 \subset \cdots \subset \mathcal{V}_p^n \subset \cdots \tag{122}$$

Define a vector space $\mathcal{W}_p^n$ as the orthogonal complement of $\mathcal{V}_p^n$ in $\mathcal{V}_p^{n+1}$

$$\mathcal{W}_p^n = \mathcal{V}_p^{n+1} \ominus \mathcal{V}_p^n \tag{123}$$

By this definition, $\mathcal{W}_p^n$ is the *details space* and $\mathcal{V}_p^n$ is consequently the *averages space*. Since $\dim \mathcal{V}_p^{n+1} = 2^{d(n+1)} k(p)$ and $\dim \mathcal{V}_p^n = 2^{dn} k(p)$, it is clear that

$$\dim \mathcal{W}_p^n = 2^{dn}(2^d - 1) k(p) \tag{124}$$

Any space $\mathcal{V}_p^n$ can then be written as progressively finer details on top of an averages background

$$\mathcal{V}_p^n = \mathcal{V}_p^0 \oplus \mathcal{W}_p^0 \oplus \mathcal{W}_p^1 \oplus \cdots \oplus \mathcal{W}_p^{n-1} \tag{125}$$

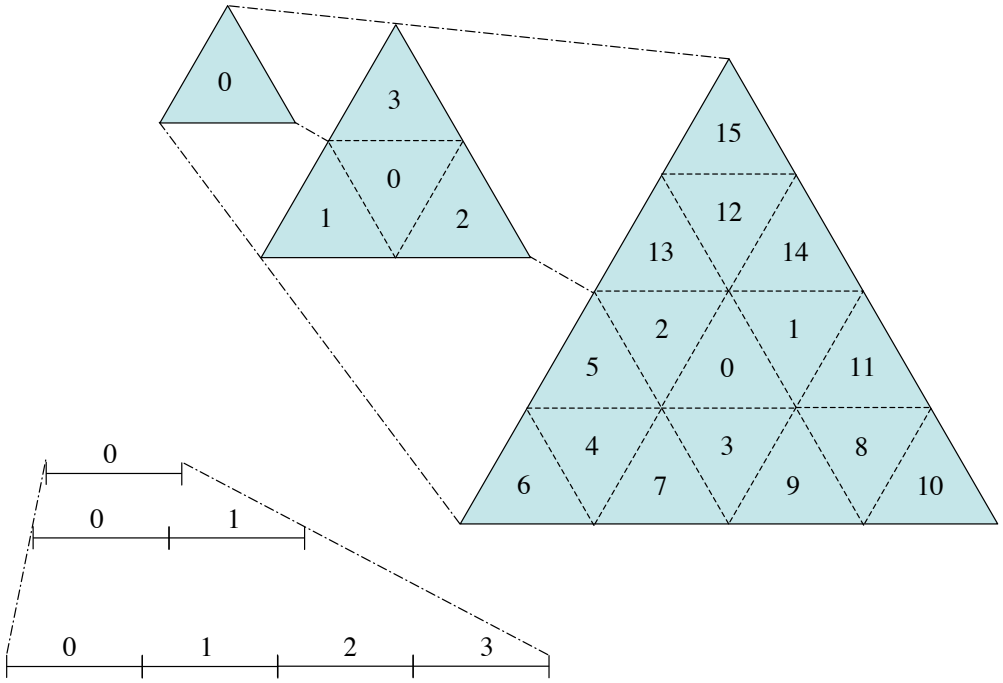

Figure 24: Recursive subdivision for $n = 0, 1, 2$ and corresponding numbering of subregions $h = 0, \ldots, 2^{dn} - 1$ in one and two dimensions.

Given a basis $\phi_0, \ldots, \phi_{k-1}$ for $\mathcal{V}_p^0$ on the d-dimensional region Ω_c having coordinates τ, the space $\mathcal{V}_p^n$ is spanned by $2^{dn}k(p)$ functions obtained from this basis by dilation and translation

$$\phi_j^{nh}(\tau) = c_h \phi_j(\mathcal{T}_{\Omega_c \to \Omega_h} \tau) \tag{126}$$

Here c_h is the dilation factor given by

$$c_h = \sqrt{\frac{|\Omega_c|}{|\Omega_h|}} = 2^{dn/2} \tag{127}$$

and $\mathcal{T}_{\Omega_c \to \Omega_h}$ is the translation operator (or general affine transformation in two or more dimensions) mapping from coordinates relative to the canonical element to its h-th subregion. Similarly, given a basis $\psi_{(l)0}, \ldots, \psi_{(l)k-1}$ for $\mathcal{W}_p^0$ where $l = 1, \ldots, 2^d - 1$, the space $\mathcal{W}_k^n$ is spanned by the $2^{dn}(2^d - 1)k(p)$ functions

$$\psi_{(l)j}^{nh}(\tau) = c_h \psi_{(l)j}(\mathcal{T}_{\Omega_c \to \Omega_h} \tau) \tag{128}$$

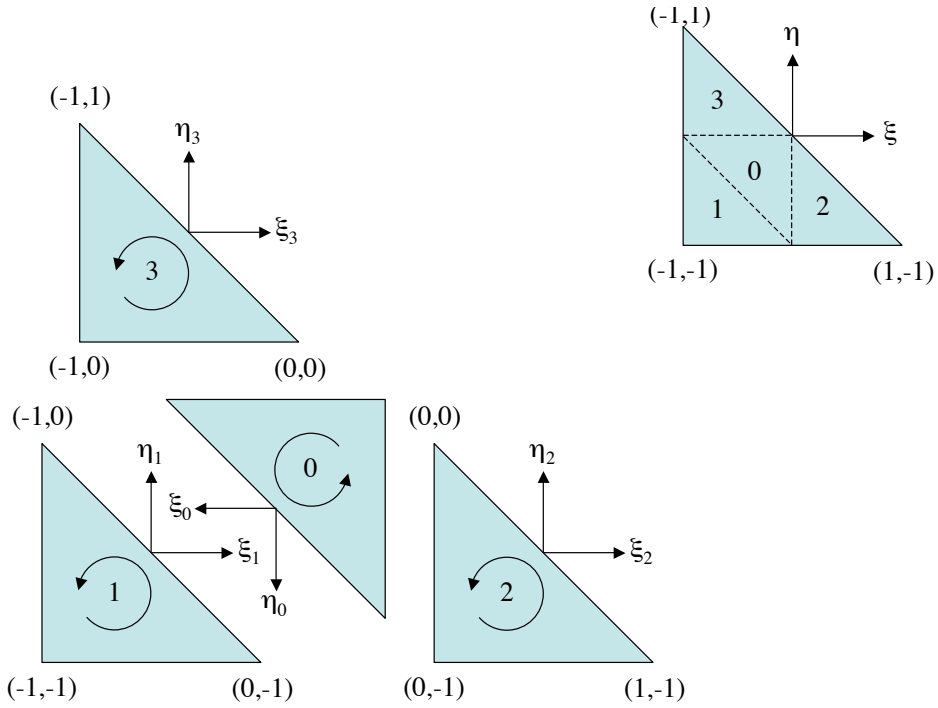

Figure 25: Dilation and translation of the sub-regions on the bi-unit triangle.

On the canonical bi-unit interval, the dilation / translation relation $\mathcal{T}_{\Omega_c \to \Omega_h} \tau$ becomes

$$\begin{aligned} \Omega_0 &: \quad \xi_0 = 2\xi + 1 \\ \Omega_1 &: \quad \xi_1 = 2\xi - 1 \end{aligned} \tag{129}$$

For the bi-unit triangle, Figure 25 shows the dilation / translation relation to be

$$\begin{aligned} \Omega_0 &: \quad \xi_0 = -2\xi - 1, \quad \eta_0 = -2\eta - 1 \\ \Omega_1 &: \quad \xi_1 = 2\xi + 1, \quad \eta_1 = 2\eta + 1 \\ \Omega_2 &: \quad \xi_2 = 2\xi - 1, \quad \eta_2 = 2\eta + 1 \\ \Omega_3 &: \quad \xi_3 = 2\xi + 1, \quad \eta_3 = 2\eta - 1 \end{aligned} \tag{130}$$

In general, the $\phi_0, \ldots, \phi_{k-1}$ are called *multi-scaling* functions and the $\psi_{(l)0}, \ldots, \psi_{(l)k-1}$ are called *multi-wavelet* functions. By construction, the basis functions are orthonormal such that

$$\langle \phi_i, \phi_j \rangle = \delta_{ij}, \quad \langle \psi_{(l)i}, \psi_{(l')j} \rangle = \delta_{ij}\delta_{ll'} \tag{131}$$

from which follows

$$\langle \psi^{nh}_{(l)i}, \psi^{n'h'}_{(l')j} \rangle = \delta_{ij}\delta_{ll'}\delta_{nn'}\delta_{hh'} \tag{132}$$

Furthermore, since $\mathcal{W}_p^0 \perp \mathcal{V}_p^0$

$$\langle \phi_i, \psi_{(l)j} \rangle = 0 \tag{133}$$

The set $\{\phi_j\} \cup \{\psi_{(l)j}^{mh}\}$ with modes $j = 0, \ldots, k-1$, dimensional connections $l = 1, \ldots, 2^d - 1$, scales $m = 0, \ldots, n-1$, and sub-regions $h = 0, \ldots, 2^{dm} - 1$ therefore forms a complete orthonormal basis for $\mathcal{V}_p^n$

3.1.2 Series Approximation

The projection of a function $\tilde{f}(\tau)$ onto the space $\mathcal{V}_p^n$ is

$$\mathbb{P}_k^n \tilde{f}(\tau) = f^n(\tau) = \sum_{h=0}^{2^{dn}-1} \sum_{j=0}^{k-1} \bar{f}_j^{nh} \phi_j^{nh}(\tau) \tag{134}$$

with averages coordinates given by

$$\bar{f}_j^{nh} = \langle \phi_j^{nh}, f^n \rangle \tag{135}$$

Similarly, the projection of a function $\tilde{f}(\tau)$ onto the space $\mathcal{W}_p^n$ is

$$\mathbb{Q}_k^n \tilde{f}(\tau) = \sum_{h=0}^{2^{dn}-1} \sum_{l=1}^{2^d-1} \sum_{j=0}^{k-1} d_{(l)j}^{nh} \psi_{(l)j}^{nh}(\tau) \tag{136}$$

with details coordinates given by

$$d_{(l)j}^{nh} = \langle \psi_{(l)j}^{nh}, f^{n+1} \rangle \tag{137}$$

Since $\mathcal{V}_p^n = \mathcal{V}_p^0 \oplus_{m=0}^{n-1} \mathcal{W}_p^m$, it follows that

$$\mathbb{P}_k^n \tilde{f}(\tau) = \mathbb{P}_k^0 \tilde{f}(\tau) + \sum_{m=0}^{n-1} \mathbb{Q}_k^m \tilde{f}(\tau) \tag{138}$$

Therefore the approximation of the function in terms of a multi-resolution expansion is

$$\mathbb{P}_k^n \tilde{f}(\tau) = \sum_{j=0}^{k-1} \bar{f}_j^{00} \phi_j^{00}(\tau) + \sum_{m=0}^{n-1} \sum_{h=0}^{2^{dm}-1} \sum_{l=1}^{2^d-1} \sum_{j=0}^{k-1} d_{(l)j}^{mh} \psi_{(l)j}^{mh}(\tau) \tag{139}$$

Denote the sets of averages and details at a given scale m as

$$\bar{f}^m = \{\bar{f}_j^{mh}\}, \quad d^m = \{d_{(l)j}^{mh}\} \tag{140}$$

where the indices cycle first by $j = 0, \ldots, k-1$, then by $l = 1, \ldots, 2^d - 1$, and finally by $h = 0, \ldots, 2^{dm} - 1$. The multi-resolution form [37] of f is

$$\mu^n(f) = \left\{ \bar{f}^0, d^0, \ldots, d^{n-1} \right\} \tag{141}$$

The crucial idea with decomposing the representation across multiple scales is that wherever $\tilde{f}$ is sufficiently smooth at some scale m', the corresponding details coefficients for scale $m > m'$ are relatively small and may be neglected, thereby providing a significant savings in the total number of terms required to represent the approximation.

3.1.3 Global Relative Error Thresholding

The question now is what is meant by relatively small details? One choice is to bound the error between the approximations at two successive resolutions as

$$\|f^{m+1} - f^m\| \leq \varepsilon \|f^{m+1}\| \tag{142}$$

For the right hand side term

$$\begin{aligned}
\langle f^m, f^m \rangle &= \int_{\Omega_c} \sum_h \sum_j \bar{f}_j^{mh} \phi_j^{mh}(\tau) \sum_{h'} \sum_{j'} \bar{f}_{j'}^{mh'} \phi_{j'}^{mh'}(\tau) \, \mathrm{d}\tau \\
&= \sum_h \sum_j \sum_{h'} \sum_{j'} \left(\int_{\Omega_c} \phi_j^{mh}(\tau) \phi_j^{mh'}(\tau) \, \mathrm{d}\tau \right) \bar{f}_j^{mh} \bar{f}_{j'}^{mh'} \\
&= \sum_h \sum_j \left(\bar{f}_j^{mh} \right)^2
\end{aligned}$$

Therefore

$$\|f^{m+1}(\tau)\| = |\bar{f}^{m+1}| \tag{143}$$

For the left hand side, since the detail coefficients and multi-wavelet functions determine the difference

$$\Delta^m(\tau) = f^{m+1}(\tau) - f^m(\tau) = \sum_h \sum_l \sum_j d_{(l)j}^{mh} \psi_{(l)j}^{mh}(\tau) \tag{144}$$

then

$$\begin{aligned}
\langle \Delta^m, \Delta^m \rangle &= \int_{\Omega_c} \sum_h \sum_l \sum_j d_{(l)j}^{mh} \psi_{(l)j}^{mh}(\tau) \sum_{h'} \sum_{l'} \sum_{j'} d_{(l')j'}^{mh'} \psi_{(l')j'}^{mh'}(\tau) \, \mathrm{d}\tau \\
&= \sum_h \sum_l \sum_j \sum_{h'} \sum_{l'} \sum_{j'} \left(\int_{\Omega_c} \psi_{(l)j}^{mh}(\tau) \psi_{(l')j}^{mh'}(\tau) \, \mathrm{d}\tau \right) d_{(l)j}^{mh} d_{(l')j'}^{mh'} \\
&= \sum_h \sum_l \sum_j \left(d_{(l)j}^{mh} \right)^2
\end{aligned}$$

Therefore

$$\|f^{m+1}(\tau) - f^m(\tau)\| = |d^m| \tag{145}$$

The two-scale relative error criteria is then written in terms of the modal coordinates as

$$|d^m| \leq \varepsilon |\bar{f}^{m+1}| \tag{146}$$

If for each h-region only details satisfying $2^{dn}|d^{nh}|^2 \leq |d^n|^2$ are considered for truncation, then

$$|d^{nh}| \leq 2^{-dn/2}\varepsilon |\bar{f}^{n+1}| \tag{147}$$

By setting to zero all details coefficients that satisfy this constraint, the multi-resolution form is adaptively compressed relative to the specified tolerance. Since the resolution on a maximum n levels with best order-of-accuary $(p + 1/2)$ can expected to be $2^{-n(p+1/2)}$, the value for the tolerance should be no smaller than this limit. From experience, the strategy that has performed reliably in this work is to deflate the expected the order of accuracy, retaining details and their nearest sub-region neighbors according to $\varepsilon \sim \mathcal{O}(2^{-n(p-1/2)})$. The effect is to provide aggressive truncation of details while maintaining a buffer region that is based entirely upon the local solution data.

3.2 Scale Transition Algorithms

By analogy to high and low-pass filtering in signal processing, the multi-resolution transform of a function can be achieved using filter banks. The two-scale transition mechanism hinges upon these filter banks to relate the basis functions at one scale in terms of the next finer scale. Multi-resolution encoding / decoding algorithms are ultimately constructed for both modal coordinates and associated matrix operators.

3.2.1 Quadrature Mirror Filter Banks

It has been established that $\phi_j \in \mathcal{V}_k^0 \subset \mathcal{V}_k^1$. Suppressing for the moment the explicit notation of scale m, this implies the ϕ_j may be written in terms of the ϕ_j^h from the sub-regions of the next finer scale as

$$\phi_i(\tau) = \sum_{h=0}^{2^d-1} \sum_{j=0}^{k-1} H_{ij}^h \phi_j^h(\tau) \tag{148}$$

The matrices of expansion coefficients H^h serve as a low-pass filter and are sometimes called the decimation matrix, in reference to dyadic averaging of pointwise data. Similarly, $\psi_{(l)j} \in \mathcal{W}_k^0 \subset \mathcal{V}_k^1$ such that

$$\psi_{(l)i}(\tau) = \sum_{h=0}^{2^d-1} \sum_{j=0}^{k-1} G^h_{(l)ij} \phi^h_j(\tau) \tag{149}$$

where the matrices of expansion coefficients $G^h_{(l)}$ serve as a high-pass filter. These two relations are collectively known as the two-scale difference equations and the matrices are the quadrature mirror filter (QMF) banks. Often, these filters are constructed to *generate* the basis functions subject to constraints on orthogonality, support, regularity, *etc.* [24] either by direct iteration on the two-scale equations or by a Fourier transform having an explicit formula involving the expansion coefficients. However, the present work takes the opposite approach, selecting scaling functions on the canonical element and explicitly constructing appropriate multi-wavelet functions for the detail space basis [3, 4]. In this case, the QMF are actually *defined* by the scaling and multi-wavelet functions.

Taking the two-scale difference equations, form the inner product with the averages basis on the sub-regions of the next finer scale and use orthogonality and mutilation to obtain

$$\langle \phi_i, \phi^{h'}_{j'} \rangle = \sum_h \sum_j H^h_{ij} \langle \phi^h_j, \phi^{h'}_{j'} \rangle = \sum_h \sum_j H^h_{ij} \delta_{jj'} \delta_{hh'}$$

$$\langle \psi_{(l)i}, \phi^{h'}_{j'} \rangle = \sum_h \sum_j G^h_{(l)ij} \langle \phi^h_j, \phi^{h'}_{j'} \rangle = \sum_h \sum_j G^h_{(l)ij} \delta_{jj'} \delta_{hh'}$$

The QMF matrices are then given by

$$H^h_{ij} = \langle \phi_i, \phi^h_j \rangle = 2^{-dn/2} \langle \phi_i(\mathcal{T}_h^{-1}\tau), \phi_j(\tau) \rangle \tag{150}$$

$$G^h_{(l)ij} = \langle \psi_{(l)i}, \phi^h_j \rangle = 2^{-dn/2} \langle \psi_{(l)i}(\mathcal{T}_h^{-1}\tau), \phi_j(\tau) \rangle \tag{151}$$

To establish useful inter-relationships between H^h and $G^h_{(l)}$, again take inner products of the two-scale difference equations, this time with the averages and details basis at the same

scale, and use orthogonality and mutilation to find

$$\langle \phi_i, \phi_{i'} \rangle = \sum_h \sum_j \sum_{h'} \sum_{j'} H^h_{ij} H^{h'}_{i'j'} \langle \phi^h_j, \phi^{h'}_{j'} \rangle$$

$$\langle \psi_{(l)i}, \psi_{(l')i'} \rangle = \sum_h \sum_j \sum_{h'} \sum_{j'} G^h_{(l)ij} G^{h'}_{(l')i'j'} \langle \phi^h_j, \phi^{h'}_{j'} \rangle$$

$$\langle \psi_{(l)i}, \phi_{i'} \rangle = \sum_h \sum_j \sum_{h'} \sum_{j'} G^h_{(l)ij} H^{h'}_{i'j'} \langle \phi^h_j, \phi^{h'}_{j'} \rangle$$

Therefore

$$\delta_{ii'} = \sum_h \sum_j H^h_{ij} H^h_{i'j}, \quad \delta_{ii'} = \sum_h \sum_j G^h_{(l)ij} G^h_{(l)i'j}, \quad 0 = \sum_h \sum_j G^h_{(l)ij} H^h_{i'j}$$

or simply

$$\sum_h H^h (H^h)^T = I, \quad \sum_h G^h_{(l)} (G^h_{(l)})^T = I, \quad \sum_h G^h_{(l)} (H^h)^T = 0 \tag{152}$$

Before continuing, it is convenient to introduce notation that will facilitate working with the multi-resolution form of vectors and matrices organized by specific resolution level. Recalling that that the averages and details vectors cycle first by $j = 0, \ldots, k-1$, then by $l = 1, \ldots, 2^d - 1$, and finally by $h = 0, \ldots, 2^d - 1$, the QMF matrices are grouped as

$$H = \begin{bmatrix} H^0 & H^1 & \cdots & H^{2d-1} \end{bmatrix} \tag{153}$$

and

$$G = \begin{bmatrix} G^0_{(1)} & G^1_{(1)} & \cdots & G^{2d-1}_{(1)} \\ G^0_{(2)} & G^1_{(2)} & \cdots & G^{2d-1}_{(2)} \\ \vdots & \vdots & \ddots & \vdots \\ G^0_{(2d-1)} & G^1_{(2d-1)} & \cdots & G^{2d-1}_{(2d-1)} \end{bmatrix} \tag{154}$$

The orthogonality relations become

$$H H^T = G G^T = I \tag{155}$$

$$H G^T = G H^T = 0 \tag{156}$$

By defining the matrix

$$Q = \begin{bmatrix} H \\ G \end{bmatrix} \tag{157}$$

and noting that by the previous results $QQ^T = I$, it is clear that Q is an orthogonal matrix satisfying $Q^TQ = I$. This last condition provides the additional relation

$$H^TH + G^TG = I \tag{158}$$

3.2.2 Modal Coordinates Vector Encoding

By the developments so far, given the averages at scale $m+1$, the averages at the next lower resolution are given by

$$\bar{f}^m = H\bar{f}^{m+1} \tag{159}$$

where H is the $2^{dm}k \times 2^{d(m+1)}k$ repeated block diagonal analog of the low pass filter above. While it is possible to use the two-scale relations to write down the details from the averages at next higher scale as well, it is more instructive to follow Harten's presentation [40]. Given the averages at scale m, the predictions at the next higher resolution are given by

$$\bar{\bar{f}}^{m+1} = R\bar{f}^m \tag{160}$$

where the yet-to-be defined reconstruction matrix R is $2^{d(m+1)} \times 2^{dm}k$. Define the error between the averages and the predictions as

$$e^{m+1} = \bar{f}^{m+1} - \bar{\bar{f}}^{m+1} \tag{161}$$

and note that

$$e^{m+1} = \bar{f}^{m+1} - R\bar{f}^m = \bar{f}^{m+1} - RH\bar{f}^{m+1} = (I - RH)\bar{f}^{m+1} \tag{162}$$

By requiring the decimation of the error to vanish, it follows that

$$\begin{aligned} He^{m+1} = 0 \quad &\longrightarrow \quad (H - HRH)\bar{f}^{m+1} = 0 \quad \longrightarrow \quad HR = I \\ H\bar{\bar{f}}^{m+1} = H\bar{f}^{m+1} = \bar{f}^m \quad &\longrightarrow \quad HR\bar{f}^m = \bar{f}^m \quad \longrightarrow \quad HR = I \end{aligned} \tag{163}$$

Given the orthogonality conditions above, $R = H^{\mathrm{T}}$ is one choice that will satisfy this requirement. Manipulating the error as $e^{m+1} = Ie^{m+1}$ with $H^{\mathrm{T}}H + G^{\mathrm{T}}G = I$, the error is

$$e^{m+1} = G^{\mathrm{T}}d^m \tag{164}$$

with the details defined as

$$d^m = Ge^{m+1} = G(I - RH)\bar{f}^{m+1} = G\bar{f}^{m+1} \tag{165}$$

The tools necessary to encode (compress) and decode (reconstruct) the the averages from the adjacent resolution are now in place. Given $\bar{f}^n$, encoding is the recursion for $m = n-1, \ldots, 0$

$$\begin{aligned} d^m &= G\bar{f}^{m+1} \\ \bar{f}^m &= H\bar{f}^{m+1} \end{aligned} \tag{166}$$

Conversely, given $\mu^n(f)$, decoding is the recursion for $m = 0, \ldots, n-1$

$$\bar{f}^{m+1} = H^{\mathrm{T}}\bar{f}^m + G^{\mathrm{T}}d^m \tag{167}$$

3.2.3 Operator Matrix Encoding – Non-Standard Form

By considering separately the rows and columns of a matrix A, the two-scale relations for A are derived by analogy to the vector f. Given the column vector forms of decimation and prediction above, the corresponding row vector forms are trivially

$$\begin{aligned} \bar{f}^m = H\bar{f}^{m+1} \quad &\longrightarrow \quad (\bar{f}^m)^{\mathrm{T}} = (\bar{f}^{m+1})^{\mathrm{T}}H^{\mathrm{T}} \\ \bar{\bar{f}}^{m+1} = R\bar{f}^m \quad &\longrightarrow \quad (\bar{\bar{f}}^{m+1})^{\mathrm{T}} = (\bar{\bar{f}}^{m+1})^{\mathrm{T}}R^{\mathrm{T}} \end{aligned} \tag{168}$$

Since a matrix may be written as the outer product of two vectors $A = uv^{\mathrm{T}}$, the appropriate operations are

$$\bar{A}^m = H\bar{A}^{m+1}H^{\mathrm{T}} \tag{169}$$

$$\bar{\bar{A}}^{m+1} = R\bar{A}^m R^{\mathrm{T}} \tag{170}$$

Define the error between the averages and the prediction as

$$E^{m+1} = \bar{A}^{m+1} - \bar{\bar{A}}^{m+1} \tag{171}$$

and again require that the decimation of the error vanishes

$$HE^{m+1}H^{\mathrm{T}} = 0 \tag{172}$$

Manipulating the error as $E^{m+1} = IE^{m+1}I^{\mathrm{T}}$ with $H^{\mathrm{T}}H + G^{\mathrm{T}}G = I$, associated details are found as

$$E^{m+1} = G^{\mathrm{T}}D^m_{(1)}G + G^{\mathrm{T}}D^m_{(2)}H + H^{\mathrm{T}}D^m_{(3)}G \tag{173}$$

where there are now the three distinct scale interactions

$$\begin{aligned} D^m_{(1)} &= GE^{m+1}G^{\mathrm{T}} = G(\bar{A}^{m+1} - R\bar{A}^{m+1}R^{\mathrm{T}})G^{\mathrm{T}} = G\bar{A}^{m+1}G^{\mathrm{T}} \\ D^m_{(2)} &= GE^{m+1}H^{\mathrm{T}} = G(\bar{A}^{m+1} - R\bar{A}^{m+1}R^{\mathrm{T}})H^{\mathrm{T}} = G\bar{A}^{m+1}H^{\mathrm{T}} \\ D^m_{(3)} &= HE^{m+1}G^{\mathrm{T}} = H(\bar{A}^{m+1} - R\bar{A}^{m+1}R^{\mathrm{T}})G^{\mathrm{T}} = H\bar{A}^{m+1}G^{\mathrm{T}} \end{aligned} \tag{174}$$

Thus the multi-resolution form of A (non-standard) [15, 40] is

$$\mu^n_{NS}(A) = \left\{\bar{A}^0, D^0_{(1)}, D^0_{(2)}, D^0_{(3)}, \ldots, D^{n-1}_{(1)}, D^{n-1}_{(2)}, D^{n-1}_{(3)}\right\} \tag{175}$$

As before, in place are the tools necessary to encode (compress) and decode (reconstruct) the the averages from the adjacent resolution. Given $\bar{T}^n$, encoding is the recursion for $m = n-1, \ldots, 0$

$$\begin{aligned} D^m_{(1)} &= G\bar{T}^{m+1}G^{\mathrm{T}} \\ D^m_{(2)} &= G\bar{T}^{m+1}H^{\mathrm{T}} \\ D^m_{(3)} &= H\bar{T}^{m+1}G^{\mathrm{T}} \\ \bar{A}^m &= H\bar{T}^{m+1}H^{\mathrm{T}} \end{aligned} \tag{176}$$

Conversely, given $\mu^n_{NS}(A)$, decoding is the recursion for $m = 0, \ldots, n-1$

$$\bar{A}^{m+1} = H^{\mathrm{T}}\bar{A}^m + G^{\mathrm{T}}\left(D^m_{(1)}G + D^m_{(2)}H\right) + H^{\mathrm{T}}D^m_{(3)}G \tag{177}$$

3.2.4 Beylkin Algorithm

The Beylkin algorithm provides a recursive procedure for applying an operator in non-standard form to a vector [17, 18]. Given $\mu^n_{NS}(A), \mu^n(f)$, compute for $m = 0, \ldots, n-1$

$$\begin{aligned} \hat{d}^m &= D_{(1)}d^m + D_{(2)}\bar{f}^m \\ \hat{g}^m &= D_{(3)}d^m \\ \bar{f}^{m+1} &= H^{\mathrm{T}}\bar{f}^m + G^{\mathrm{T}}d^m \end{aligned} \tag{178}$$

At this point, the representation of g is not in any basis as it consists of both averages and details on *all* scales

$$\mathbb{P}_k^n(Af)(\tau) = \sum_{m=0}^{n-1}\sum_{h=0}^{2^{dm}-1}\sum_{j=0}^{k-1}\hat{g}_j^{mh}\phi_j^{mh}(\tau) + \sum_{m=0}^{n-1}\sum_{h=0}^{2^{dm}-1}\sum_{l=1}^{2^d-1}\sum_{j=0}^{k-1}\hat{d}_{(l)j}^{mh}\psi_{(l)j}^{mh}(\tau)$$

However, this does present an opportunity for truncating small values in the expansion. To project the result back into the wavelet basis, take $\bar{g}^{n-1} = \hat{g}^{n-1}$ and compute for $m = n-2, \ldots, 0$

$$\begin{aligned} d^m &= \hat{d}^m + G\bar{g}^{m+1} \\ \bar{g}^m &= \hat{g}^m + H\bar{g}^{m+1} \end{aligned} \tag{179}$$

Now

$$\mathbb{P}_k^n(Af)(\tau) = \sum_{j=0}^{k-1}\bar{g}_j^{00}\phi_j^{00}(\tau) + \sum_{m=0}^{n-1}\sum_{h=0}^{2^{dm}-1}\sum_{l=1}^{2^d-1}\sum_{j=0}^{k-1}d_{(l)j}^{mh}\psi_{(l)j}^{mh}(\tau) \tag{180}$$

as desired.

One difficulty with using the non-standard form and Beylkin algorithm is the fact that non-sparse $\bar{f}^m$ are needed at all levels. For reference scheme operators such as boundary extraction and integration in which a single h block of input data affects a single block of output data, only the *relevant* h portion of $\bar{f}^m$ on any given level need be retained. However for reference scheme operators such as the derivative, multiple sub-regions must communicate, and the logic to determine which h on a given level to retain is complicated due to the additional consideration for the stencil on that level.

3.2.5 Operator Matrix Encoding – Standard Form

A matrix A may also be encoded by simply retaining the *cumulative* operators formed by the process for vector reconstruction, $\mathcal{R}$, and vector compression, $\mathcal{C} = \mathcal{R}^{-1} = \mathcal{R}^{\mathrm{T}}$

$$\bar{g}^n = \bar{A}^n\bar{f}^n \quad \longrightarrow \quad \mathcal{R}\mu^n(g) = \bar{A}^n\mathcal{R}\mu^n(f) \quad \longrightarrow \quad \mu^n(g) = \mu_S^n(A)\mu^n(f) \tag{181}$$

Thus the multi-resolution form of A (standard) is written

$$\mu_S^n(A) = \mathcal{C}\bar{A}^n\mathcal{R} \tag{182}$$

Unfortunately, the standard form of an operator is known to be less sparse than the non-standard form. Nevertheless, this work utilizes the standard form of operators for simplicity of implementation.

3.3 Discontinuous Galerkin with Multi-Resolution

A key to the success and convenience of the discontinuous Galerkin method is the use of broken approximation spaces to provide both high order and conservation with an invariably compact stencil. The method often employs a member of the Jacobi family of polynomials for element basis functions, such as Legendre polynomials on the bi-unit interval and Koornwinder-Dubiner polynomials on the bi-unit triangle. Following from the weak form of the derivative in a discontinuous setting, inter-element communication of flow information is maintained by a numerical flux function in the boundary trace inner product. The resulting method enjoys high accuracy per degree of freedom while retaining geometric versatility.

Given these attributes and the ease in which the broken approximation space is extended by a multi-resolution analysis, the discontinuous Galerkin method is embraced as a promising candidate for data compression afforded by multi-resolution approximation. Some final topics are addressed here to extend the method. First, the filter banks required for scale transition depend entirely on the selection of the bases for the averages and details approximation spaces. Given the precedent set in the original method, the Jacobi polynomial is retained as the choice of basis for the canonical element, thereby establishing the scaling functions on the coarsest scale. The corresponding multi-wavelet functions for the detail space basis are constructed following the procedure due to Alpert [3, 4], yielding what might be viewed as a multi-modal analog of the famous Haar wavelet. Second, the weak form of the derivative and associated boundary trace inner product is examined from the refined perspective of intra-element communication between the sub-regions. Both the use of generalized coordinates and the Lax-Friedreichs flux function facilitate construction of a *linear* reference scheme operator for the derivative of functions on the canonical element. This and other reference scheme matrix operators (e.g. the boundary extraction and integration operators) may be encoded in the multi-resolution form using the algorithms above.

3.3.1 Alpert's Procedure for Detail Space Basis Functions

The following is Alpert's procedure for constructing the one-dimensional basis $\{\psi_j\}$ for $j = 0, \ldots, k-1$ of the approximating space $\mathcal{W}_k^0$ as it appears in references [3, 4]. Start with

the $2k$ functions which span the space of functions that are polynomials of degree less than k on the interval $(0,1)$ and on $(-1,0)$, then orthogonalize k of them, first to the functions $\phi_0, \phi_1, \ldots, \phi_{k-1}$, then to the functions $\phi_k, \phi_{k+1}, \ldots, \phi_{2k-1}$, and finally among themselves.

1. Define
$$w_j^1(x) = \begin{cases} \phi_j(2x-1), & x \in (0,1) \\ -\phi_j(2x+1), & x \in (-1,0) \\ 0, & \text{else} \end{cases}$$
and note that the $2k$ functions $\phi_0, \phi_1, \ldots, \phi_{k-1}, w_0^1, w_2^1, \ldots, w_{k-1}^1$ are linearly independent, hence span the space of functions that are polynomials of degree lees than k on $(0,1)$ and on $(-1,0)$.

2. By the Gram-Schmidt process orthogonalize w_j^1 with respect to the sequence $\phi_0, \phi_1, \ldots, \phi_{k-1}$, to obtain w_j^2, for $j = 0, \ldots, k-1$. This orthogonality is preserved by the remaining orthogonalizations, which only produce linear combinations of the w_j^2.

3. The next sequence of steps yields $k-1$ functions orthogonal to the sequence $\phi_0, \phi_1, \ldots, \phi_{k-1}$, of which $k-2$ functions are orthogonal to ϕ_{k+1}, and so forth, down to 1 function which is orthogonal to ϕ_{2k-2}.

   (a) First, if at least one of the w_j^2 is not orthogonal to ϕ_k, reorder the functions so that it appears first, $\langle \phi_k, w_0^2 \rangle \neq 0$

   (b) Define $w_j^3 = w_j^2 - a_j w_0^2$ where a_j is chosen so $\langle \phi_k, w_j^3 \rangle = 0$ for $j = 1, \ldots, k-1$, achieving the desired orthogonality to ϕ_k.

   (c) Similarly, orthogonalize to $\phi_{k+1}, \ldots, \phi_{2k-2}$, each in turn, to obtain $w_0^2, w_1^3, \ldots, w_{k-1}^{k+1}$ such that $\langle \phi_i, w_j^{j+2} \rangle = 0$ for $i \leq j + k - 1$.

4. Finally, do Gram-Schmidt orthogonalization on $w_{k-1}^{k+1}, w_{k-2}^k, \ldots, w_0^2$, in that order, and normalize to obtain $\psi_{k-1}, \psi_{k-2}, \ldots, \psi_0$.

As an example, Figure 26 shows the one-dimensional scaling and multi-wavelet functions for degree $p = 4$.

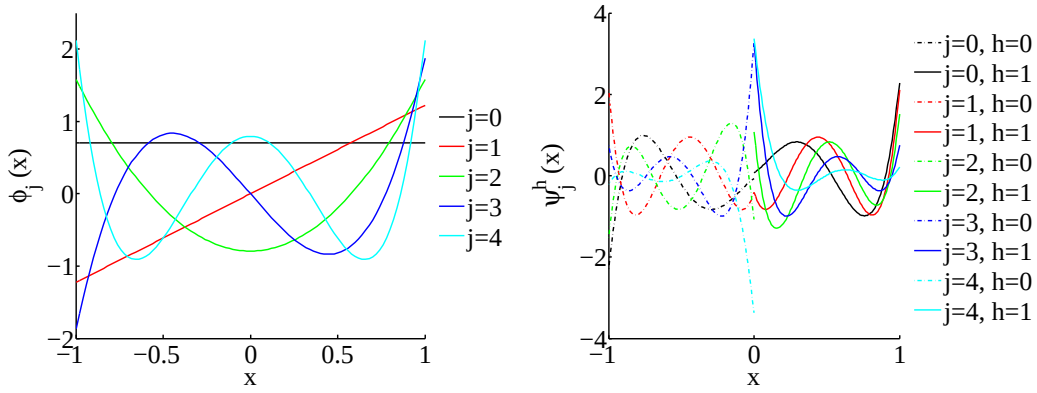

Figure 26: Orthonormal scaling functions $\phi_j(x)$ and multi-wavelet functions $\psi_j^h(x)$ of degree $p = 4$ on the interval.

The above approach may be generalized to d dimensions for constructing a basis of $\psi_{(l)0}, \psi_{(l)1}, \ldots, \psi_{(1)k-1}$ for $l = 1, \ldots, 2^d - 1$. In fact, Yu *et al.* [83] present an algorithm for constructing Alpert multi-wavelets on a triangle by working in barycentric coordinates to effortlessly describe mid-point subdivision of the canonical element. Any suitable symbolic computation engine may be employed to implement this procedure. However, this is not strictly necessary for two reasons. First, the multi-wavelet functions are *only* used for the computation of the high pass filter matrices $G^h_{(l)}$. Second, since the scaling functions is most conveniently provided from sampled values of the Jacobi polynomial family by recursion formula, numerical quadrature is the most natural means of computing the low pass filter matrices H^h. These factors motivate a purely numerical approach to compute G. This is accomplished by working in the modal coordinates of the $w_0, w_1, \ldots, w_{k-1}$ (each in the basis $\phi_0^h, \phi_1^h, \ldots, \phi_{k-1}^h$ for $h = 0, \ldots, 2^{dn} - 1$) instead of the functions themselves. Proper organization these modal coordinates yields G.

3.3.2 Revisiting the Derivative Operator

First it is useful to note that the transformation from modal to physical space is analogous to the single resolution case. Assuming that only the non-trivial case for $\tau_p \in \Omega_h$ is of

interest, the dilation and translation relation becomes

$$\begin{aligned} V_{pj}^{nh} &= \phi_j^{nh}(\tau_p) \\ &= 2^{dn/2}\phi_j(\mathcal{T}_{\Omega_h \to \Omega_c}\tau_p) \\ &= 2^{dn/2}\phi_j(\tau_{cp}) \\ &= 2^{dn/2}V_{pj} \end{aligned} \tag{183}$$

The construction of the derivative operator is demonstrated, focusing on the one-dimensional case for clarity. Let $q(x) = \mathrm{d}f/\mathrm{d}x$, then by orthogonality of the basis $\bar{q}_j^{mh} = \langle \phi_j^{mh}, q \rangle$. In complete analogy to the global domain partition, integrate across the sub-regions of the canonical element by parts twice and treat the normal trace $f_n = n_x f$ with special care to obtain

$$\bar{q}_i^{nh} = \left\langle \phi_i^{nh}, \frac{\mathrm{d}f}{\mathrm{d}x} \right\rangle_{\Omega_h} + \langle \phi, f_n^* - f_n \rangle_{\Gamma_h} \tag{184}$$

Again, the derivative $\mathrm{d}f^{nh}/\mathrm{d}x$ may be computed in two ways. First

$$f_x^{nh}(x) = \frac{\mathrm{d}}{\mathrm{d}x} f^{nh}(x) = \sum_{j=0}^{k-1} \bar{f}_j^{nh} \frac{\mathrm{d}}{\mathrm{d}x}\phi_j^{nh}(x) \quad \longrightarrow \quad \vec{f}_x^{nh} = V_x^{nh}\bar{f}^{nh} \tag{185}$$

where the derivative Vandermonde matrix now includes an additional scale factor relative to the single resolution version

$$\begin{aligned} V_{x_{pj}}^{nh} &= \frac{\mathrm{d}}{\mathrm{d}x}\phi_j^{nh}(x_p) \\ &= \frac{\mathrm{d}}{\mathrm{d}x}\left(2^{n/2}\phi_j(2^n x_p - h)\right) \\ &= 2^{3n/2}\frac{\mathrm{d}}{\mathrm{d}x}\phi_j(x_p) \\ &= 2^{3n/2}V_{x_{pj}} \end{aligned} \tag{186}$$

Writing down the expansion for $\mathrm{d}\tilde{f}/\mathrm{d}x$ directly gives

$$\mathbb{P}_k^n \left.\frac{\mathrm{d}}{\mathrm{d}x}\tilde{f}(x)\right|_h = f_x^{nh}(x) = \sum_{j=0}^{k-1} \bar{f}_{x_j}^{nh}\phi_j^{nh}(x) \quad \longrightarrow \quad \vec{f}_x^{nh} = V^{nh}\bar{f}_x^{nh} \tag{187}$$

The unknown modal coefficients $\bar{f}_x^{nh}$ are found by equating the respective $\vec{f}_x^{nh}$ from the two approaches

$$\bar{f}_x^{nh} = D_x^{nh}\bar{f}^{nh} \tag{188}$$

where the derivative operator is

$$D_x^{nh} = V^{nh^{-1}} V_x^{nh} = 2^n D_x \tag{189}$$

Thus for the orthonormal basis

$$\left\langle \phi_i^{nh}, \frac{\mathrm{d}f^{nh}}{\mathrm{d}x} \right\rangle_{\Omega_h} = \mathbf{e}_{(i)}^T D_x^{nh} \bar{f}^{nh} \tag{190}$$

As shown previously, the boundary term requires special treatment with a numerical flux function that provides the region-to-region communication. This time, the sub-regions Ω_h are the focus, and the current development is inspired by that in [2], but with the addition of the state jump required for the upwind correction. The boundary inner product is expanded into the individual side contributions as

$$\begin{aligned} \left\langle \phi_i^{nh}, f_n^* - f_n \right\rangle_{\Gamma_h} &= 2^{n/2} \left[f_n^*(x_{(+)}) - f_n(x_{(+)}) \right] \phi_i(+1) \\ &\quad + 2^{n/2} \left[f_n^*(x_{(-)}) - f_n(x_{(-)}) \right] \phi_i(-1) \end{aligned} \tag{191}$$

where

$$\begin{aligned} f_n(x_{(+)}) &= 2^{n/2} \sum_j \bar{f}_j^{nh} \phi_j(+1) \\ f_n(x_{(-)}) &= -2^{n/2} \sum_j \bar{f}_j^{nh} \phi_j(-1) \end{aligned} \tag{192}$$

For the convective flux use the Lax-Friedrichs function such that

$$\begin{aligned} f_n^*(x_{(+)}) &= 2^{n/2} \sum_j \frac{1}{2} \left(\bar{f}_j^{nh} \phi_j(+1) + \bar{f}_j^{n,h+1} \phi_j(-1) \right) \\ &\quad + 2^{n/2} \sum_j \frac{\lambda_{\max}}{2} \left(\bar{u}_j^{nh} \phi_j(+1) + \bar{u}_j^{n,h+1} \phi_j(-1) \right) \end{aligned} \tag{193}$$

and

$$\begin{aligned} f_n^*(x_{(-)}) &= -2^{n/2} \sum_j \frac{1}{2} \left(\bar{f}_j^{nh} \phi_j(-1) + \bar{f}_j^{n,h-1} \phi_j(+1) \right) \\ &\quad + 2^{n/2} \sum_j \frac{\lambda_{\max}}{2} \left(\bar{u}_j^{nh} \phi_j(-1) + \bar{u}_j^{n,h-1} \phi_j(+1) \right) \end{aligned} \tag{194}$$

Substituting these into the boundary inner product and gathering like terms, the derivative is found compactly written as

$$\bar{q}^n = T \bar{f}^n + R \bar{u}^n \tag{195}$$

where the central difference operator T and the upwind correction operator R are (in the 1D case considered here) block tridiagonal matrices such that

$$\begin{aligned}\bar{q}^{nh} &= 2^n \left(T_{(1)} \bar{f}^{n,h-1} + T_{(2)} \bar{f}^{nh} + T_{(3)} \bar{f}^{n,h+1} \right) \\ &+ 2^n \left(R_{(1)} \bar{u}^{n,h-1} + R_{(2)} \bar{u}^{nh} + R_{(3)} \bar{u}^{n,h+1} \right)\end{aligned} \tag{196}$$

The sub-, main-, and super-diagonal blocks are defined as

$$\begin{aligned}T_{(1)_{ij}} &= -\frac{1}{2} \phi_i(-1) \phi_j(+1) \\ T_{(2)_{ij}} &= D_{x_{ij}} + \frac{1}{2} \left(-\phi_i(+1) \phi_j(+1) + \phi_i(-1) \phi_j(-1) \right) \\ T_{(3)_{ij}} &= \frac{1}{2} \phi_i(+1) \phi_j(-1)\end{aligned} \tag{197}$$

and

$$\begin{aligned}R_{(1)_{ij}} &= -\frac{\lambda_{\max}}{2} \phi_i(-1) \phi_j(+1) \\ R_{(2)_{ij}} &= \frac{\lambda_{\max}}{2} \left(\phi_i(+1) \phi_j(+1) + \phi_i(-1) \phi_j(-1) \right) \\ R_{(3)_{ij}} &= -\frac{\lambda_{\max}}{2} \phi_i(+1) \phi_j(-1)\end{aligned} \tag{198}$$

Figure 27 shows examples of the reference scheme stencil and the corresponding derivative operator compressed in the standard form.

3.4 Numerical Examples

The effectiveness of the multi-resolution discontinuous Galerkin (MRDG) method is now demonstrated by application to simple yet illustrative problems for the Euler equations in one dimension and two dimensions. The first several problems are repeated from Chapter 2 (some with minor alterations) to simply demonstrate feature tracking and compression of data. The vortex convection problem provides an opportunity to quantify the cost of the MRDG method for a meaningful problem in meaningful spatial dimension. The last example brings together the characteristics of smooth and non-smooth flow into a single problem and tests the method's ability to capture the interaction of a shock and vortex. All cases use the fourth-order Runge-Kutta scheme and a timestep restricted by a CFL factor of one-half: $\Delta t \leq \frac{1}{2} \mathrm{CFL}(p) \sqrt{|\Omega_{h(n)}|_{\min}} / \lambda_{\max}$. Details coefficients are truncated after each Runge-Kutta stage wherever density, momentum magnitude, and stagnation energy details all test below the threshold criteria.

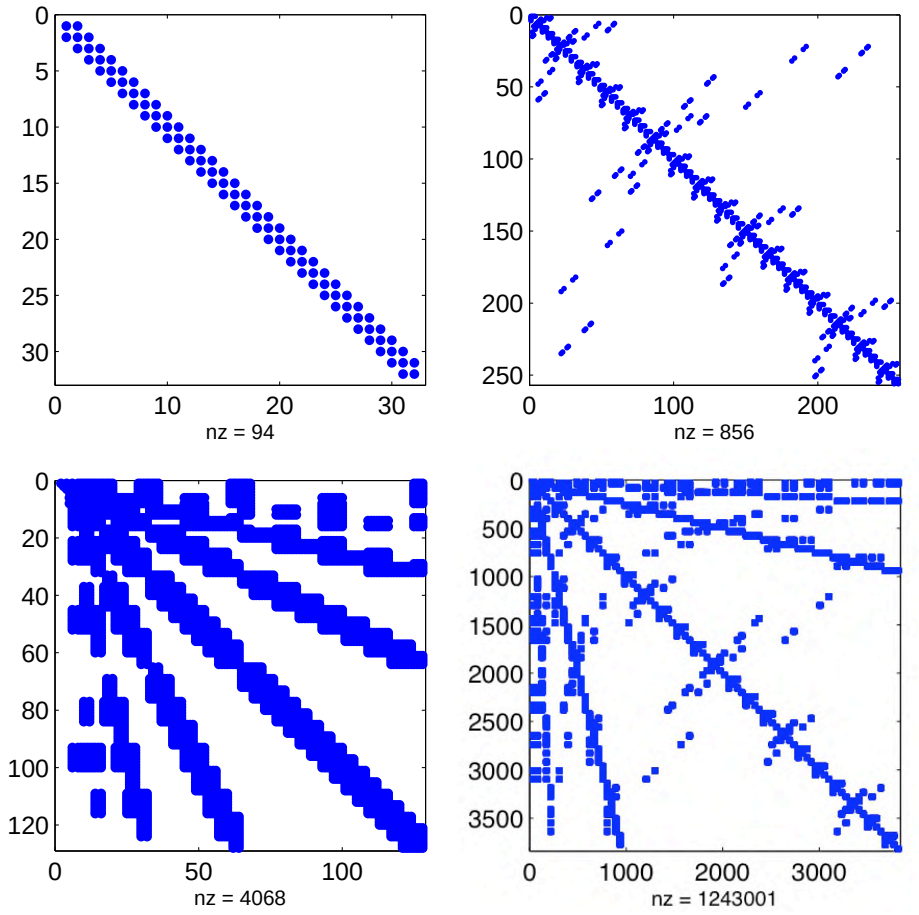

Figure 27: Examples of stencil and derivative operator D_x (standard form) in one and two-dimensions. The left column shows the one-dimensional stencil for $n = 5$ levels of detail and the corresponding derivative operator of degree $p = 3$. The right column shows the two-dimensional stencil for $n = 4$ levels of detail and the corresponding derivative operator of degree $p = 4$.

3.4.1 Acoustic Pulse

This problem is much like that computed for the basic DG method in Chapter 2. To elucidate the adaptation of the flowfield, the parameters modified as $A = 1.e-5$, $x_w = 0.05$ to generate a very thin pulse relative to the domain size. Time-dependent solutions are obtained at a timestep of $\Delta t = 2.e-4$ on a single element of degree $p = 9$ and $n = 5$ levels of detail . Figure 28 show time evolution of acoustic pulse, with markers indicating the *active* sub-regions of the multi-resolution decomposition. The solution data adapts to and tracks with the pulse as indicated by the non-uniform distribution of boundary markers. Figure 29 show the compression of active degrees of freedom relative to a uniform mesh of

2^n elements, *i.e.* $(N_{\text{uniform}} - N_{\text{multi-res}})/N_{\text{uniform}}$. A significant reduction the total degrees of freedom is achieved with a compression rate near 0.75.

3.4.2 Shock Tube

The sod shock tube problem is repeated using MRDG. Time-dependent solutions are obtained at a timestep of $\Delta t = 5.e-5$ on a single element of degree $p = 9$ and $n = 5$ levels of detail. Figure 30 shows time evolution of the flow. Figure 31 show the compression of active degrees-of-freedom. Similar to the previous example, this calculation achieves a DoF compression rate near 0.70.

3.4.3 Vortex Convection

To demonstrate the cost effectiveness in addition to the tracking / adaptation capability of the MRDG method, the isentropic vortex case of Chapter 2 is repeated here on a larger domain. This trivial alteration does not change the nature of the problem and provides a good vehicle for cost comparisons by considering combinations of degree and levels of detail.

Figure 32 shows the time evolution starting from the initial position in the center of a $x, y \in [-40, 40] \times [-10, 10]$ domain (approximately 20×5 core diameters). This particular solution uses a timestep $\Delta t = 1.e-2$ with $N = 32$ elements of degree $p = 3$ and $n = 4$ levels of detail and is typical of results for other p, n combination. Note that the number and level of active sub-regions is essentially constant, as should be expected. Figure 33 confirms an essentially constant DoF compression rate of approximately 0.959. Note that this is a large gain in compression rate compared to the one-dimensional acoustic pulse; thus the expectation for analogous three-dimensional problems is a rate near 0.99.

The efficiency of the method for various p, n is demonstrated in Figure 34 where the wallclock for $p = 1$, $n = 0$ is taken as the baseline. The initial rate of reduction in wallclock is roughly the same for different expansion degrees, while the continued payoff for increasing levels of detail favors decreasing expansion degree. This due to the correspondingly smaller overhead of the operators and the encoding / decoding algorithms. This overhead is a good example of where clever application of the non-standard form and the Beylkin procedure

for operators may hold greater potential over application of the standard form. Nevertheless, significant gains of greater than an order of magnitude in solution time are achieved with more "modest" values of p, which correspond to high orders of accuracy relative to traditional methods.

3.4.4 Shock-Vortex Interaction

The interaction between shock waves and vortices is of interest in the field of aeroacoustics and is often considered a knowledge building block for sound generation in supersonic turbulent flows. The following test case follows that of Inoue and Hattori [45], in which a vortex of prescribed strength is convected into a standing shock wave. The problem domain is $x, y \in [-24, 12] \times [-12, 12]$, with flow from right to left across a shock placed at $x = 0$. The vortex is initially placed in the supersonic stream upstream of the shock at $(x, y) = (8, 0)$. For this particular example, the parameters of the flow are taken from Inoue's Case D and are prescribed by the shock and vortex Mach numbers $M_s = 1.05$, $M_v = 0.5$. Note that the vortex Mach number is simply $M_s = B/2\pi$, with vortex strength B and gradient $A = 1/2$ used in previous examples. By selecting the upstream primitive variable state as $\rho = 1$, $u = -1.05$, $v = 0$, $p = 1/\gamma$, the state downstream of the shock is found from the normal shock relations [67]. Boundary conditions for the problem are periodic at $y = \pm 12$, fixed at $x = 12$, and extrapolation at $x = -24$. The timestep is $\Delta t = 1.e - 2$.

Figures 35-36 show the time evolution of density from shock impact to the final time using $N = 12$ elements of degree $p = 4$ and $n = 4$ levels of detail. The developing structure of the regular Mach reflection is visible as is the adaptation of the scheme to the salient features. It is interesting to note that the MRDG scheme correctly tracks the weak acoustic disturbance originating from the $t = 0^+$ over-shoot at the shock before the artificial viscosity has fully developed to damp the initial jump. The density field in Figure 37 compares favorably with a shadowgraph from Inoue and Hattori's calculation. Over the time history, more of the global domain is occupied by non-benign flow features as the diameter of the interaction grows. Figure 38 shows a DoF compression rate that is decreasing in time as expected, falling to a level of approximately 0.6.

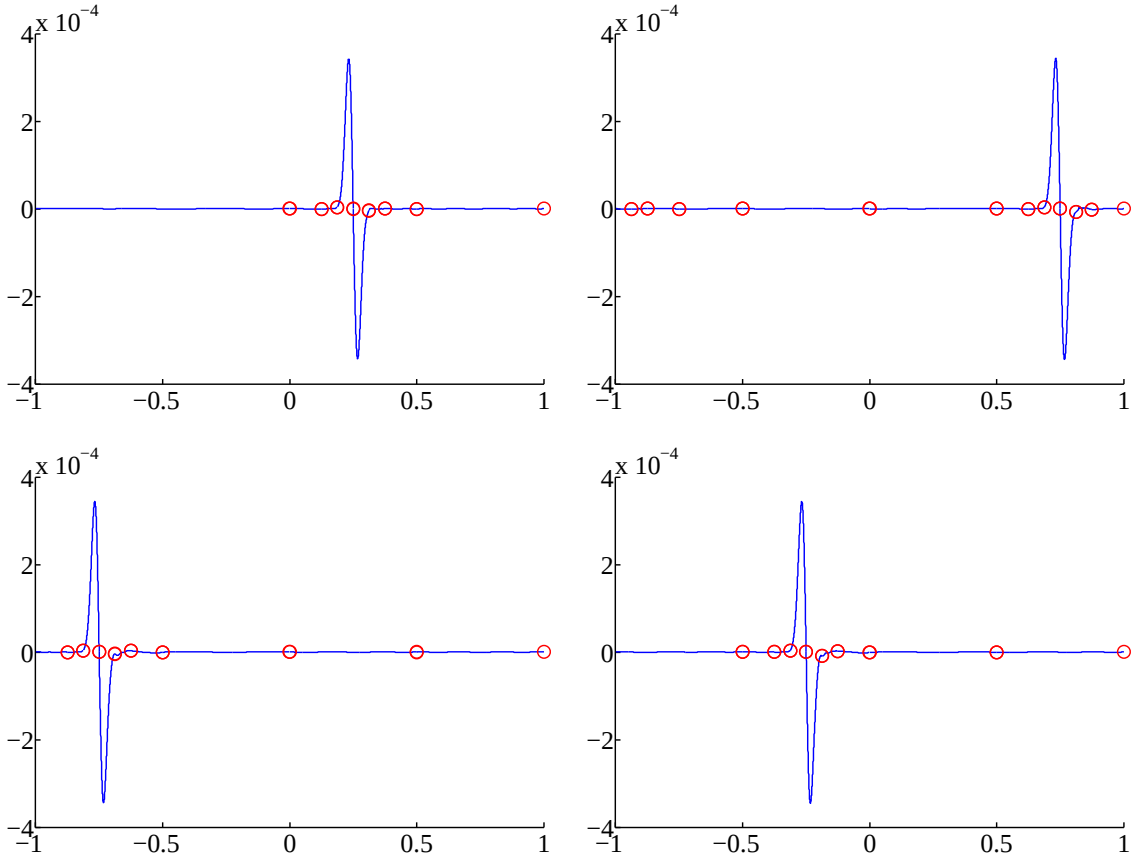

Figure 28: Time evolution of an acoustic pulse (x-momentum) with degree $p = 9$ and $n = 5$ levels of detail on a single element. Markers indicate sub-region boundaries.

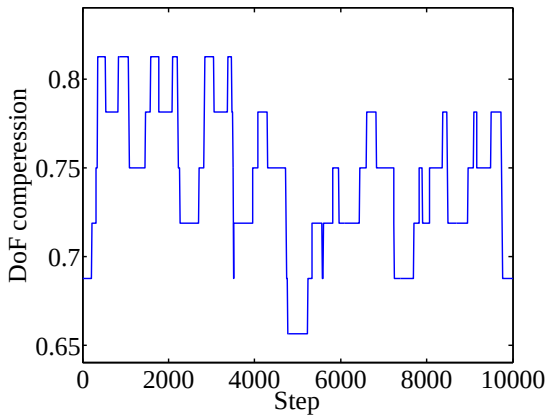

Figure 29: Compression history of active degrees of freedom for the acoustic pulse with degree $p = 9$ and $n = 5$ levels of detail on a single element. A compression rate of approximately 0.75 is achieved with the MRDG method.

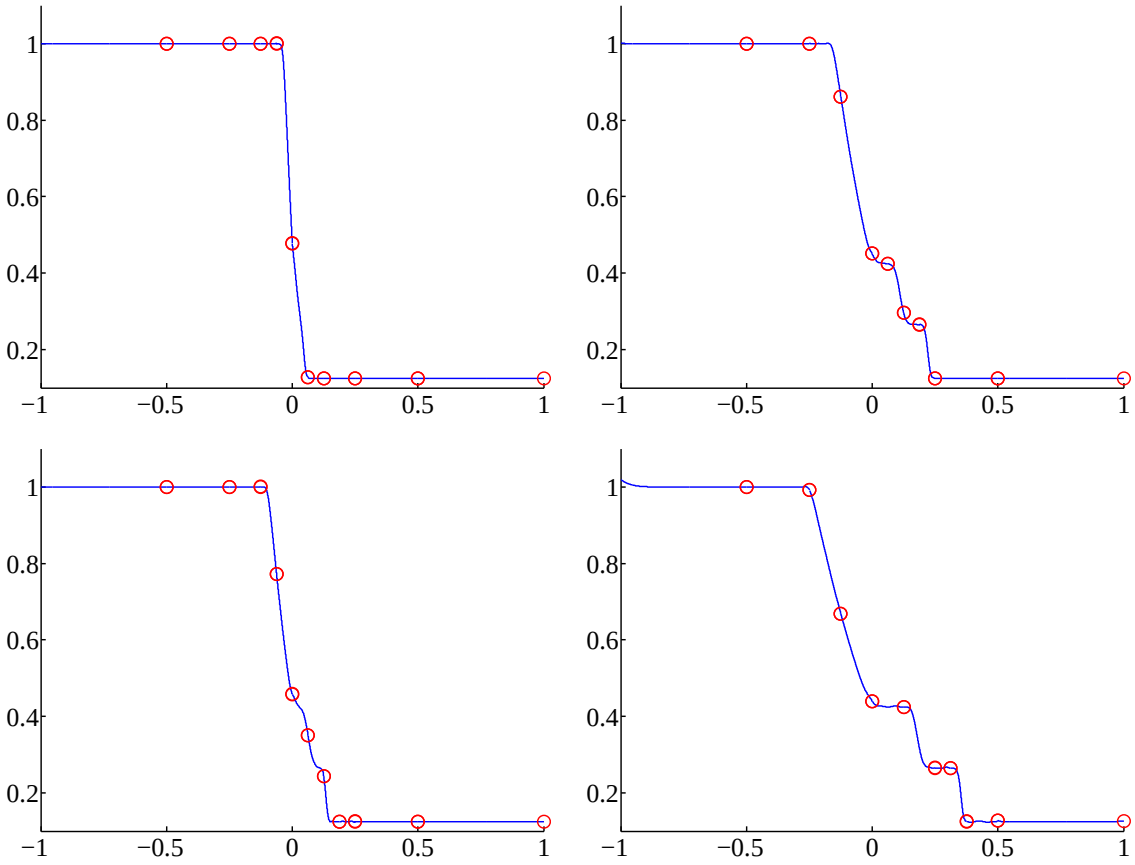

Figure 30: Time evolution of the Sod shock tube (density) with degree $p = 9$ and $n = 5$ levels of detail on a single element. Markers indicate sub-region boundaries.

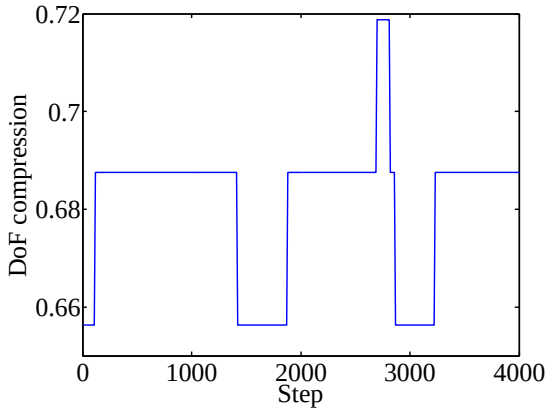

Figure 31: Compression history of active degrees of freedom for the Sod shock tube with degree $p = 9$ and $n = 5$ levels of detail on a single element. A compression rate of approximately 0.70 is achieved with the MRDG method.

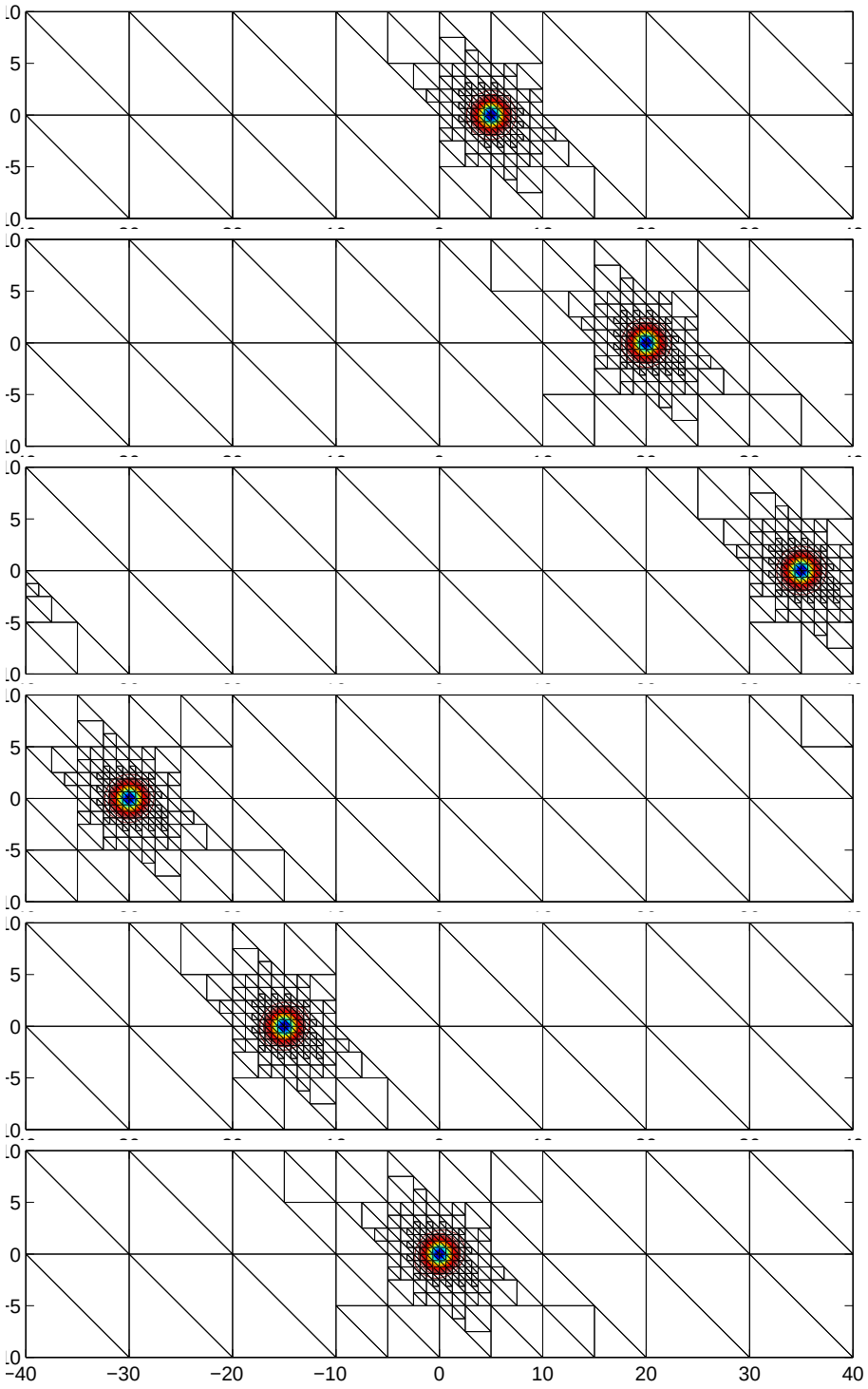

Figure 32: Time evolution and adaptation of vortex convection in a long distance periodic domain with the current MRDG scheme using $N = 32$ elements of degree $p = 3$ and $n = 4$ levels of detail. The first frame is after approximately 1 core diameter of convection; each subsequent frame is at an additional 3 core diameters.

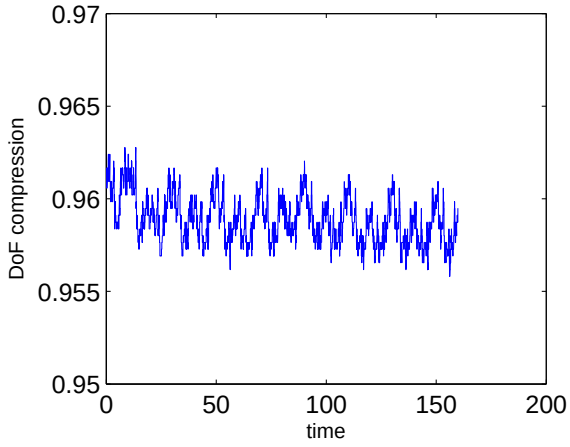

Figure 33: Compression time history of active degrees of freedom for the vortex using $N = 32$ elements of degree $p = 3$ and $n = 4$ levels of detail. The compression rate is approximately 0.959. Given this significant increase over the analogous one-dimensional pulse problem, rates near 0.99 may be expected in three-dimensions.

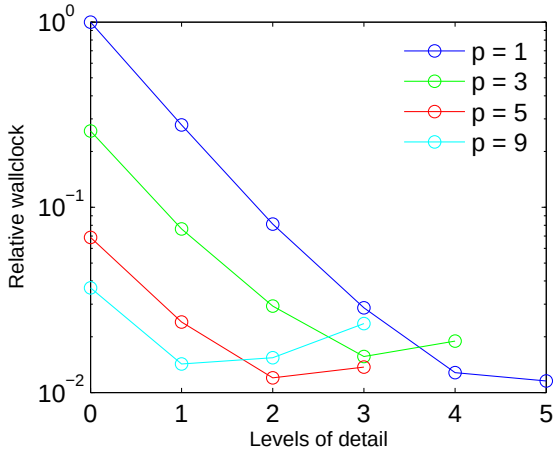

Figure 34: Efficiency of MRDG as a function of polynomial degree and levels of detail for the long-distance vortex convection problem. The initial rate of reduction in wallclock is roughly the same for different expansion degrees, while the return for increasing levels of detail favors decreasing expansion degree. This due to the correspondingly smaller overhead of the operators and the encoding / decoding algorithms. Use of the non-standard form of operators may provide greater effficiency.

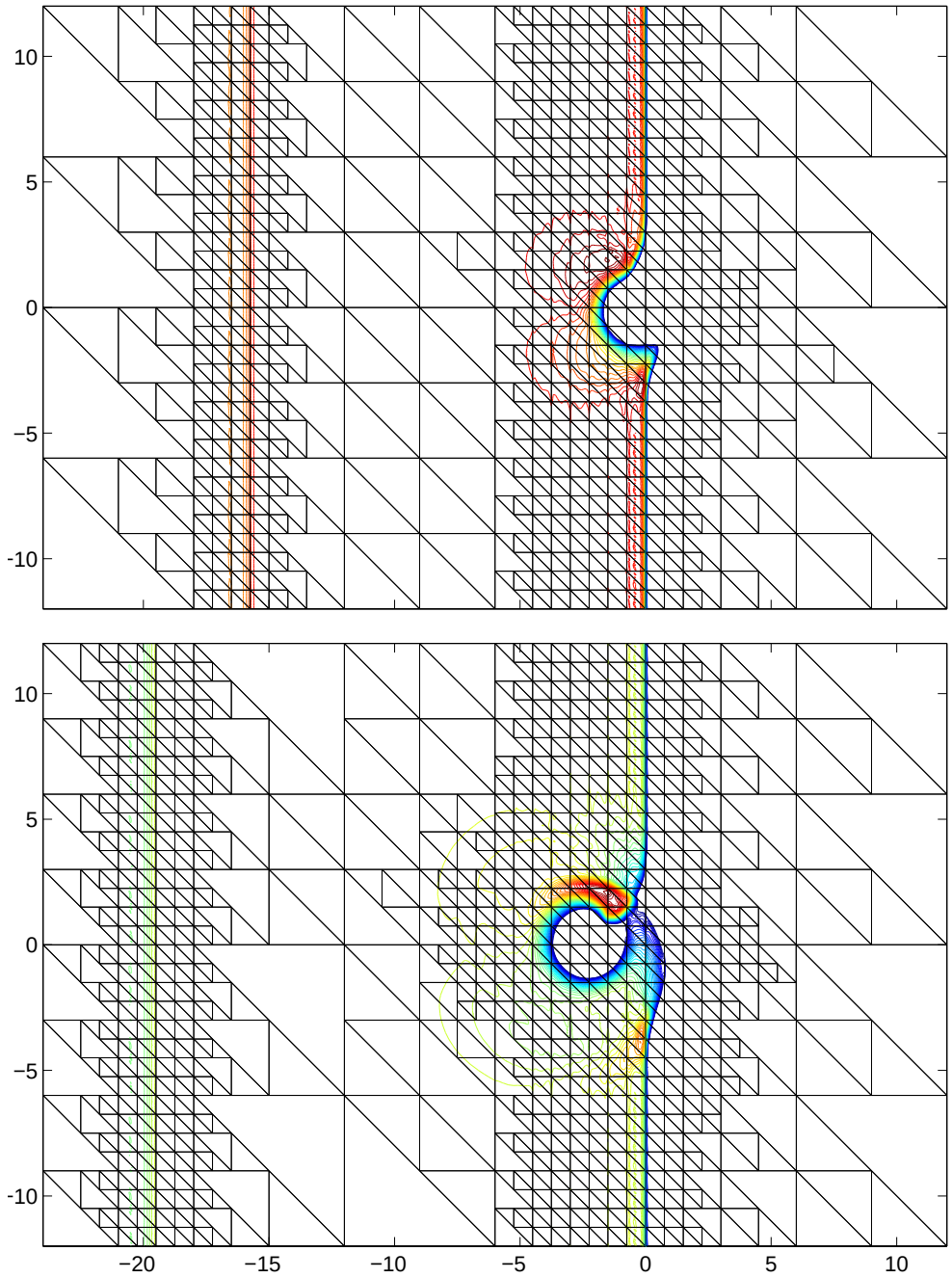

Figure 35: Time evolution and adaptation of a shock-vortex interaction with the current MRDG scheme using $N = 12$ elements of degree $p = 4$ and $n = 4$ levels of detail. Density contours are in the range $1.04 \leq \rho \leq 1.18$. Times are $t = 8, 10$. Note that the scheme also tracks the propagation of a wave originating from the initial $t = 0^+$ over-shoot in the solution at the shock.

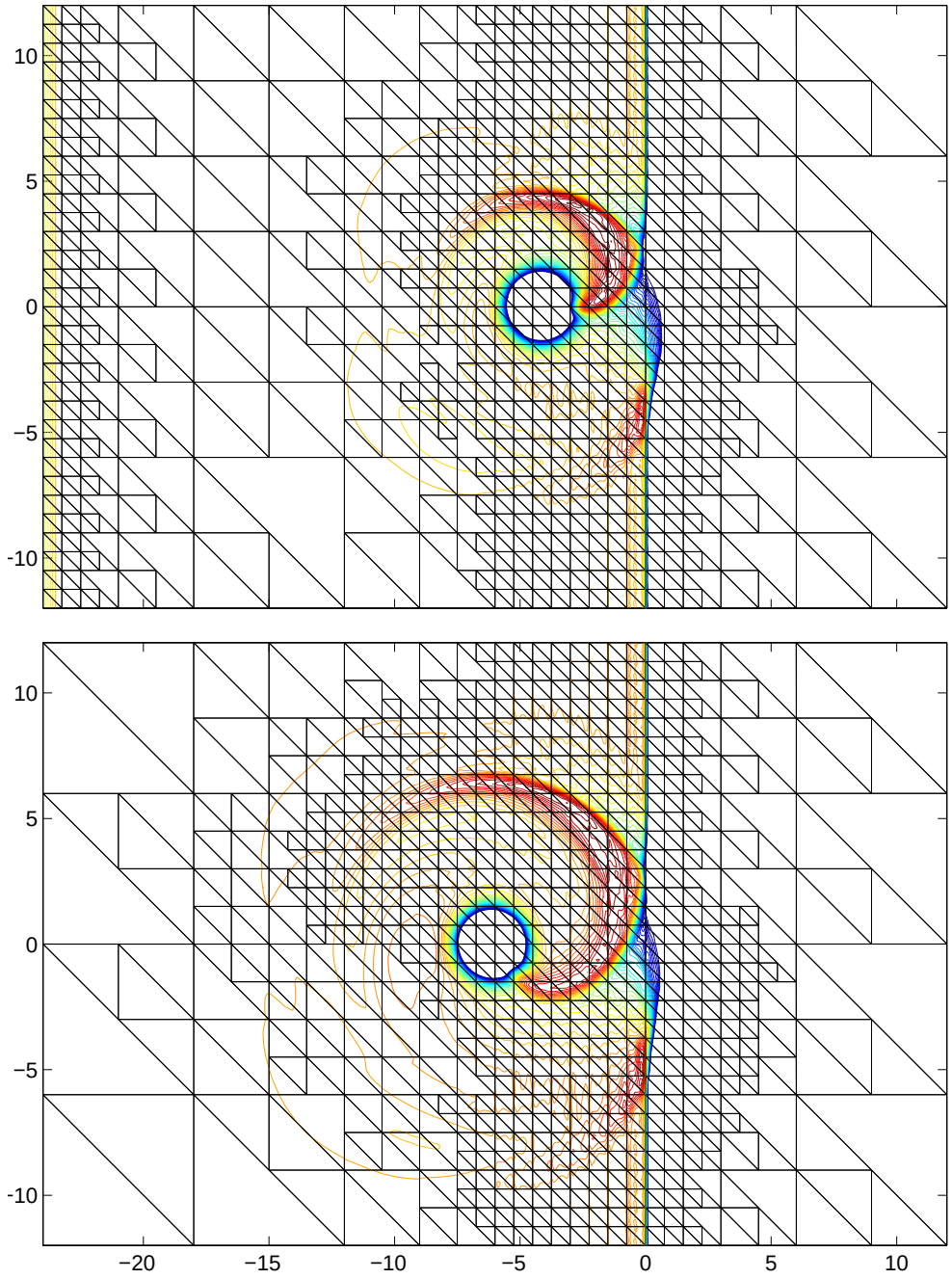

Figure 36: Continued time evolution and adaptation of a shock-vortex interaction. Times are $t = 12, 14$. By the final time, the original shock over-shoot wave has left the domain and the structure of the interaction is clear. Note that the shock Mach number of $M_s = 1.05$ results in a regular reflection.

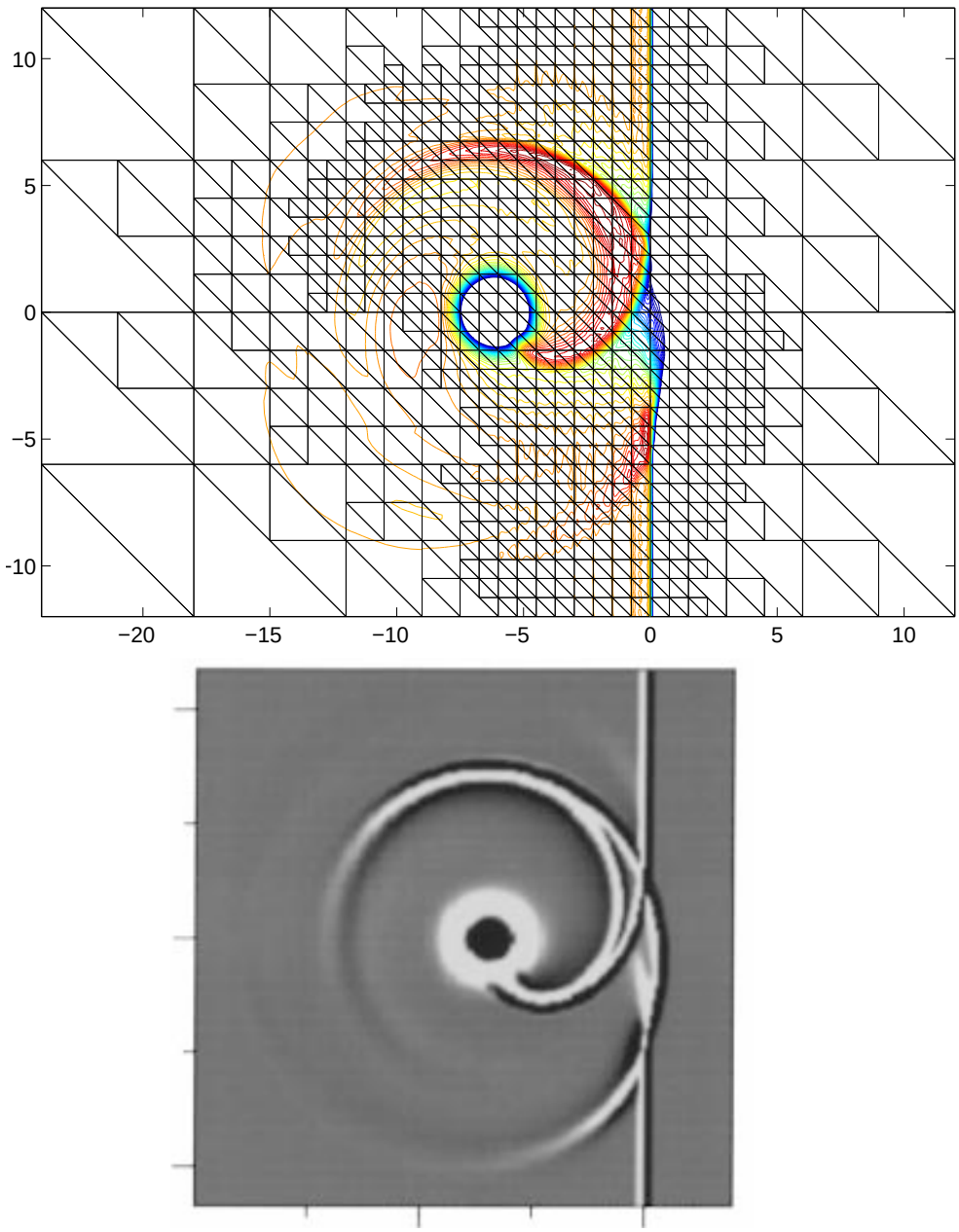

Figure 37: Comparison of shock-vortex interaction at the final time $t = 14$ with a shadowgraph from Inoue and Hattori case D [45]. The basic structure of the interaction is nicely resolved with the current MRDG scheme using $N = 12$ elements of degree $p = 4$ and $n = 4$ levels of detail. The reference computation uses a sixth-order compact Pade-type scheme on a stretched cartesian mesh of 1044×1170.

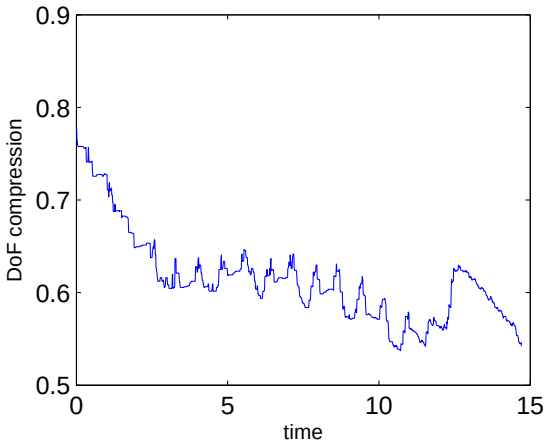

Figure 38: Compression time history of active degrees of freedom for the shock-vortex using $N = 12$ elements of degree $p = 4$ and $n = 4$ levels of detail. The decreasing rate is consistent for problems in which there is an increasing spatial extent of important flow features over time.

CHAPTER IV

ACCOMPLISHMENTS AND FUTURE DEVELOPEMENT

4.1 Conclusions

This thesis develops a general framework for unsteady compressible flows that simultaneously accommodates solution locality in both formal order of accuracy and physical scale. The following conclusions are drawn from the examples and derivations in this work.

- Solution error and problem run-time are observed to exponentially decay with increasing method order of accuracy-accuracy. The discontinuous Galerkin method provides a high order computational tool with local conservation, invariant stencil, and geometric flexibility.

- Problem run-time is observed to exponentially decay with increasing level of local spatial adaptation. The multi-resolution representation of data and operators provides an adaptation and compression framework which is *entirely solution-driven* without *ad hoc* error estimation and potentially non-robust and time-lagged mesh refinement.

- The multi-resolution framework and the discontinuous Galerkin method are well-suited for a new approach to accuracy and cost as demonstrated by the relative ease of their integration in spatial dimension greater than one. Some specific steps include the implementation of suitable data encoding and compression algorithms, construction of multi-wavelet expansion bases in one and two dimensions, and derivation of the multi-resolution derivative operator that includes an upwind-type correction to the central scheme.

- Solutions with the MRDG method are observed to adapt to and track with flow features of both smooth and shock character using no problem-class specific settings.

- The MRDG method provides order of magnitude run-time efficiency through local, high order adaptation. Additionally, solution data compression rates with MRDG

for one- and two-dimensional problems are observed to be 0.75 and 0.96, respectfully, when the salient flow features are have a spatially small extent compared to the global domain but are free to move anywhere within the domain. This trend suggests continued gain for analogous three-dimensional problems, which makes MRDG an attractive methodology to pursue for external 3D aerodynamics.

4.2 Recommendations

The long-term goal of this research is to provide – for the first time – high order, solution adaptation capability to hybrid Reynolds-averaged Navier-Stokes / Large Eddy Simulation. Recall that for LES-based approaches to turbulence closure, the effective filter width (*e.g.*, the local mesh size) plays an explicit role in the governing equations for turbulent kinetic energy. In existing adaptation strategies, the filter width and hence the problem itself is redefined as the mesh changes. The situation for the MRDG method is different since it is based on a pre-selected reference scheme having a corresponding effective filter width. In the MR framework, discarding small details within a defined tolerance does not redefine filter width, and therefore does not redefine the problem. This is possible since the method considers inter-region communication to be a multi-scale event such that output data from a given operation may immediately contain smaller or larger scales than the input data.

The following recommendations provide avenues of continued research to bring the MRDG method into the mainstream as the approach of choice for demanding compressible flow simulations.

- An extension to three-dimensions is straightforward. Koornwinder-Dubiner-like basis functions and the Warburton procedure for Fekete nodes already exist for the canonical tetrahedron. The Alpert procedure for multi-wavelet functions is readily extended beyond the canonical triangle using the numerical approach for the direct formation of the high-pass filter matrix.

- The problem domain can easily contain elements of different expansion degree and levels of detail, and this may be exploited in both static and dynamic fashions. For

example, in external flow situations where greater resolution is expected in the near-field, elements in that region are specified to a have high order and/or a high level of detail as part of problem setup. In addition to mesh clustering, this provides two additional opportunities for a pre-emptive increase in resolution. Furthermore, when a region has saturated details (losing data sparsity) for long periods of solution time, local order-of-accuracy and/or levels of detail may be increased beyond the initial settings by a simple padding of the solution data and a (possibly pre-computed and stored) redefinition of the necessary operators. Similarly, when regions have very sparse solution representations, order-of-accuracy and/or levels of detail may be reduced to deallocate memory from the unused portions of operators.

- The detail thresholding / truncation process itself can be made adaptive beyond the dependence upon spatial variation in expansion degree and detail level. A variety of strategies are possible and include a distance- or position-based threshold increase or regionally-defined threshold target quantities (*e.g.*, density, kinetic energy, *etc*).

- Implement a PDE-based artificial viscosity model, such that damping reacts to and impacts the solution in a coupled fashion. This approach provides an additional quantity upon which to base the detail thresholding and more importantly provides a direct relationship between solution damping and data truncation.

- The non-standard form is known to be more sparse than the standard form and the intermediate state of the output data in the Beylkin algorithm provides a potentially valuable opportunity for thresholding small values. Address the challenges in averages promotion logic in many-to-one h region reference scheme operations that require communication with neighboring sub-regions at a given level.

- Investigate the use of interpolating basis functions to provide additional economy in the computation of nonlinear quantities. The current de-aliasing procedure using over-integration and Galerkin projection may be augmented with an analogous "over-refinement" and multi-wavelet projection to enhance the quality of nonlinear combinations of a marginally-resolved solution state.

REFERENCES

[1] Abgrall, R. and Harten, A., "Multiresolution representation in unstructured meshes," *SIAM Journal on Numerical Analysis*, vol. 35, no. 6, pp. 2128–2146, 1998.

[2] Alpert, B., Belykin, G., Gines, D., and Vozovoi, L., "Adaptive solution of partial differential equations in multiwavelet bases," *Journal of Computational Physics*, vol. 182, no. 1, pp. 149–190, 2002.

[3] Alpert, B. K., "Wavelets and other bases for fast numerical linear algebra," in *Wavelets: A Tutorial* (Chui, C. K., ed.), Academic Press, 1992.

[4] Alpert, B. K., "A class of bases in L^2 for the sparse representation of integral operators," *SIAM Journal on Mathematical Analysis*, vol. 24, no. 1, pp. 246–262, 1993.

[5] Anderson, J., *Modern Compressible Flow with Historical Perspective*. McGraw-Hill, third ed., 2003.

[6] Arnold, D., Brezzi, F., Cockburn, B., and Marini, L. D., "Unified analysis of discontinuous Galerkin methods for elliptic problems," *SIAM Journal on Numerical Analysis*, vol. 39, no. 5, pp. 1749–1779, 2002.

[7] Ascher, U. and Petzold, L., *Computer Methods for Ordinary Differential Equations and Differential-Algebraic Equations*. SIAM, 1998.

[8] Barter, G. and Darmofal, D., "Shock capturing with higher-order, pde-based artificial viscosity," in *18th AIAA Computational Fluid Dynamics Conference*, (Miami, FL), American Institute of Aeronautics and Astronautics, June 2007.

[9] Bassi, F., Crivellini, A., Rebay, S., and Savini, M., "Discontinuous Galerkin solution of the Reynolds-averaged Navier-Stokes and $k-\omega$ turbulence model equations," *Computers and Fluids*, vol. 34, no. 4-5, pp. 507–540, 2005.

[10] Bassi, F. and Rebay, S., "A high-order accurate discontinuous finite element method for the numerical solution of the compressible Navier-Stokes equations," *Journal of Computational Physics*, vol. 131, no. 2, pp. 253–379, 1997.

[11] Bassi, F. and Rebay, S., "High-order accurate discontinuous finite element solution of the 2d Euler equations," *Journal of Computational Physics*, vol. 138, pp. 251–285, 1997.

[12] Bassi, F. and Rebay, S., "Numerical evaluation of two discontinuous Galerkin methods for the compressible navier-stokes equations," *International Journal for Numerical Methods in Fluids*, vol. 40, no. 1-2, pp. 197–207, 2002.

[13] Baumann, C., *An hp-Adaptive Discontinuous Galerkin Finite Element Method for Computational Fluid Dynamics*. PhD thesis, The University of Texas at Austin, 1997.

[14] Baumann, C. and Oden, J. T., "A discontinuous *hp* finite element method for the euler and navier-stokes equations," *International Journal for Numerical Methods in Fluids*, vol. 31, no. 1, pp. 79–95, 1999.

[15] Beylkin, G., "On the representation of operators in bases of compactly supported wavelets," *SIAM Journal on Numerical Analysis*, vol. 29, no. 6, pp. 1716–1740, 1992.

[16] Beylkin, G., Cheruvu, V., and Pérez, F., "Fast adaptive algorithms in the non-standard form for multidimensional problems," *Applied and Computational Harmonic Analysis*, vol. in press, 2007.

[17] Beylkin, G., Coifman, R., and Rokhlin, V., "Fast wavelet transforms and numerical algorithms I," *Communications on Pure and Applied Mathematics*, vol. 44, no. 2, pp. 141–183, 1991.

[18] Beylkin, G. and Keiser, J., "On the adaptive numerical solution of nonlinear partial differential equations in wavelet bases," *Journal of Computational Physics*, vol. 132, no. 2, pp. 233–259, 1997.

[19] Bihari, B. and Harten, A., "Multiresolution schemes for the numerical solution of 2-d conservation laws I," *SIAM Journal on Scientific Computing*, vol. 18, no. 2, pp. 315–354, 1997.

[20] Bos, L., "On certain configuration of points in $\mathbb{R}^n$ which are unisolvent for polynomial interpolation," *Journal of Approximation Theory*, vol. 64, no. 3, pp. 271–280, 1991.

[21] Chen, Q. and Babuška, I., "Approximate optimal points for polynomial interpolation of real functions in an interval and in a triangle," *Computer Methods in Applied Mechanics and Engineering*, vol. 128, no. 3-4, pp. 405–417, 1995.

[22] Cockburn, B. and Shu, C. W., "The local discontinuous Galerkin method for time-dependent convection-diffusion systems," *SIAM Journal on Numerical Analysis*, vol. 35, no. 6, pp. 2440–2463, 1998.

[23] Cockburn, B. and Shu, C. W., "The Runge-Kutta discontinuous Galerkin method for convection-dominated problems," *Journal of Scientific Computing*, vol. 16, no. 3, pp. 173–261, 2001.

[24] Daubechies, I., *Ten Lectures on Wavelets*. SIAM, 1992.

[25] Daubechies, I., "Where do wavelets come from? – a personal point of view," *Proceedings of the IEEE*, vol. 84, no. 4, pp. 510–513, 1996.

[26] Diosady, L. and Darmofal, D., "Discontinuous Galerkin solutions of the Navier-Stokes equations using linear multigrid preconditioning," in *18th Computational Fluid Dynamics Conference*, (Miami, FL), American Institute of Aeronautics and Astronautics, June 2007.

[27] Dubiner, M., "Spectral methods on triangle and other domains," *Journal of Scientific Computing*, vol. 6, no. 4, pp. 345–390, 1991.

[28] Ekaterinaris, J., "High-order accurate, low numerical diffusion methods for aerodynamics," *Progress in Aerospace Sciences*, vol. 41, no. 3-4, pp. 192–300, 2005.

[29] Farge, M. and Schneider, K., "Coherent vortex simulation (CVS), a semi-deterministic turbulence model using wavelets," *Flow, Turbulence and Combustion*, vol. 66, no. 4, pp. 393–426, 2001.

[30] Farge, M., Schneider, K., and Kevlahan, N., "Non-gaussianity and coherent vortex simulation for two-dimensional turbulence using an adaptive orthogonal wavelet basis," *Physics of Fluids*, vol. 11, no. 8, pp. 2187–2201, 1999.

[31] Frölich, J. and Schneider, K., "An adaptive wavelet-vaguelette algorithm for the solution of PDEs," *Journal of Computational Physics*, vol. 130, no. 2, pp. 174–190, 1997.

[32] Garnier, E., Sagaut, P., and Deville, M., "A class of explicit ENO filters with application to unsteady flows," *Journal of Computational Physics*, vol. 170, no. 1, pp. 184–204, 2001.

[33] Goldstein, D. and Vasilyev, O., "Stochastic coherent adaptive large eddy simulation method," *Physics of Fluids*, vol. 16, no. 7, pp. 2497–2513, 2004.

[34] Gordon, W. and Hall, C., "Construction of curvilinear coordinate systems and application to mesh generation," *International Journal for Numerical Methods in Engineering*, vol. 7, no. ?, pp. 461–477, 1973.

[35] Grinberg, L. and Karniadakis, G. E., "Hierarchical spectral basis and Galerkin formulation using barycentric quadrature grids in triangular elements," *Journal of Engineering Mathematics*, vol. 56, no. 3, pp. 289–306, 2006.

[36] Harten, A., "Discrete multi-resolution analysis and generalized wavelets," Tech. Rep. CAM 92-08, UCLA Group in Computational and Applied Mathematics, 1992.

[37] Harten, A., "Multiresolution representation of data I: Preliminary report," Tech. Rep. CAM 93-13, UCLA Group in Computational and Applied Mathematics, 1993.

[38] Harten, A., "Multiresolution representation of cell-averaged data," Tech. Rep. CAM 94-21, UCLA Group in Computational and Applied Mathematics, 1994.

[39] Harten, A., "Multiresolution representation of data: A general framework," *SIAM Journal on Numerical Analysis*, vol. 33, no. 3, pp. 1205–1256, 1996.

[40] Harten, A. and Yad-Shalom, I., "Fast multiresolution algorithms for matrix-vector multiplications," *SIAM Journal on Numerical Analysis*, vol. 31, no. 4, pp. 1191–1218, 1994.

[41] Heil, C. and Walnut, D., *Fundametal Papers in Wavelet Theory*. Princeton University Press, 2006.

[42] Hesthaven, J., "From electrostatics to almost optimal nodal sets for polynomial interpolation in a simplex," *SIAM Journal on Numerical Analysis*, vol. 35, no. 2, pp. 655–676, 1998.

[43] Hesthaven, J. and Warburton, T., "Nodal high-order methods on unstructured grids I. time-domain solution of Maxwell's equations," *Journal of Computational Physics*, vol. 181, no. 1, pp. 186–221, 2002.

[44] Holmström, M., "Solving hyperbolic PDEs using interpolating wavelets," *SIAM Journal on Scientific Computing*, vol. 21, no. 2, pp. 405–420, 1999.

[45] Inoue, O. and Hattori, Y., "Sound generation by shock-vortex interactions," *Journal of Fluid Mechanics*, vol. 380, no. 3, pp. 81–116, 1999.

[46] Jameson, L., "A wavelet-optimized, very high order adaptive grid and order numerical method," *SIAM Journal on Scientific Computing*, vol. 19, no. 6, pp. 1980–2013, 1998.

[47] Karniadakis, G. E. and Sherwin, S., *Spectral/hp Element Methods for Computational Fluid Dynamics*. Oxford University Press, second ed., 2005.

[48] Karniadakis, I. L. G. E., "A discontinuous Galerkin method for the Navier-Stokes equations," *International Journal for Numerical Methods in Fluids*, vol. 29, no. ?, pp. 587–603, 1999.

[49] Kirby, R. and Karniadakis, G. E., "De-aliasing on non-uniform grids: Algorithms and applications," *Journal of Computational Physics*, vol. 191, no. 1, pp. 249–264, 2003.

[50] Koornwinder, T., "Two-variable analogues of the classical orthogonal polynomials," in *Theory and Applications of Special Functions* (Askey, R., ed.), Academic Press, 1975.

[51] Kuethe, A. and Chow, C. Y., *Foundations of Aerodynamics*. John Wiley and Sons, fourth ed., 1986.

[52] Laney, C., *Computational Gasdynamics*. Cambridge Univerity Press, 1998.

[53] Lomtev, I., *A Discontinuous Galerkin Method for the Compressible Navier-Stokes Equations in Stationary and Moving 3D Domains*. PhD thesis, Brown University, 1999.

[54] Lomtev, I., Kirby, R., and Karniadakis, G. E., "A discontinuous Galerkin ALE method for compressible viscous flows in moving domains," *Journal of Computational Physics*, vol. 155, no. 1, pp. 128–159, 1999.

[55] Lomtev, I., Quillen, C., and Karniadakis, G. E., "Spectral/hp methods for viscous compressible flows on unstructured 2d meshes," *Journal of Computational Physics*, vol. 144, no. 2, pp. 325–357, 1998.

[56] Luo, X. J., Shephard, M., O'Bara, R., Nastasia, R., and Beall, M., "Automatic p-version mesh generation for curved domains," *Engineering with Computers*, vol. 20, no. 3, pp. 273–285, 2004.

[57] Mallat, S., "Theory for multiresolution signal decomposition: The wavelet representation," *IEEE Transactions on Pattern Analysis and Machine Intelligence*, vol. 11, no. 7, pp. 674–693, 1989.

[58] Mallat, S., *A Wavelet Tour of Signal Processing*. Academic Press, 1999.

[59] Mani, K. and Mavriplis, D., "A parallel hp-multigrid solver for three-dimensional discontinuous Galerkin discretizations of the Euler equations," in *45th Aerospace Sciences Meeting and Exhibit*, (Reno, NV), American Institute of Aeronautics and Astronautics, January 2007.

[60] Meyer, Y., "Ondelettes et fonctions splines," in *Séminaire sur les équations aux dérivées partielles 1986–1987*, École Polytechnique, 1987.

[61] Natase, C. and Mavriplis, D., "Discontinuous Galerkin methods using an *hp*-multigrid solver for inviscid compressible flows on three-dimensional unstructured meshes," in *44th Aerospace Sciences Meeting and Exhibit*, (Reno, NV), American Institute of Aeronautics and Astronautics, January 2006.

[62] Oliver, T. and Darmofal, D., "An unsteady adaptation algorithm for discontinuous galerkin discretizations of the rans equations," in *18th AIAA Computational Fluid Dynamics Conference*, (Miami, FL), American Institute of Aeronautics and Astronautics, June 2007.

[63] Persson, P. O. and Peraire, J., "An efficient low memory implicit dg algorithm for time dependent problems," in *44th Aerospace Sciences Meeting and Exhibit*, (Reno, NV), American Institute of Aeronautics and Astronautics, January 2006.

[64] Persson, P. O. and Peraire, J., "Sub-cell shock capturing for discontinuous Galerkin methods," in *44th Aerospace Sciences Meeting and Exhibit*, (Reno, NV), American Institute of Aeronautics and Astronautics, January 2006.

[65] Piomelli, U., "Large eddy simulation: Achievements and challenges," *Progress in Aerospace Sciences*, vol. 35, no. 4, pp. 335–362, 1999.

[66] Remacle, J. F., Flaherty, J., and Shephard, M., "An adaptive discontinuous Galerkin technique with an orthogonal basis applied to compressible flow problems," *SIAM Review*, vol. 45, no. 1, pp. 53–72, 2003.

[67] Staff, A. R., "Equations, tables, and charts for compressible flow," Tech. Rep. NACA TR-1135, Ames Aeronautical Laboratory, National Advisory Committee for Aeronautics, 1953.

[68] Sweldens, W., "The lifting scheme: A construction of second generation wavelets," *SIAM Journal on Mathematical Analysis*, vol. 29, no. 2, pp. 511–546, 1998.

[69] Tannehill, J., Anderson, D., and Pletcher, R., *Computational Fluid Dynamics and Heat Transfer*. Taylor and Francis, second ed., 1997.

[70] Taylor, M., Wingate, B., and Vincent, R., "An algorithm for computing Fekete points in the triangle," *SIAM Journal on Numerical Analysis*, vol. 38, no. 5, pp. 1707–1720, 2000.

[71] Trefethen, L. and Bau, D., *Numerical Linear Algebra*. SIAM, 1997.

[72] Vasilyev, O. and Bowman, C., "Second-generation wavelet collocation method for the solution of partial differential equations," *Journal of Computational Physics*, vol. 165, no. 2, pp. 660–693, 2000.

[73] Vasilyev, O., Paolucci, S., and Sen, M., "A multilevel wavelet collocation method for solving partial differential equations in a finite domain," *Journal of Computational Physics*, vol. 120, no. 1, pp. 33–47, 1995.

[74] Wang, L. and Mavriplis, D., "Implicit solution of the unsteady Euler equations for high-order accurate discontinuous galerkin discretizations," in *44th Aerospace Sciences Meeting and Exhibit*, (Reno, NV), American Institute of Aeronautics and Astronautics, January 2006.

[75] Wang, Z. J., "High-order methods for the Euler and Navier-Stokes equations on unstructured grids," *Progress in Aerospace Sciences*, vol. 43, no. 1-3, pp. 1–41, 2007.

[76] Warburton, T., *Spectral/hp Methods on Polymorphic Multi-Domains: Algorithms and Aplications*. PhD thesis, Brown University, 1999.

[77] Warburton, T., "An explicit construction of interpolation nodes on the simplex," *Journal of Engineering Mathematics*, vol. 56, no. 3, pp. 247–262, 2006.

[78] Warburton, T., Pavarino, L., and Hesthaven, J., "A psuedo-spectral scheme for the incompressible Navier-Stokes equations using unstructured nodal elements," *Journal of Computational Physics*, vol. 164, no. 1, pp. 1–21, 2000.

[79] Whitham, G., *Linear and Non-linear Waves*. John Wiley and Sons, 1974.

[80] Wingate, B. and Taylor, M., "The Koorwinder polynomials are the eigenfunctions of a singular Sturm-Liouville problem in the simplex," Tech. Rep. LA-UR 98-1278, Los Alamos National Laboratory, 1998.

[81] Wingate, B. and Taylor, M., "The natural function space for triangular and tetrahedral spectral elements." Submitted to SIAM Journal on Numerical Analysis, 1998.

[82] Yee, H., Sandham, N., and Djomehri, M., "Low-dissapative high-order shock-capturing methods using characteristic-based filters," *Journal of Computational Physics*, vol. 150, no. 1, pp. 199–238, 1999.

[83] Yu, T., Kolarov, K., and Lynch, W., "Barysymmetric multiwavelets on triangle," Tech. Rep. IRC 1997-006, Interval Research Corporation, 1997.

VITA

Andrew Brian Shelton was born in Birmingham, Alabama on February 5, 1971 to Douglas Jay and Mary Dean (Whorton) Shelton. He is married to the former Anna Catherine Neville Hasher of Greenville, South Carolina and they have a daughter Ella.

Andrew graduated valedictorian from Thompson High School in Alabaster, Alabama in 1989 and began his career in engineering by earning a Bachelor of Aerospace Engineering at Auburn University in 1994. He continued his education at Auburn and in 1997 earned a Master of Science in Mechanical Engineering.

Andrew worked in the area of applied computational fluid dynamics from 1997-2003 at Raytheon, General Electric and Lockheed-Martin. In 2003 he returned to the classroom as a Doctoral student in Aerospace Engineering at the Georgia Institute of Technology. There he performed research in the area of unsteady, turbulent aerodynamics using numerical techniques, earning a Doctorate of Philosophy in 2008. That same year, Andrew accepted a faculty appointment in Aerospace Engineering at Auburn University.

Andrew is a member of the American Institute of Aeronautics and Astronautics, the American Helicopter Society, and the National Aerospace Engineering Honor Society, Sigma Gamma Tau.